

**DEVELOPMENT AND INVESTIGATION OF INTEGRATED SOLAR SYSTEMS
FOR HYDROGEN AND METHANOL PRODUCTION**

by

Janette Hogerwaard

A Thesis Submitted in Partial Fulfillment
of the Requirements for the Degree of Doctor of Philosophy

in

Mechanical Engineering

Faculty of Engineering and Applied Science
University of Ontario Institute of Technology

Oshawa, Ontario, Canada

April, 2018

ABSTRACT

Implications of climate change, in particular the negative effects of greenhouse gas (GHG) emissions resulting from fossil fuel combustion, as well as the finite nature of fossil fuels necessitate the implementation of reliable and environmentally benign alternative energy options. This is particularly true for transportation and power generation sectors, which are responsible for the majority of carbon dioxide emissions. Hydrogen is a clean fuel that can be produced from renewable energy via electrolysis and direct photonic energy conversion from sunlight, produces no harmful emissions in combustion, and can be converted to electricity via fuel cells with good efficiency. However, it is challenging to store H_2 in a cost and energy efficient manner, and it is not widely available to consumers in comparison to traditional liquid fuels for transportation applications. Storage of H_2 produced from solar energy in synthetic fuels is a key step in moving towards an eventual hydrogen economy. By conversion to synthetic fuels such as methanol, hydrogen and solar energy may be directly utilised in current infrastructures as liquid fuels for transportation or in power generation applications.

This thesis experimentally investigates clean hydrogen production from solar energy and water using a novel photoelectrochemical water-splitting reactor designed, built, and tested at the Clean Energy Research Laboratory in UOIT. Integrating solar concentration and a spectrum-splitting mirror allows simultaneous photovoltaic electricity generation and direct photonic energy conversion to split water via PEM electrolysis and photoelectrochemical water splitting on the custom built photocathode of the reactor. Case studies are presented for system integration with methanol synthesis from solar energy and anthropogenic carbon capture for environmentally benign fuel production.

Keywords: Hydrogen production, Solar energy, Photoelectrochemical process, Methanol, Efficiency

DEDICATION

I dedicate this work to my family. My mother, Tessa Hogerwaard, who is are the strongest and best person I know. My sister Erika, who is my much better half and always keeps me grounded. And to my father, Ernst Hogerwaard, who made me curious about how the world around me works and is why I chose engineering – I miss you always, and hope you're watching over us.

ACKNOWLEDGEMENTS

I would like to express my sincere thanks to my supervisor and mentor, Dr. Ibrahim Dincer, whom I have had the privilege of studying under for nearly seven years. As an undergraduate student I was inspired by my Professor's knowledge and enthusiasm for progressive research that helps make the world a better place. I am so grateful that he encouraged me to pursue graduate studies, and for his invaluable guidance, patience, and support along the way. I would also like to sincerely thank my co-supervisor, Dr. Greg F. Naterer for his support of my research, and for his guidance throughout my studies.

Many thanks to Dr. Calin Zamfirescu for his support throughout my graduate studies. Dr. Yusuf Bicer, I could not have asked for a better colleague for our experimental research. Farrukh Khalid, for his kind encouragement especially during the writing of this thesis. To my friends and colleagues at UOIT for their support and good humour, Maan Al-Zareer, Ahmed Hasan, Canan Acar, Rami El-Emam, and many others along the way.

To my dearest friends—Meagan, Nadia, Eva, and Natalie. I am so lucky to have such an impressive and strong group of women supporting me.

TABLE OF CONTENTS

Abstract	ii
Acknowledgements	iii
Table of Contents	v
List of Tables	ix
List of Figures	xi
Nomenclature	xvii
CHAPTER 1: Introduction	1
1.1 World Energy and Environmental Outlook	1
1.2 Solar Energy	2
1.3 Hydrogen	3
1.3.1 Renewable Hydrogen Production Methods	4
1.3.2 Hydrogen Storage	4
1.4 Solar Energy and H ₂ Storage in Synthetic Fuels	5
1.4.1 Potential Solar Fuel Options	6
1.4.2 Resource Sustainability Considerations for Solar Fuel Synthesis	8
1.5 Motivation	11
1.5.1 Novelty and Originality	12
1.6 Objectives	13
CHAPTER 2: Background and Literature Review	16
2.1 Introduction	16
2.2 Solar Energy Conversion	16
2.2.1 Solar Power Generation	16

2.2.2	Solar H ₂ Production from Water Splitting	20
2.2.3	Solar H ₂ and CO ₂ Fuel Production Processes	23
2.2.4	Solar Methanol Production	24
2.3	Photoelectrochemical Hydrogen Production.....	25
2.3.1	Photoactive Materials.....	26
2.4	Main Gaps in the Literature	27
CHAPTER 3: Experimental Apparatus and Procedures for CPV-PEC H ₂ Production.....		29
3.1	Experimental System Description.....	30
3.2	Experimental Equipment.....	31
3.2.1	PEC Reactor.....	31
3.2.2	Concentrating Lens and Dielectric Mirror	34
3.2.3	Photovoltaic (PV) Module	35
3.3	Experimental Devices and Procedures	37
3.3.1	Gamry Reference 3000 Potentiostat with 30 K booster.....	37
3.3.1	Solar Simulator	37
3.3.3	Experimental Procedures	38
3.4	Experimental Error and Measurement Uncertainties	40
CHAPTER 4: Integrated Systems for Solar Methanol Fuel Synthesis.....		42
4.1	Integrated System I: CPV-PEC Based Methanol Synthesis.....	42
4.1.1	Methanol Synthesis via CO ₂ Hydrogenation	43
4.1.2	H ₂ O Production via Seawater Reverse Osmosis.....	44
4.1.3	CO ₂ Capture via Bipolar Membrane Electrodialysis (BPMED).....	46
4.2	Integrated System II: Solar Methanol Synthesis via E-CEM H ₂ and CO ₂	47

4.2.1	H ₂ and CO ₂ Capture from Seawater via E-CEM Reactor	47
CHAPTER 5: Analysis and Modeling		49
5.1	Introduction	49
5.2	Thermodynamic Analyses	49
5.2.1	Thermophysical Properties of Material Streams	51
5.3	Energy and Exergy of Solar Insolation	52
5.3.1	Solar Concentration and Spectrum Splitting	53
5.4	Electrochemical Modeling of the PEC Reactor	55
5.3.2	PV Electricity Generation	58
5.5	CPV-PEC Component and Integrated System Efficiencies	60
5.6	Analysis of Integrated Systems for Solar Fuel Synthesis	62
5.6.1	Methanol Synthesis Plant	62
5.6.2	Freshwater Production via Seawater Reverse Osmosis (SWRO)	64
5.6.3	CO ₂ Capture from Seawater	65
5.6.4	Energy and Exergy Efficiencies of Integrated Systems	66
5.7	Exergoeconomic Analysis	67
5.8	Exergoenvironmental Analysis	69
5.9	Optimization	70
CHAPTER 6: Results and Discussion		74
6.1	Introduction	74
6.2	CPV-PEC Experimental Results and Model Validation	74
6.2.1	Solar Concentration and Spectrum Splitting	75
6.2.2	Experimental PEC Reactor and PV Results	80

6.2.3	Integrated CPV-PEC Performance	92
6.2.5	CPV-PEC Exergoeconomic Results	97
6.2.6	CPV-PEC Optimization	99
6.3	Integrated System Results	105
6.3.1	Aspen Plus Results for Methanol Synthesis Plant	106
6.3.3	System I Case Study Results.....	110
6.3.4	System II Case Study Results	112
CHAPTER 7: Conclusions and Recommendations		116
7. 1	Conclusions	116
7.2	Recommendations	116
References		118

LIST OF TABLES

Table 1.1: Renewable based solar-H ₂ production processes	4
Table 1.2: Comparison of H ₂ storage methods.	5
Table 1.3: Energy requirements for various seawater desalination methods.....	11
Table 2.1: Solar thermal collector types and operating ranges.	17
Table 2.2: CPV Technologies	20
Table 3.1: Proton exchange membrane specifications.....	32
Table 3.2: Spectrum splitting dielectric mirror specifications.....	35
Table 3.3: Characteristics of the SC6-18V Solar PV module.....	36
Table 3.4: Measurement device accuracy and range.	41
Table 4.1: SWRO desalination plant operating characteristics.	45
Table 5.1: Gas phase heat capacity inputs for Shomate Equation.	52
Table 5.2: Mass, energy, entropy, and exergy balance equations of common components.	62
Table 5.3: Equipment coefficients for purchase cost estimations.....	69
Table 6.1: Measurement Uncertainties	75
Table 6.2: Solar insolation values for measured aperture (lens) and concentrated values.	80
Table 6.3: PV electricity generation and efficiencies for the experimental cases.	91
Table 6.4: CPV-PEC component energy and exergy input.	97
Table 6.5: Capital cost of PEC Reactor.	98
Table 6.6: Capital cost of integrated CPV-PEC.....	99
Table 6.7: Parameters used to generate the objective function through neural network.	100

Table 6.8: The results of the multi-objective optimization.....	104
Table 6.9: State points for Aspen Plus methanol plant.....	107
Table 6.10: Component work, entropy generation, and exergy destructions for 1 kmol/hr CH ₃ OH production.....	108
Table 6.11: Subsystem energy consumption for System II.	113

LIST OF FIGURES

Figure 1.1: Energy consumption by energy source, 1990-2040 (data from [2]).	2
Figure 1.2: Methanol demand for industrial and fuel applications in 2013 (data from [17])	7
Figure 1.3: Dynamic equilibrium of atmospheric and ocean CO ₂ (adapted from [19]).	9
Figure 1.4: Solar-based seawater desalination processes.	10
Figure 2.1: High-temperature heliostat field CSP plant.	18
Figure 2.2: Dish engine solar thermal collector.	18
Figure 2.3: PV electricity generation (left), and PV/T panel array (right).	19
Figure 2.4: (a) Electrolysis and (b) photochemical cells (adapted from [30]).	21
Figure 2.5: Schematic and electrode reactions for (a) alkaline electrolyser and (b) PEM electrolyser cells.	22
Figure 2.6: Photobiological H ₂ and CO ₂ conversion by algae for biomass production in raceway pond and flat plate photobioreactors.	23
Figure 2.7: Renewable methanol production pathways (adapted from [40])	25
Figure 2.8: Bandgap of various semiconductors for PEC water splitting applications (data from [44] [45] [46] [47]).	27
Figure 2.9: Band edges (conduction lower and valence top) for various semiconductor materials (data from [44] [45] [46] [47])	27
Figure 3.1: CPV-PEC H ₂ reactor and solar splitting apparatus outside of CERL Solarium.	29
Figure 3.2: Arrangement of main CPV-PEC components.	30

Figure 3.3: Assembled PEC reactor photocathode (left) and anode (right) compartments.	31
Figure 3.4: Custom profile design of stainless steel plates for PEC reactor, (a) cathode, and (b) anode.	32
Figure 3.5: CAD model of PEC reactor (a) cathode compartment, (b) anode compartment, (c) membrane electrode assembly.....	33
Figure 3.6: (a) Concentrating Fresnel lens, and (b) mounting arrangement of the dielectric mirror, PEC, and PV components in the CPV-PEC experimental setup.	34
Figure 3.7: Dielectric mirror array.....	35
Figure 3.8: Sunwize 6 W PV Module.....	36
Figure 3.9: Gamry Reference 3000 (a) Potentiostat, (b) 30K Booster (images adapted from [54]).....	37
Figure 3.10: (a) TriSol Class AAA Solar Simulator [55], (b) solar simulator in experimental setup for photocathode characterization in simulated light.	38
Figure 3.11: Electrodeposition of Cu_2O film on stainless steel cathode plate.....	39
Figure 3.12: Stainless steel cathode plate before (left) and after (right) Cu_2O electrodeposition process.	40
Figure 4.1: System I processes, power, and material flows.....	43
Figure 4.2: Methanol synthesis plant (adapted from [63]).	44
Figure 4.3: SWRO desalination plant (adapted from [64]).....	45
Figure 4.4: Schematic of BPMED unit for CO_2 from seawater (adapted from [65]).	46
Figure 4.5: System II processes, power, and material flows.	47
Figure 4.6: Electrolytic cation exchange membrane (adapted from [66]).	48

Figure 5.1: Simplified circuit diagram of a PV cell.....	60
Figure 6.1: Spectral irradiance levels (ASTMG173 spectra data from [89]).	76
Figure 6.2: Direct beam spectral irradiance for dielectric mirror range.	76
Figure 6.3: Concentrated direct solar irradiance for mirror, PV, and PEC surfaces.....	77
Figure 6.4: Measured intensity (counts) of concentrated sunlight (a) reflected, and (b) transmitted by dielectric mirror.	78
Figure 6.5: Measured reflectance and transmittance of the dielectric mirror concentrated light conditions.....	79
Figure 6.6: Measured and theoretical reflected solar irradiance onto PEC photocathode.	79
Figure 6.7: Photocurrent (J_{photo}) and photovoltage (V_{photo}) for J-V voltammograms of Cu_2O coated stainless steel photocathode plate (0.05 M NaOH electrolyte) under dark and simulated light conditions (1000 W/m^2 AM 1.5G).....	81
Figure 6.8: Partial illumination of Cu_2O coated stainless steel photocathode plate (0.05 M NaOH electrolyte) to simulated sunlight (1000 W/m^2 AM1.5)......	82
Figure 6.9: Photocathode testing under concentrated solar illumination.....	82
Figure 6.10: Cyclic voltammetry curve of Cu_2O photocathode plate in 0.05 M NaOH electrolyte solution under dark and concentrated light conditions.	83
Figure 6.11: Linear sweep voltammetry for Cu_2O coated photocathode plate in 0.05 M NaOH electrolyte solution under chopped concentrated light.	84
Figure 6.12: Measured current at 1.6 V for PEC operation under shadowed (low light) and concentrated solar concentration.....	85
Figure 6.13: Measured H_2 production at 1.6 V for PEC operation under shadowed (low light) and concentrated solar concentration.	85

Figure 6.14: Measured current at 1.8 V for PEC operation under shadowed (low light) and concentrated solar concentration.....	86
Figure 6.15: Measured H ₂ production at 1.8 V for PEC operation under shadowed (low light) and concentrated solar concentration.	86
Figure 6.16: Measured current at 2.0 V for PEC operation under shadowed (low light) and concentrated solar concentration.....	87
Figure 6.17: Measured H ₂ production at 2.0 V for PEC operation under shadowed (low light) and concentrated solar concentration.	88
Figure 6.18: Measured current at 3.0 V for PEC operation under shadowed (low light) and concentrated solar concentration.....	88
Figure 6.19: Measured H ₂ production at 3.0 V for PEC operation under shadowed (low light) and concentrated solar concentration.	89
Figure 6.20: Experimental I-V and P-V curves for PV module under ambient sunlight..	90
Figure 6.21: Experimental I-V and P-V curves for PV module under concentrated sunlight.	90
Figure 6.22: Experimental I-V and P-V curves for PV module under concentrated sunlight with spectrum-splitting.	91
Figure 6.23: Variation of membrane conductivity (σ) and resistivity (R) with operating temperature at $J = 100 \text{ mA/cm}^2$	92
Figure 6.24: Variation of modeled cell overpotentials with operating temperature for PEM electrolysis ($J=100 \text{ mA/cm}^2$).....	93
Figure 6.25: Variation of cell overpotentials with current density for PEM electrolysis model ($T=303 \text{ K}$, $P=1 \text{ atm}$).....	94

Figure 6.26: Effect of current density on work input and exergy destruction for PEM electrolysis.	94
Figure 6.27: Effect of operating temperature on PEM energy and exergy efficiencies (J=100 mA/cm ²).	95
Figure 6.28: Variation of PEM energy (η) and exergy (ψ) efficiencies with current density (V=2 V).	96
Figure 6.29: Energy and exergy inputs to each component of the CPV-PEC.	97
Figure 6.30: Exergoeconomic factor of integrated CPV-PEC reactor for different interest rate scenarios.	99
Figure 6.31: Considered parameters and the corresponding PV power output used to train the neural network in generating the objective function.	101
Figure 6.32: Considered parameters and the corresponding exergy efficiency of the PV used to train the neural network in generating the objective function.	101
Figure 6.33: Considered parameters and the corresponding energy efficiency of the PV used to train the neural network in generating the objective function.	102
Figure 6.34: Considered parameters and the corresponding energy efficiency of the concentrator used to train the neural network in generating the objective function.	102
Figure 6.35: Error histogram of the trained, validated and tested objective function of the proposed system.	103
Figure 6.36: Performance of the model with the iterations through the training of the objective function.	104
Figure 6.37: Regression plots of the generated models against the supplied data.	105
Figure 6.38 Aspen Plus flowsheet of methanol synthesis plant.	106

Figure 6.39: Exergy destruction fraction of methanol plant components.....	109
Figure 6.40: CO _{2e} balance of methanol plant components.	109
Figure 6.41: Exergoeconomic factor of methanol synthesis plant for different interest rate scenarios.....	110
Figure 6.42: Variation of energy and exergy efficiencies of the integrated system with the solar irradiation.	111
Figure 6.43: Effect of area of the collector on the energy and exergy efficiencies of the integrated system.	111
Figure 6.44: Effect of environmental temperature on System II energy and exergy efficiencies.	114
Figure 6.45: Effect of E-CEM specific-work reduction on total electricity consumption by SWRO, E-CEM, and methanol plant subsystems.....	114
Figure 6.46: Effect of E-CEM specific-work reduction on electricity-to-methanol (dashed lines), and solar-to-methanol (solid lines) energy and exergy efficiencies.	115

NOMENCLATURE

A	Area (m^2)
b	Specific Environmental Impact Factor (Pts/GJ)
\dot{B}	Environmental Impact Rate (Pts/s)
c	Cost per Unit of Exergy (\$/GJ)
\dot{C}	Cost rate (\$/s)
CR	Solar Concentration Ratio (Suns)
E	Energy (kJ)
E°	Standard Cell Potential (V)
Ex	Exergy (kJ)
ex	Specific Exergy (kJ/kg)
\dot{Ex}	Exergy Rate (kW)
\dot{Ex}_d	Exergy Destruction Rate (kW)
g	Specific Gibbs Free Energy (kJ/kg)
\bar{g}	Molar Specific Gibbs Free Energy (kJ/kmol)
G	Solar Insolation (W/m^2)
h	Specific Enthalpy (kJ/kg)
H	Enthalpy (kJ)
I	Solar Insolation (W/m^2)
m	Mass (kg)
\dot{m}	Mass Flow Rate (kg/s)
M	Molar Mass (kg/kmol)
n	Moles (kmol)
\dot{n}	Molar Flow Rate (kmol/s)
P	Pressure (kPa)
Q	Heat (kJ)
\dot{Q}	Heat Rate (kW)
s	Specific Entropy (kJ/kg·K)
\bar{s}	Molar Specific Enthalpy (kJ/kmol·K)

\dot{S}_{gen}	Entropy Generation Rate (kW/K)
T	Temperature (°C or K)
\dot{Y}	Component Related Environmental Impact (Pts/s)
\dot{Z}	Component Related Cost Rate (\$/h)

Greek Letters

η	Energy Efficiency
ρ	Density (kg/m ³)
σ	Uncertainty
ψ	Exergy Efficiency
θ_i	Solar Incident Angle (deg.)

Subscripts

ap	Aperture
el	Electric
in	Input flows
out	Output flows
P	Product
R	Reaction or Reactant

Superscripts

ch	Chemical
ph	Physical

Physical constants

F	Faraday's Constant 96,485 s·A/mol
I_{sc}	Average Solar Constant Insolation 1373 W/m ²
R_u	Universal Gas Constant 8.314 kJ/kmol·K
T_s	Sun Temperature 5762 K

Acronyms

BPMED	Bipolar Membrane Electrodialysis
CCS	Carbon Capture and Storage
CPV	Concentrated Photovoltaic
CSP	Concentrated Solar Power

EBE	Energy Balance Equation
E-CEM	Electrolytic-Cation Exchange Membrane
EnBE	Entropy Balance Equation
ExBE	Exergy Balance Equation
GHG	Greenhouse Gas
MBE	Mass Balance Equation
PEC	Photoelectrochemical
PEM	Proton Exchange Membrane
PV	Photovoltaic
TES	Thermal Energy Storage
UOIT	University of Ontario Institute of Technology

CHAPTER 1: INTRODUCTION

1.1 World Energy and Environmental Outlook

Increasing energy demand with world population growth and development, and the environmental consequences of excessive fossil fuel consumption to meet this demand, are primary factors behind global initiatives for the implementation of more environmentally benign energy options. Sustainable development of alternative energy options requires both short and long-term solutions in order to reduce fossil fuel dependence, and mitigate the negative environmental impacts resulting from their use.

In particular, reduction of greenhouse gas emissions resulting from fuel combustion in the transport and the electricity and heat sectors—responsible for more than 23% and 42% of global carbon dioxide (CO₂) emissions in 2014, respectively [1]—is a critical international issue. Furthermore, though there is debate over the rate of depletion of fossil fuel reserves, the fact remains that these resources will eventually run out. It is critical to investigate alternative resources and energy systems that are sustainable, more environmentally benign, and practical for implementation within today's energy infrastructures.

Projections shown in Figure 1.1 for energy consumption by energy source in [2] suggest a promising trend for renewable energies over the next two decades. However they also imply that the demand for fossil fuels for transportation and power generation (liquid fuels and natural gas) will also continue to rise steadily. Developing sustainable alternatives that can directly replace these high-demand fossil fuels by conversion of renewable energies and sustainable resources to form carbon-neutral and carbon-free synthetic fuels

will help ease transition away from fossil fuel energy dependence, towards renewable energy infrastructures and the eventual hydrogen economy.

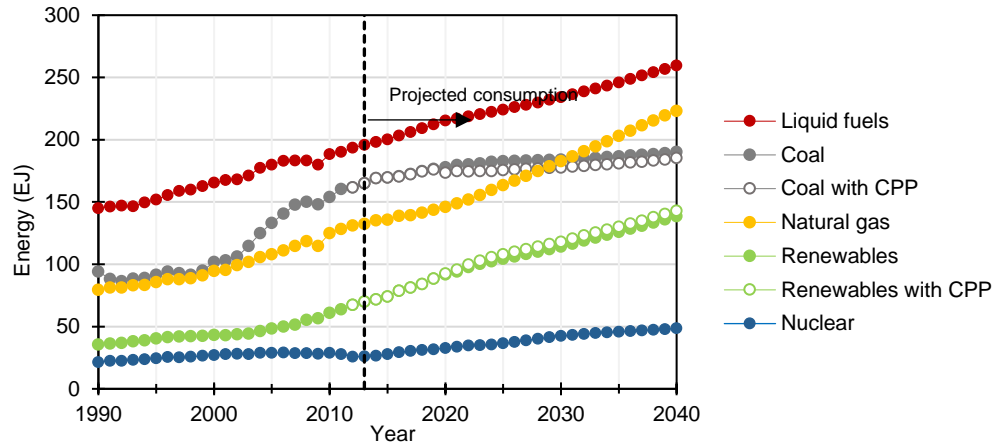


Figure 1.1: Energy consumption by energy source, 1990-2040 (data from [2]).

Renewable resources, such as solar, wind, and geothermal, supply environmentally benign energy for power (electricity) generation, but face practical challenges as direct alternatives to equivalent capacity fossil fuel applications with respect to resource availability/stability, system size (i.e. land space requirement), and economics (i.e. energy cost). Conversion of renewable resources into secondary carriers, such as electrical (i.e. batteries), mechanical (i.e. water pumping), thermal, or chemical (i.e. hydrogen) media, stores green energy in useful, practical forms and manages the issue of intermittent energy availability [3].

1.2 Solar Energy

The Sun is the most abundant renewable energy source on this planet; just 1% of the available solar energy that reaches Earth's surface is sufficient to meet global energy demands [4]. Photonic and thermal energy from the sun is converted to electricity and or heat using photovoltaic (PV) and solar-thermal collectors. Heat energy may be converted

to electricity, stored in various thermal energy storage (TES) systems, or used directly as process heating in a wide array of thermal applications, including hydrogen (H_2) production processes from either electricity or heat. The intermittent nature of sunlight—which varies with time of day, weather conditions, season, global position, and reference (environment) temperature—necessitates the integration of energy conversion and storage mediums in order to effectively harvest solar energy and provide a stable supply to consumers.

One of the major challenges of collecting solar energy is the significant PV surface area and equipment cost to capture incident solar flux sufficient for large capacity power generation applications. Solar collector technology is progressing in two major areas: concentrating solar flux on a receiver area, and in semiconductor material and structure technologies to increase absorption of the solar energy spectrum in PV and photoelectrochemical systems. Spectrum splitting devices, such as mirrors and lenses, use dielectric coating materials to reflect and transmit certain wavelengths of light. Solar energy conversion applications that utilize photoactive materials can take advantage of this by spectrum-matching dielectric coatings to a specific process according to the most suitable bandgap and wavelength range, and use the remaining solar spectrum for power or heat generation to increase the overall efficiency.

1.3 Hydrogen

Hydrogen (H_2) is an ideal energy carrier [5]; it is able to be produced from and converted to electricity with good efficiency, and can be converted into other energy forms more efficiently than any other fuel. Furthermore, H_2 emits no pollutants in combustion, and can be sustainably produced using renewable energy sources of electricity and or heat, with water as the input.

1.3.1 Renewable Hydrogen Production Methods

Current methods for H₂ production primarily utilize non-renewable sources as energy and material inputs. Steam reforming of natural gas or light oil account for over 95% [6] of H₂ production. Table 1.1 provides an overview of solar-H₂ production processes by [7] that utilize only renewable material resources, and the main water splitting processes are discussed in further detail in Chapter 2.

Table 1.1: Renewable based solar-H₂ production processes

Solar energy	H ₂ process	Material inputs	Process description
Thermal	Thermolysis	Water	Thermal dissociation of water ($T > 2500$ K)
	Thermo-catalysis	H ₂ S	Cracking of H ₂ S extracted from seas or industrial processes
		Biomass	Thermo-catalytic biomass conversion to H ₂
	Thermochemical	Biomass	Gasification of biomass converted to syngas; H ₂ extracted
		Water	Cyclical chemical reactions (w/ or w/o redox reactions) split water molecule.
Photonic	PV-electrolysis	Water	PV generated electricity drives electrolyser
	Photo-catalysis		Catalysts or molecular devices with photo-initiated electrons collection generate H ₂ from water
	Photo-electrochemical		Hybrid cell generates PV electricity for water electrolysis
Potential + Thermal	High temperature electrolysis	Water	Water splitting in solid oxide electrolyte cells
Potential + Photonic	Photo-electrolysis	Water	Photo-electrodes + electricity
Photo-biological	Artificial photosynthesis	Biomass, water	Bacteria and microbes photo-generate H ₂
	Bio-photolysis		Biological systems based on cyanobacteria generate H ₂
	Photo-fermentation		Fermentation process facilitated by light exposure

Source: [7]

Note: Electricity generated from solar.

1.3.2 Hydrogen Storage

The characteristics of the main storage options are given in Table 1.2. Hydrogen is the lightest element and requires either large volumes, high pressure, low temperature, or

advanced material storage techniques to hold sufficient fuel for practical operating range [8]. This is particularly relevant in light duty passenger vehicles since the low volumetric energy density of H₂ requires large volume, high pressure storage tanks to achieve driving range comparable to that of vehicles consuming traditional transportation fuels [9].

Table 1.2: Comparison of H₂ storage methods.

Storage method	Energy Intensity (MJ/kg-H ₂)	wt%-H ₂ per tank	wt%-H ₂ /kg-system	g-H ₂ / tank	g-H ₂ /L-system
Compressed H ₂ (35 MPa)	10.2	6	4-5	20	15
Liquid H ₂	28-45	20	15	63	52
Low Temperature Hydrides (T<100°C)	10-12	2	1.8	105	70
High Temperature Hydrides (T>300°C)	20-25	7	5.5	90	55

Source: [10]

Before the realization of a hydrogen economy, innovative solutions for efficient storage methods require development—there are challenges to storing such a small molecule, and current storage methods, such as cryogenic, liquefaction, compression, and metal hydrides are energy intensive and can be prohibitive in practical application.

1.4 Solar Energy and H₂ Storage in Synthetic Fuels

Conversion and storage of solar energy and renewable H₂ in chemical forms, such as methanol, ammonia biofuels, and synthetic natural gas provides a stable supply of renewable energy in practical media that are suitable to supply a wide range of power generation applications; for example, gas turbine power plants, internal combustion engines, and fuel cells. In addition to their use as combustion fuels for power generation and transportation applications, various hydrocarbon derivatives from fossil fuels are feedstock for products, such as synthetic textiles, plastics, and for synthesis of pharmaceutical and industrial chemicals [11].

1.4.1 Potential Solar Fuel Options

Synthetic Hydrocarbons and Biofuels

Synthetic and biomass derived hydrocarbons, such as synthetic natural gas (SNG) and biomethane (CH_4), biogas, and biodiesel fuels can directly replace their fossil fuels counterparts in power generation and transportation applications with little or no modification required.

Renewable hydrocarbon biofuels can be produced from a wide variety of sustainable resources, such as vegetable oils and fats, cellulose (i.e. agricultural waste, wood), and sugars. in a number of processes [12] such as gasification, fermentation, and electrochemical processes.

Ammonia

Ammonia (NH_3) is a strong option as a sustainable alternative to hydrocarbon fuels for transportation applications [13]. From the review study by [14], the following points highlight particular advantages of NH_3 as a transportation fuel:

- High octane rating of NH_3 (110–130) make it suitable for ICE applications [15]
- Can be thermally decomposed into H_2 for fuel, and N_2 gas
- Compared to other fuels used in combustion applications, NH_3 has the highest hydrogen energy density—higher even than pressurized and liquefied hydrogen fuel, based on current storage methods [16]
- Contains no carbon, has a global warming potential (GWP) of zero, and produces only N_2 and H_2O when combusted.

Methanol

Methanol is a particularly useful chemical storage medium for solar and renewable energy. Methanol (CH_3OH), or methyl alcohol, is a colourless liquid that has a specific gravity of 0.789 at standard temperature and pressure, and thus does not require energy intensive storage. As a fuel, methanol can be used directly or in fuel mixtures in combustion engines, or to generate electricity in reverse fuel cells. As an industrial chemical, methanol is an important feedstock, primarily for formaldehyde and acetic acid production, as well as in fuel production. Worldwide annual production reached approximately 65 million metric tonnes in 2013 [17] to meet demand by industrial and commercial applications as shown in Figure 1.2.

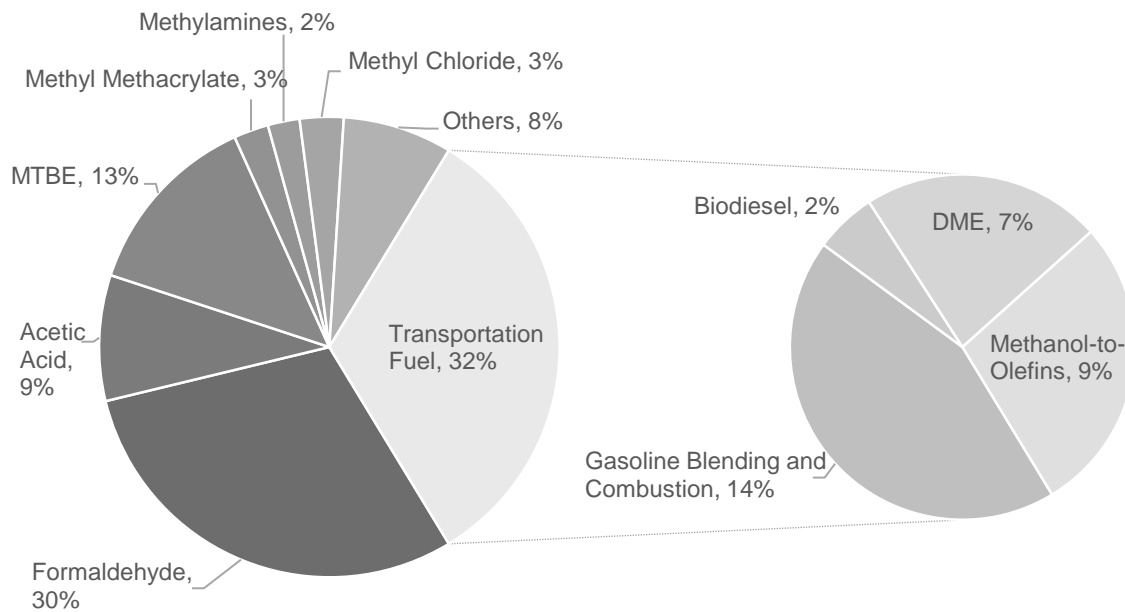


Figure 1.2: Methanol demand for industrial and fuel applications in 2013 (data from [17])

Though approximately two thirds (40 million tonnes; [18]) of methanol production processes utilize syngas from fossil fuel derivatives, environmentally benign fuel

production options are being actively investigated, including photoelectrochemical and photosynthetic processes to produce benign hydrocarbon fuels.

1.4.2 Resource Sustainability Considerations for Solar Fuel Synthesis

From a sustainability standpoint, it is interesting to note the interactions of solar fuel synthesis with three of Earth's most important global cycles: solar energy, hydrological, and carbon. Thermal and photonic energy from the Sun sustains all life on Earth—maintaining liveable climate conditions, as well as driving atmospheric and oceanic convective currents, the global water cycle, and photosynthesis processes in plant life. Humans and animals rely on these processes fundamentally for food (energy) and fresh water supply.

These biological lifecycle interactions are part of the carbon cycle in both short and long term in ways; CO₂ consuming plants become part of the food chain, and all organic matter returns carbon through decomposition. This decaying matter goes to geological deposits, and, under significant heat and pressure conditions, eventually becomes fossil fuel. Developing methods that reduce fossil fuel use and instead utilize renewable energy and sustainable resources to produce hydrogen and synthetic hydrocarbon fuels will help to reduce the negative human impacts of interrupting these natural cycles.

Oceans are a major part of the natural carbon cycle. CO₂ is in dynamic equilibrium with the atmosphere at the ocean surface, and transfers organic and inorganic carbon into ground deposits through sedimentation. Figure 1.3 describes the fast and slow cycle interactions of CO₂ in the ocean. At the ocean surface, atmospheric CO₂ dissolves in seawater, producing carbonic acid.

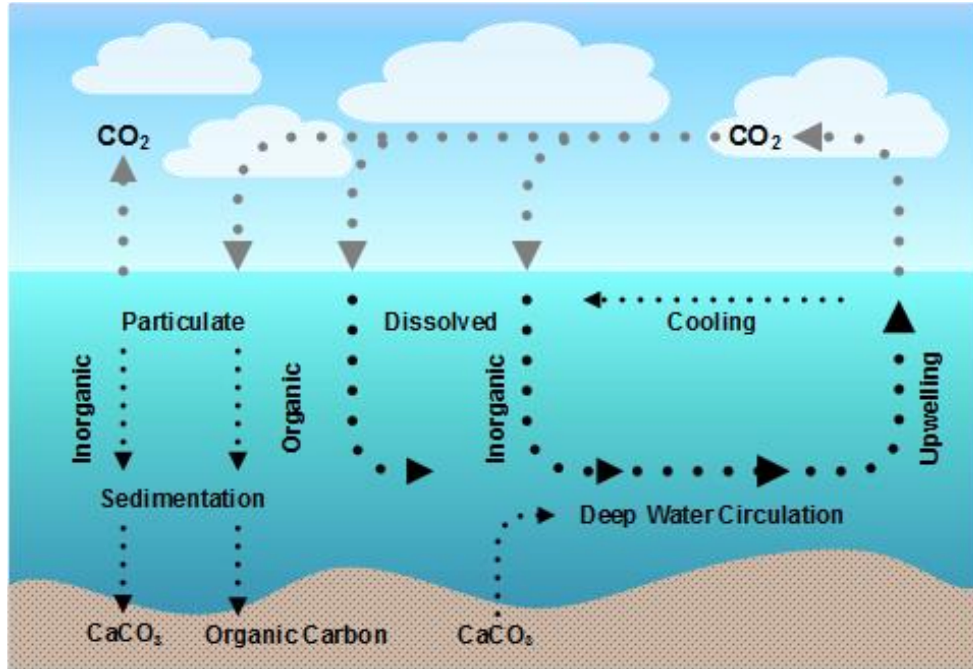


Figure 1.3: Dynamic equilibrium of atmospheric and ocean CO₂ (adapted from [19]).

Carbonic acid releases hydrogen ions that combine with carbonate, forming bicarbonate. Excess (anthropogenic) CO₂ in the carbon cycle is causing an increase in ocean temperature and acidification, negatively affecting marine animals and ecosystems [20]. Eventually, this may accelerate the release of carbonate from sediments and rocks, which will cause the ocean to absorb CO₂ even more quickly [21]. As a carbon source for fuel production, seawater holds 0.1 kg-CO₂ per m³, which is 140 more than that of air. This, along with the negative implications of CO₂ excesses in the World's oceans, is a strong incentive to explore carbon capture options for seawater.

Solar Desalination

Oceans cover 71% of Earth's surface, and represent 97% of Earth's water supply [22]. Desalination of seawater provides clean water for human consumption, sanitation, and industrial processes without depleting natural freshwater resources. Figure 1.4 summarizes

solar-based options for commercial desalination technologies in two categories: thermal distillation, and membrane separation. In thermal distillation methods, such as multi-stage flash (MSF) and multi-effect distillation (MED), changes in the pressure and temperature of seawater cause freshwater to evaporate and condense as a distillate. Membrane separation methods, such as reverse osmosis (RO), use pressure gradients across a semi-permeable membrane to filter out undesired salt and minerals dissolved in seawater.

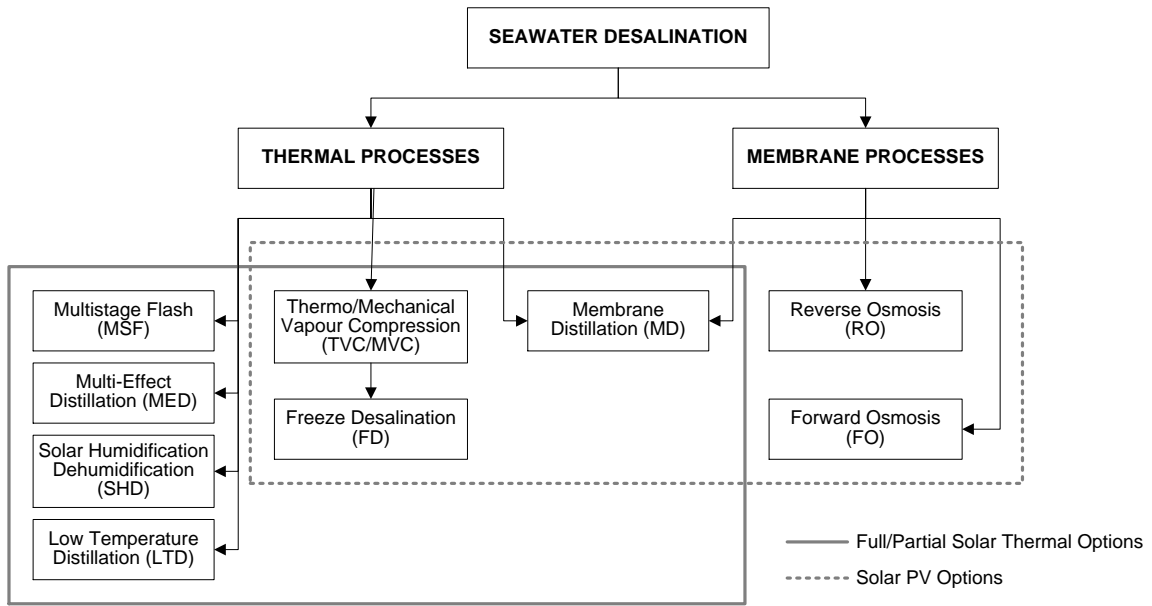


Figure 1.4: Solar-based seawater desalination processes.

Reverse osmosis is the dominant method for seawater desalination, representing 80% of desalination plants worldwide [23], due in part to its relatively low capital cost and energy consumption, and that it does not require thermal input. Furthermore, RO desalination processing is modular; combination of multiple units in a range of capacities makes this technology highly flexible [24]. Typical power consumption of various methods for seawater desalination are given in Table 1.3.

Table 1.3: Energy requirements for various seawater desalination methods

Method	Electrical (kWh/m ³)	Thermal (kWh/m ³)	Total (kWh/m ³)
Reverse osmosis (RO)	3 – 3.5	0	3 – 3.5
Multistage flash distillation (MSF)	4 – 6	9.5 – 21.5	13.5 – 25.5
Multi-effect desalination (MED)	1.5 – 2.5	5 – 8.5	6.5 – 11
MED with thermal vapour compression (MED-TVC)	1.5 – 2.5	0	11 – 28
Mechanical vapour compression (MVC)	7 – 12	0	7 – 12

Source: [25]

1.5 Motivation

In order to shift resource utilization away from fossil fuels, practical alternatives that are feasible within current infrastructures are necessary to bridge the gap toward renewable energies and the eventual hydrogen economy. There is extensive research in the area of renewable hydrogen and fuel production, as well as economic and environmental assessments of solar energy driven hydrogen processes that maximize solar density and spectrum utilization with concentration technologies, advanced PV materials, and spectrum-splitting technologies.

Increasing solar-to-hydrogen efficiency and system feasibility requires certain challenges to be addressed: multiple conversion processes from solar resource to final H₂ product reduces overall efficiency with each conversion step. Developing technologies that offer a more direct route from resource to product, such as with photoelectrochemical H₂ production, helps reduce losses due to energy conversion processes. However, much of the research into direct photo-conversion processes use rare Earth materials (such as platinum) that are unsustainable both economically and environmentally. Utilization of sustainable materials for both the photoactive elements and components of the integrated system will

help to make PEC H₂ more feasible. Furthermore, responsible material resource selection for the water source to supply the process should focus on non-freshwater resources such as seawater – which is an essentially unlimited resource - or wastewater resources. Limited freshwater resources must not become a commodity for energy processes.

Lastly, the storage of H₂ is energy intensive. Integrating chemical conversion to a liquid fuel, such as methanol, provides a stable format for storage and transportation of solar-H₂ that is useable in modern infrastructures in direct combustion and fuel cell applications, and as an industrial chemical feed stock material.

1.5.1 Novelty and Originality

The development of the integrated CPV-PEC experimental system in this study addresses key challenges of solar energy utilization, hydrogen production, and resource sustainability.

In terms of solar utilization and solar-to-hydrogen efficiency, the application of solar concentration with spectrum splitting improves conversion efficiency by using a larger range of the solar spectrum. This also addresses issues of system footprint by producing two outputs simultaneously (H₂ and electricity) from a single solar input. The custom-built PEC reactor is specifically designed to utilize solar energy with a large area Cu₂O photocathode, which is an abundant and inexpensive photoactive material. The large area membrane (> 900 cm²) takes advantage of the higher current density capability associated with PEM electrolysis to increase hydrogen production. By design, the photocathode and anode electrode plates for the PEM electrolyser act as a skeleton-type support for the large area membrane to prevent damage and shifting due to pressure

differential between the anode and cathode compartments, as well as to direct bubble flow upwards and away from the active surfaces through small channels.

As an integrated system, the experimental CPV-PEC setup uses low-cost and repurposed materials wherever possible. The Fresnel lens is salvaged from a rear-projection television obtained at no cost (though the cost may range approximately \$50-\$100 depending on local availability), and uses a low-cost single-junction Si PV module. The reactor body is built from high-density polyethylene (HDPE), which is an inexpensive and recyclable thermoplastic. As a very common plastic for food and beverage containers, shopping bags, and other products packaging, there is a significant supply of free HDPE stock (waste) material, and with its low melting point (~ 125 °C) it is feasible to construct simple casting molds to produce customized reactor housings from waste materials at minimal cost. Identifying cost efficient and sustainable solutions for the experimental setup allows allocation of system cost to more critical components (i.e. PEM, dielectric mirrors), and helps to improve economy of scale for small-capacity systems for other researchers or consumer applications.

1.6 Objectives

This research will apply comprehensive thermodynamic, exergoeconomic, and exergoenvironmental analyses, as well as a multi-objective optimization study for efficient, sustainable, and feasible solar fuel synthesis options that can directly replace or reduce fossil fuel utilization in combustion (power generation, transportation), and as a valuable industrial chemical commodity.

The aim of this thesis study is to experimentally and theoretically investigate hydrogen and methanol production that utilize solar energy, and sustainable material inputs—i.e. ocean and anthropogenic CO₂. The specific objectives of this research include:

1. To develop novel integrated solar energy systems that utilize sunlight for hydrogen and power generation, and fuel synthesis from anthropogenic CO₂ and sustainable water resources:

- CPV electricity production using seawater as H₂ and CO₂ resource for methanol synthesis plant.
- Concentrated sunlight is split into high and low energy wavelengths via dielectric mirror for simultaneous PV electricity and photoelectrochemical hydrogen generation.
- Investigate fuel options, such as ethanol, ammonia, and biofuels.

2. To build and test an experimental set-up for solar-driven hydrogen production:

- Electrodeposition of photoactive Cu₂O on cathode of electrolyser unit with testing of experimental prototype for photoelectrochemical (PEC) hydrogen production
- Perform experimental testing of integrated PEC and PV cells using solar spectrum splitting under simulated and concentrated natural sunlight for investigation of hydrogen production and electricity generation rates.

3. To conduct comprehensive energy and exergy analyses of the experimental and integrated system configurations:

- Definition of mass, energy, entropy, and exergy balance equations for the individual components, subsystems, and reactions.

- Thermodynamic modeling using Engineering Equation Solver to evaluate the properties and rates of the various streams, and exergy destructions for the components, subsystems, and reactions.
4. To conduct simulations of the methanol fuel synthesis reactor.
 - Evaluation of the mass, energy, and exergy flows for the methanol fuel system to determine total heat and electrical work demand.
 - Conduct parametric studies to observe the effect of varying operating conditions (i.e. temperature, pressure) and environmental conditions on the energy and exergy efficiency of the subsystems and the integrated systems.
 5. To conduct exergoeconomic assessments of the integrated system, including:
 - Determination of total exergy cost rate.
 - Determination of exergoeconomic factor.
 6. To perform a multi-objective optimization of the integrated CPV-PEC system by defining the objective functions and constraints for thermodynamic assessment
 - Determination of optimum conditions for energy and exergy efficiency of the CPV-PEC system

CHAPTER 2: BACKGROUND AND LITERATURE REVIEW

2.1 Introduction

This chapter is presented in two parts: first, an overview of solar energy conversion for power generation, chemical conversion for H₂ production, and fuel synthesis options for conversion of H₂ and CO₂ highlight the applications and technologies for utilization of solar thermal and photonic energies. Following this, a literature review of photoelectrochemical hydrogen production is given, including a survey of current photoactive materials research and experimental studies is given to support the experimental investigation of this thesis work. Based on the review, certain gaps in the literature are identified as areas of research that will benefit from this thesis study and its results.

2.2 Solar Energy Conversion

Direct solar energy conversion to heat (and indirect power), photovoltaic electricity, and chemical produce useable, practical forms of energy that can be used for everyday applications. The methods discussed here represent some of the more mature solar conversion processes and technologies found in literature and in use.

2.2.1 Solar Power Generation

Concentrated Solar Power (CSP)

Thermal energy is captured using CSP collectors, which transfer heat at high temperature to circulating fluids. These types of collectors use optical concentration to increase the solar radiative flux without significantly increasing thermal losses [26]. The general types and operating condition ranges for solar thermal collectors are outlined in Table 2.1.

Table 2.1: Solar thermal collector types and operating ranges.

Motion	Collector type	Absorber type	CR	Temperature (°C)
Stationary	Flat plate collector	Flat	1	30 – 80
	Evacuated tube collector	Flat	1	50 – 200
	Compound parabolic collector	Tubular	1 – 5	60 – 240
Single-axis tracking	Linear Fresnel reflector	Tubular	10 – 40	60 – 250
	Parabolic trough collector	Tubular	15 – 45	60 – 300
	Cylindrical trough collector	Tubular	10 – 50	60 – 300
Two-axes tracking	Parabolic dish reflector	Point	100 – 1000	100 – 500
	Heliostat field collector	Point	100 – 1500	150 – 2000

Source: [27]

A review by [28] presents the operating conditions for pilot and commercial CSP plants, including parabolic trough, dish-engine, and central receiver systems. Parabolic collectors are 2-D systems that focus incident solar radiation onto a receiver mounted along a focal line using single-axis tracking mirrors. The temperature of the thermal fluid circulated in the absorber tube can reach 500 °C, and thermal power ranging from 30—700 MW for systems with concentration ratios ranging from 30—80, making these CSP systems suitable for steam Rankine cycle power generation.

The central receivers and dish-engine collectors are 3-D concentrating systems that focus incident radiation onto a solar receiver. Central receiver systems employ two-axis tracking heliostats to focus solar radiation onto a tower-mounted receiver. Compared to parabolic trough systems, central receivers have a similar thermal power output range, but higher temperature range of the heat transfer fluid ($500 < T < 2000^{\circ}\text{C}$), and significantly higher concentration ratios ($200 < \text{CR} < 1000$), making central receiver collectors suitable for various thermochemical and advanced thermodynamic cycles.

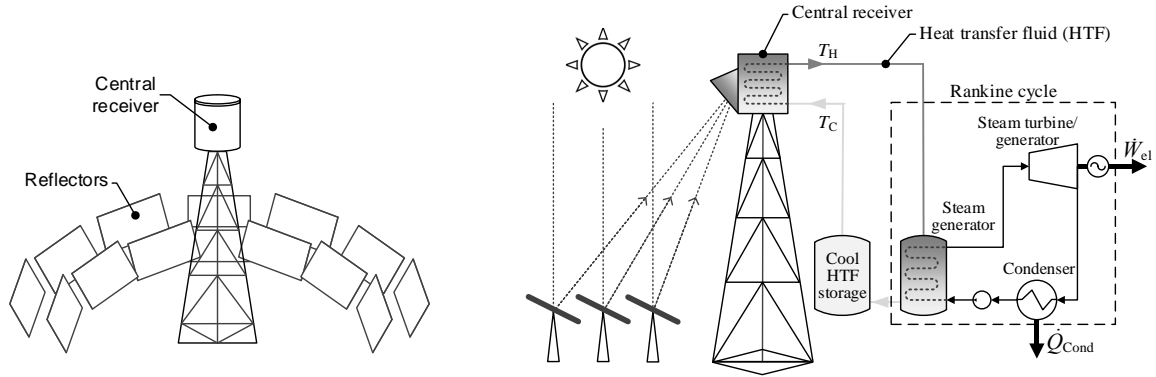


Figure 2.1: High-temperature heliostat field CSP plant.

Dish engine systems are smaller, single unit collectors combine a two-axis tracking parabolic concentrator with a Stirling or Brayton mini-turbine housed in the receiver. These systems are useful in remote and off-grid power systems in the range of 5—25 kW [26].

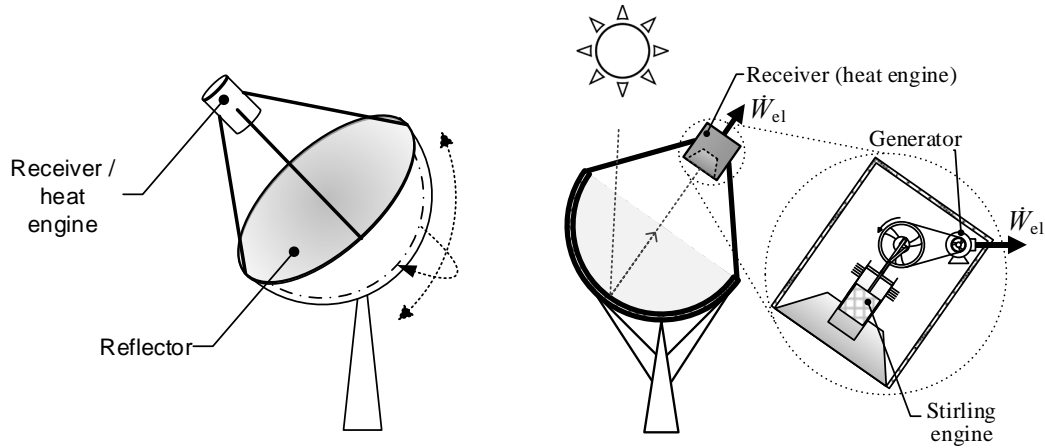


Figure 2.2: Dish engine solar thermal collector.

Photovoltaic (PV) Electricity Generation

The photoelectric effect describes the conversion of photonic energy to electricity. PV cells absorb sunlight, transferring energy to electrons within the atoms of a semiconductor material (traditionally silicon), causing them to escape from their positions. Imposing a charge imbalance between two semiconducting materials layers of the cell produces an

electric field that directs the flow of electrons (current) in an electric circuit. Figure 2.3 shows the general structure of a PV cell and circuit. Doping each of the semiconductor layers with other materials such that one layer is electron-rich (n-type layer) and the other is electron-poor (p-type layer) maintains the charge imbalance for passage of electrons to take place. Combining multiple PV cells in a module or panel is necessary to collect sufficient energy for useful electricity production, and larger systems are scalable by assembling a number of modules in an array with or without heat collection.

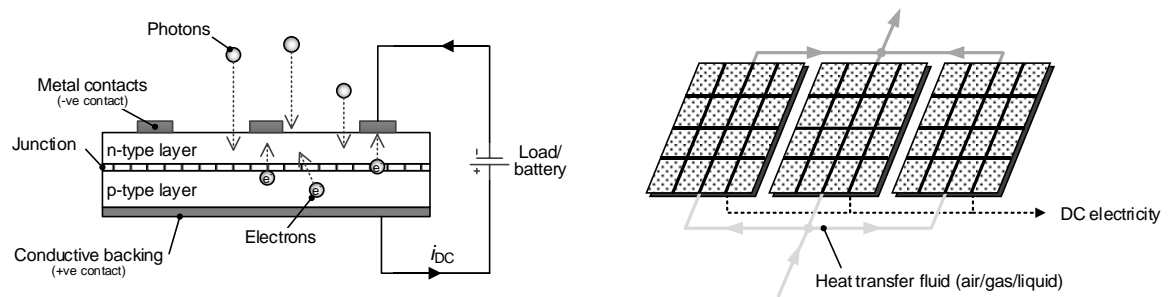


Figure 2.3: PV electricity generation (left), and PV/T panel array (right).

Concentrated PV (CPV) power generation is an attractive option for large capacity electricity production. Multi-junction cell technologies are rapidly improving PV cell efficiencies by taking advantage of the different bandgaps of semiconductor materials to maximize the range of the solar spectrum absorption by stacking different materials in sequence. In the work by [29], the authors summarize several CPV technologies, listed in Table 2.2. It is important to note that the cost of high efficiency PV cells requires concentration to make these options economically viable.

Table 2.2: CPV Technologies

Manufacturer	Cell Technology	Concentration Factor, C	Efficiency, η_{PV}	Power Density (W/m ²)	
				Cell	Aperture
ENTECH	GaIn/GaAs/Ge submodule	10 suns	27.0%	2700	270
UNSW	Laser-grooved large arc c-Si module	11 suns	21.7%	2387	217
DuPont	Split-spectrum tandem GaInP/GaAs with GaInAsP/GaInAs submodule	20 suns	38.5%	7700	385
ENTECH	12-cell c-Si module	79 suns	20.5%	16,195	205
Amonix	Back-contact c-Si cell	92 suns	27.6%	25,392	254
Fraunhofer ISE	GaAs single cell	117 suns	29.1%	34,047	257
Spectrolab	Lattice-matched two-terminal triple-junction GaInP/GaInAs/Ge cell	364 suns	41.6%	151,424	416
Solar Junction	Triple-cell two-terminal GaInP/GaAs/ GaInNAs cell	418 suns	43.5%	181,830	435

Note: AM 1.5 spectrum, cell temperature maintained at 25 °C.

Source: Reproduced from [29]

2.2.2 Solar H₂ Production from Water Splitting

Water electrolysis using solar photonic energy, or photoelectrolysis, occurs by applying a certain cell potential to initiate the reaction can be from an external bias applied by an electricity source (PV, wind, etc.) or by direct interaction of photons with semiconductor materials on the electrodes.

Semiconductor Systems: PV-Electrolysis and Photochemical Cells

Figure 2.4 shows the general reactor schematic for electrolysis and photochemical cells. In an electrolyser (Figure 2.4a), current passes between the cell anode and cathode, which are submerged in an electrolyte liquid. Photoelectrochemical electrolyzers are addressed in more detail in section 2.3. Photochemical (or photocatalytic) water splitting cells (Figure 2.4b) use sensitizer molecules or semiconductors in solution with water, which absorb photonic energy and initiate photochemical reactions to produce H₂ and O₂ gases without

any external bias potential supply. A challenge of these types of reactors is the requirement for the additional step of separation of the H_2 and O_2 products.

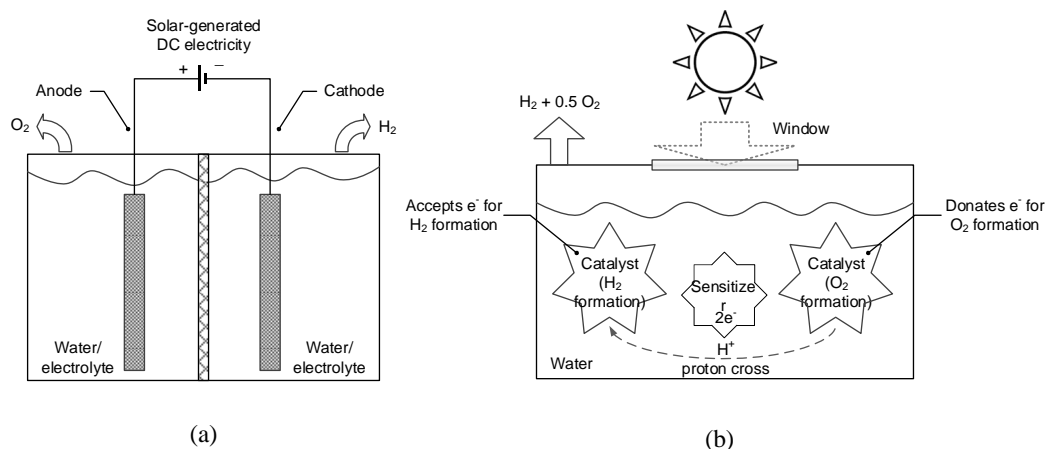


Figure 2.4: (a) Electrolysis and (b) photochemical cells (adapted from [30]).

In a review on the progress of solar energy technologies in Saudi Arabia, [31] identify water electrolysis via PV generated electricity as the most mature method to produce solar- H_2 . The review study by [30] reports a range of 50–80% efficiency for commercial electrolysis processes, and a maximum PV-electrolysis efficiency of less than 16% considering PV efficiencies in the range of 10–20%.

Two mature technologies for water splitting are alkaline and proton exchange membrane (PEM) electrolyzers, shown schematically in Figure 2.5. Alkaline electrolyzers have reliable operation with efficiencies ranging from 47% - 87% [32], and lifetimes up to 15 years [33] [34]. In alkaline cells, electrodes immersed in concentrated KOH electrolyte (25-30 wt% [32]) are separated by a gas-tight diaphragm. Water is reduced at the cathode to produce H_2 , and OH^- anions pass through the diaphragm to recombine at the anode, producing O_2 and releasing electrons.

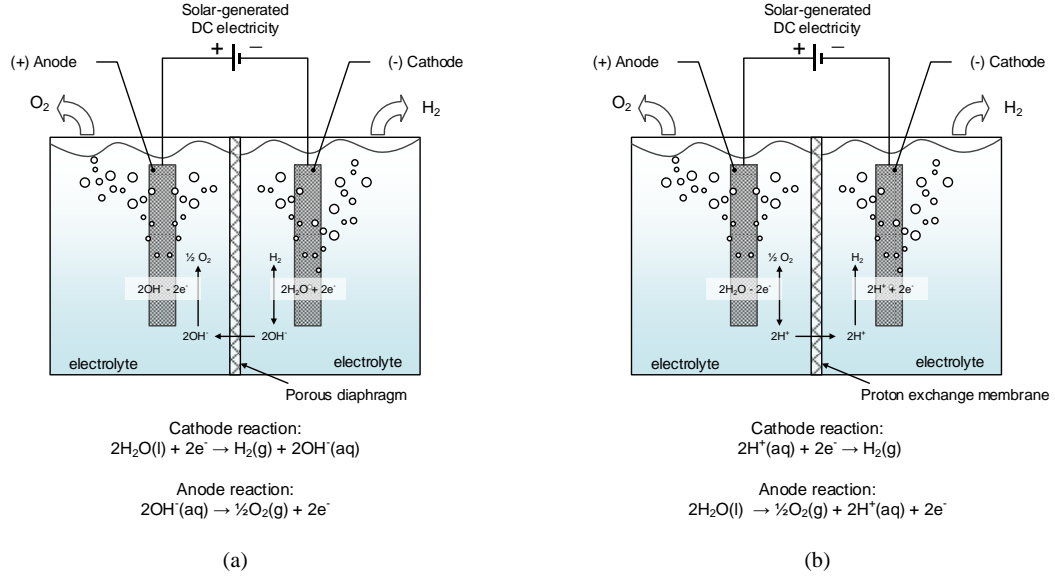


Figure 2.5: Schematic and electrode reactions for (a) alkaline electrolyser and (b) PEM electrolyser cells.

Compared to alkaline cells, PEM electrolysis does not require a corrosive electrolyte and produce high purity gases in a more ecological manner [35]. Furthermore, PEM electrolyzers are able to operate at high current densities up to several amps per square centimetre [36]. In the PEM electrolysis process, water is oxidized at the anode, producing O₂ gas, electrons, and protons. The protons pass through the ion exchange membrane and are reduced on the cathode, closing the circuit and producing H₂ gas. A 2016 study by [37] demonstrates a solar-to-hydrogen conversion efficiency averaging 30% over a 48-hour test period using triple junction PV cells under concentrated simulated light to supply electricity to two series-connected PEM electrolyzers. In the study, the authors note that a key factor for improving efficiency of PV-electrolysis is by matching the maximum power points of the PV cell and the electrolyser. By combining multiple electrolyser units in series, it is possible to match the maximum power points of the PV and electrolyser systems to improve the integrated system performance [37].

2.2.3 Solar H₂ and CO₂ Fuel Production Processes

Various processes utilize solar H₂ and anthropogenic CO₂ for fuel production, either as direct solar applications, or indirectly by using solar electricity to supply power to a fuel production process.

Photobiological H₂ and CO₂ Utilization

Direct applications supply sunlight to photosynthetic organisms to store solar energy as biomass in algae for processing to biofuel using photobioreactors of various configurations, such as those shown in Figure 2.6.

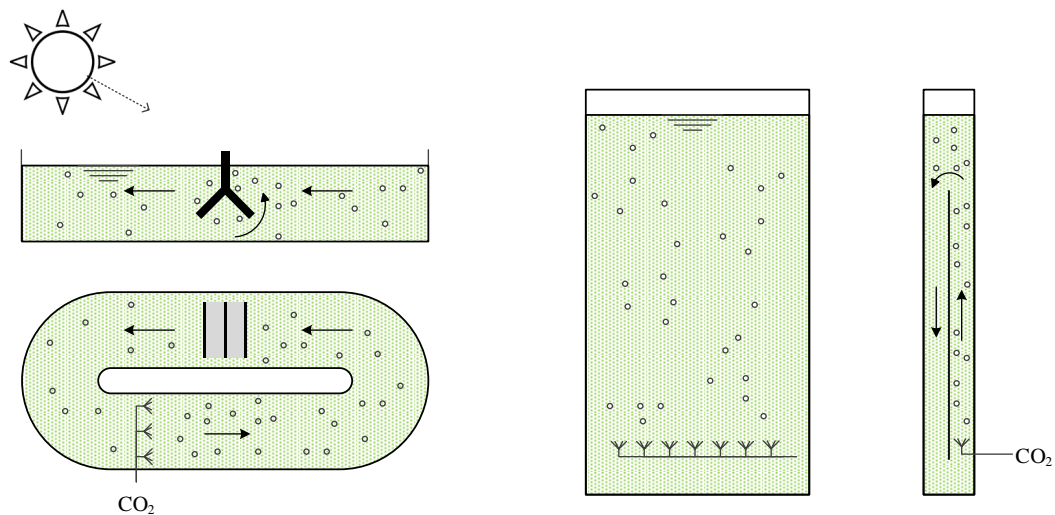


Figure 2.6: Photobiological H₂ and CO₂ conversion by algae for biomass production in raceway pond and flat plate photobioreactors.

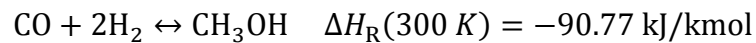
The performance evaluation of these systems uses a Net Energy Ratio (NER), which compares the energy production in the form of biomass or lipids to the energy requirement to operate the bioreactors to generate the organic materials [38]. Photobiological systems can also generate hydrogen and oxygen using green microalgae and cyanobacteria. These systems have an ideal efficiency of 10%, and saturate at low solar irradiance levels (~ 0.03 Suns) [39].

2.2.4 Solar Methanol Production

The use of methanol as a hydrogen storage medium has been regarded as the “most economic way” [11] to reduce GHGs. Methanol is the simplest liquid H₂ carrier, and can be used as a direct fuel, in direct methanol fuel cells, and as an efficient fuel in gas turbines [40]. Figure 2.7 shows solar and renewable resource based methanol synthesis options for syngas and CO₂ hydrogenation options. Although CO₂ is one of the main GHG air pollutants, it is also a potential source for raw carbon [41]. Application as a carbon monoxide (CO) replacement in fuel production processes is gaining significant attention from researcher, especially as the need to reduce anthropogenic CO₂ intensifies.

CO₂ Hydrogenation

Two main reactions occur in the process of reacting CO₂ and H₂, which is referred to as CO₂ hydrogenation: the reverse water gas shift, and the formation of methanol, according to the following two reactions:



The overall reaction for CO₂ hydrogenation occurs according to:



The reverse water gas shift reaction is side reaction, since the main goal is storing the hydrogen in methanol. As presented in the formation of methanol reaction the reaction of one mole of CO₂ with three moles of hydrogen produces -90.70 kJ of thermal energy, meaning that it is an exothermic reaction. However, the reverse of the water gas shift reaction is an endothermic reaction. Based on the ideal thermodynamic analysis, increase

in pressure and decrease of the temperature favour the methanol formation reaction. Considering the nature of CO_2 being a chemically inert gas, increasing the temperature above 513 K enhances the CO_2 activation and in turn activates the methanol formation [41].

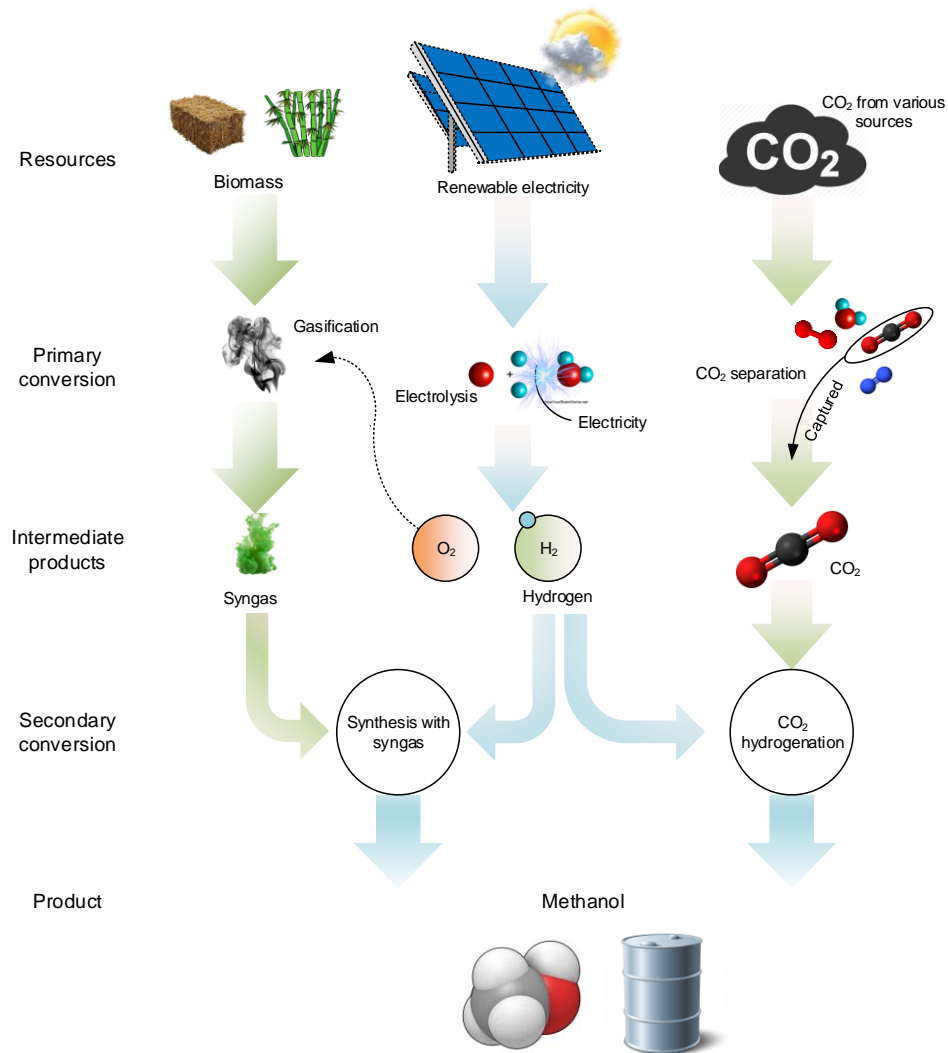


Figure 2.7: Renewable methanol production pathways (adapted from [40])

2.3 Photoelectrochemical Hydrogen Production

Photoelectrochemical (PEC) water-splitting combines solar energy collection and water electrolysis processes in one device. The PEC process occurs when a semiconductor

material immersed in an aqueous electrolyte is exposed to sunlight. Under certain conditions (dependent on the material properties), photon energy converts to electrochemical energy capable of directly splitting water into hydrogen and oxygen, effectively storing solar energy in a stable form as chemical energy [42].

2.3.1 Photoactive Materials

The 1972 study by Fujishima and Honda [43] is widely cited as the first demonstration of PEC water splitting using TiO_2 . Since then, the study of photoactive materials has become an active research area in terms of material properties, characterization and characterization methods, and applications for water splitting and other photoelectrochemical reactions.

For reliable photoelectrochemical decomposition of water to occur, the ideal semiconductor system must meet certain criteria [42]:

- generate sufficient voltage for water splitting upon irradiation,
- have a sufficiently narrow band gap to absorb a large portion of the solar spectrum,
- conduction and valence band edge potentials should straddle the hydrogen and oxygen redox potential levels,
- system components must have long term corrosion resistance in aqueous electrolyte conditions,
- charge transfer from the semiconductor surface to the electrolyte solution must minimize kinetic overpotential losses, and be selective for the hydrogen evolution reaction and oxygen evolution reaction.

The band gap values of several semiconductor materials are shown in Figure 2.8, and the associated band edges are shown in Figure 2.9.

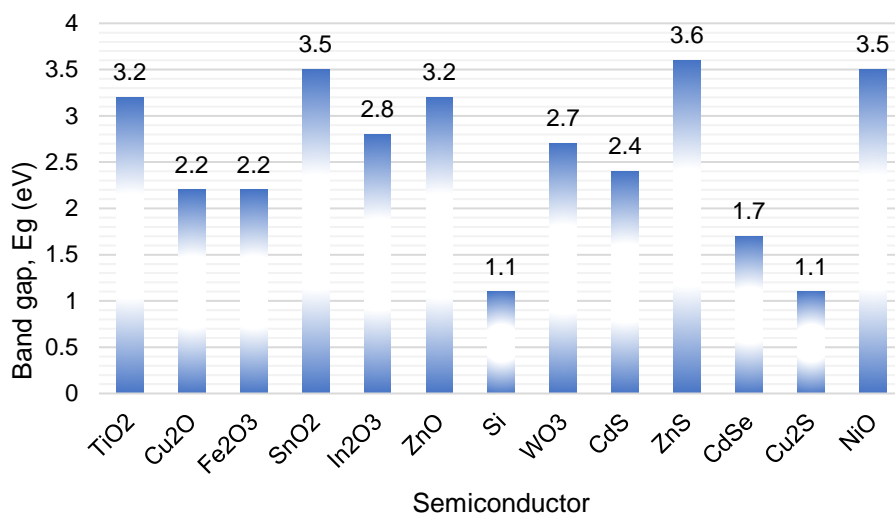


Figure 2.8: Bandgap of various semiconductors for PEC water splitting applications (data from [44] [45] [46] [47])

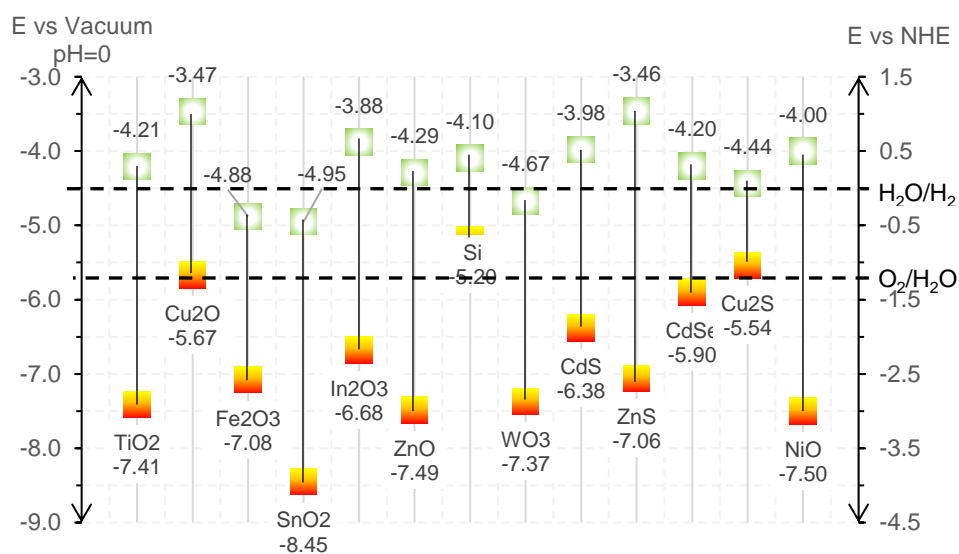


Figure 2.9: Band edges (conduction lower and valence top) for various semiconductor materials (data from [44] [45] [46] [47])

2.4 Main Gaps in the Literature

Throughout the literature review, there are a great number of in-depth studies and reviews of photoactive semiconductor materials, and lab-scale prototypes for characterization of photo-response, and methods to apply (adhere) these to various substrates. However, very

few studies include fully integrated systems utilizing PEC technology. Investigation of a novel hybrid configuration of a PEC cell in [48] models solar spectrum splitting to generate PV electricity and H_2 simultaneously. The cell also utilizes photoactive electrode material to produce H_2 in a photocatalytic reaction. By storing electricity generated during daylight hours, the cell is able to generate hydrogen continuously via the chlor-alkali electrochemical reaction process, which also produces NaOH as a useful by-product. The authors report maximum multigeneration efficiency of 42% when operating in the temperature range from 40–50°C.

In a review on the status of PEC device integration by [49], the authors suggest that the limited number of studies focusing on complete PEC devices (rather than individual component performance and characterization), and system integration in experimental prototypes as a reason for the ‘less-advanced, smaller-scale, and less-stable status’ of PEC technology in comparison to other water splitting reactors. This study aims to address this gap with the experimental investigation of an integrated CPV-PEC H_2 reactor. Performance assessment will consider that of the individual components (concentrator, spectrum-splitting mirror, electrolyser and PEC reactor, and PV module), and of the integrated device in simulated and actual environmental conditions.

CHAPTER 3: EXPERIMENTAL APPARATUS AND PROCEDURES FOR CPV-PEC H₂ PRODUCTION

The CPV-PEC apparatus, built at the Clean Energy Research Laboratory in UOIT and shown in Figure 3.1, consists of a novel PEC reactor, solar concentrating Fresnel lens, spectrum-splitting dielectric mirror array, and PV module. This chapter describes the components, devices, and procedures for the CPV-PEC system.



Figure 3.1: CPV-PEC H₂ reactor and solar splitting apparatus outside of CERL Solarium.

3.1 Experimental System Description

Figure 3.2 shows the general arrangement of the system components with light splitting. The operating principle is such that the direct-normal portion of solar insolation incident to the surface of the concentrating Fresnel lens focuses onto the surface of the dielectric mirror array, which is set at a distance such that the focal area is approximately the same as the array. The mirror reflects wavelengths from 425 nm – 675 nm onto the photocathode of the PEC reactor and transmits wavelengths ranging from 800 nm – 1200 nm onto a PV panel. The PV panel is connected to the PEM electrolyser component of the PEC reactor as a load. In this arrangement, a single light source supplies energy to PEM electrolysis and photoelectrochemical H_2 production processes simultaneously.

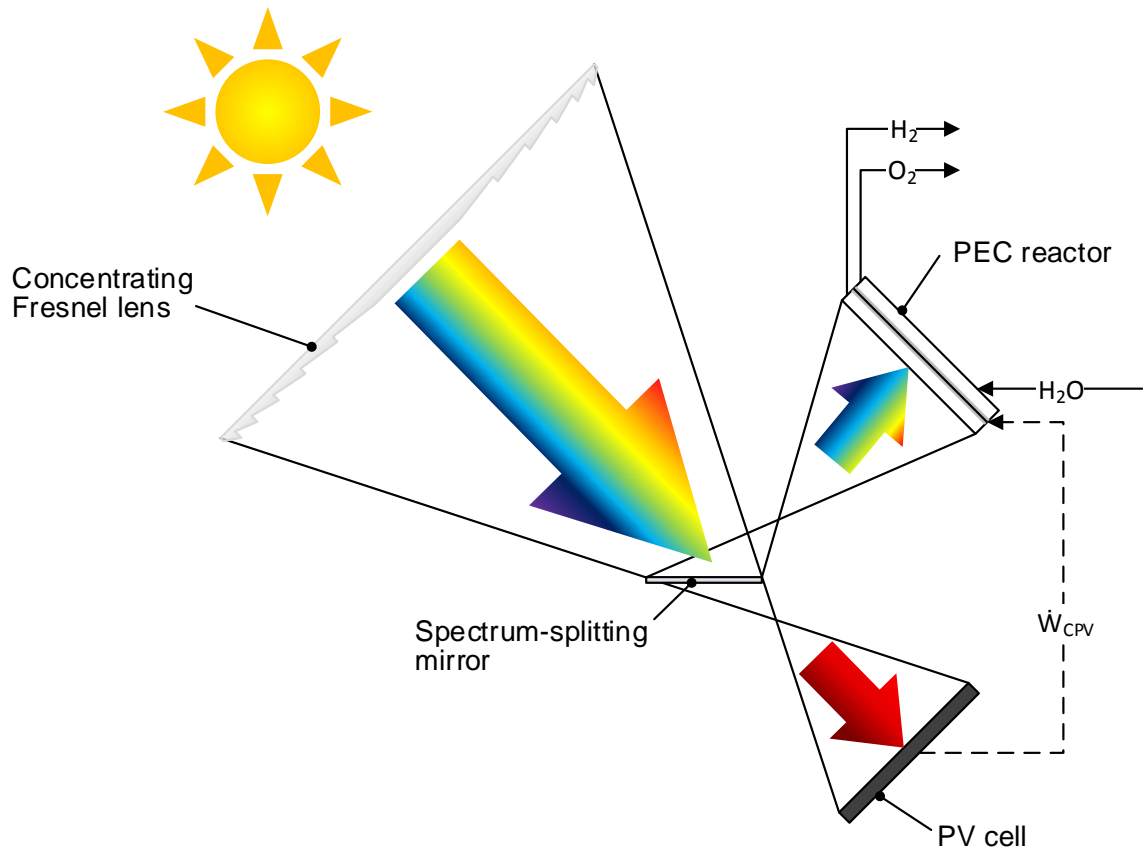


Figure 3.2: Arrangement of main CPV-PEC components.

3.2 Experimental Equipment

3.2.1 PEC Reactor

The main component of the experimental system is the novel PEC reactor unit, which is capable of generating H_2 by PEM electrolysis and photoelectrochemical reaction via direct interaction with photonic energy on the surface of a large-area copper oxide (Cu_2O) coated photocathode (820 cm^2), shown in Figure 3.3.

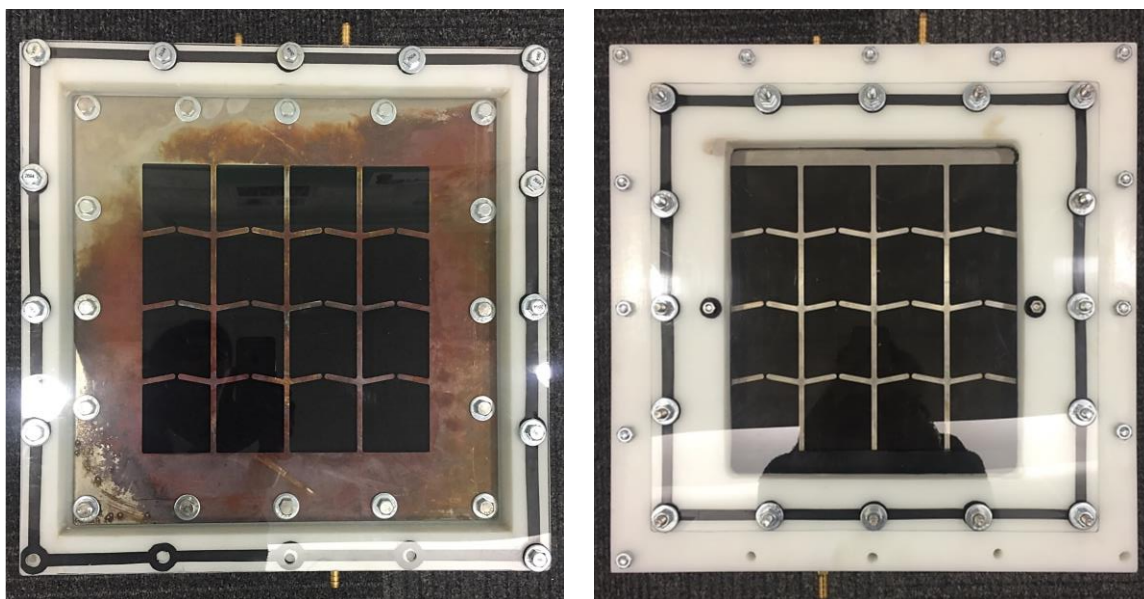


Figure 3.3: Assembled PEC reactor photocathode (left) and anode (right) compartments.

The membrane electrode assembly of the electrolyser comprises custom design cathode and anode plates, and a large area ($\sim 930\text{ cm}^2$) Nafion 115 proton exchange membrane (PEM) purchased from Fuel Cells Etc. [50]. The properties of the PEM are listed in Table 3.1. The electrodes are laser cut from 3 mm thick stainless steel in a custom skeletal-type design to provide support for the large area of the proton exchange membrane and prevent damage or shifting due to pressure differential in the anode and cathode compartments. The electrode design also acts to direct flow of H_2 and O_2 bubbles produced

on the active membrane and electrode surfaces upward through channel openings to outflow ports for collection.

Table 3.1: Proton exchange membrane specifications.

Membrane Dimensions	30.5 cm x 30.5 cm
Membrane Material	Nafion 115
Membrane Thickness	127 μm
Active Area	930 cm^2
Anode Catalyst Loading	IrRuOx (3 mg/cm^2)
Cathode Catalyst Loading	PtBlack (3 mg/cm^2)
Water Content (23 °C, 50% rel. humidity)	5 %
Water Uptake	38%
Thickness Change (23 °C, 50% rel. humidity to water soaked at 23 °C,)	10%
Thickness Change (23 °C, 50% rel. humidity to water soaked at 100 °C,)	14%
Conductivity	0.1 $\Omega^{-1}\text{cm}^{-1}$

Source: [51]

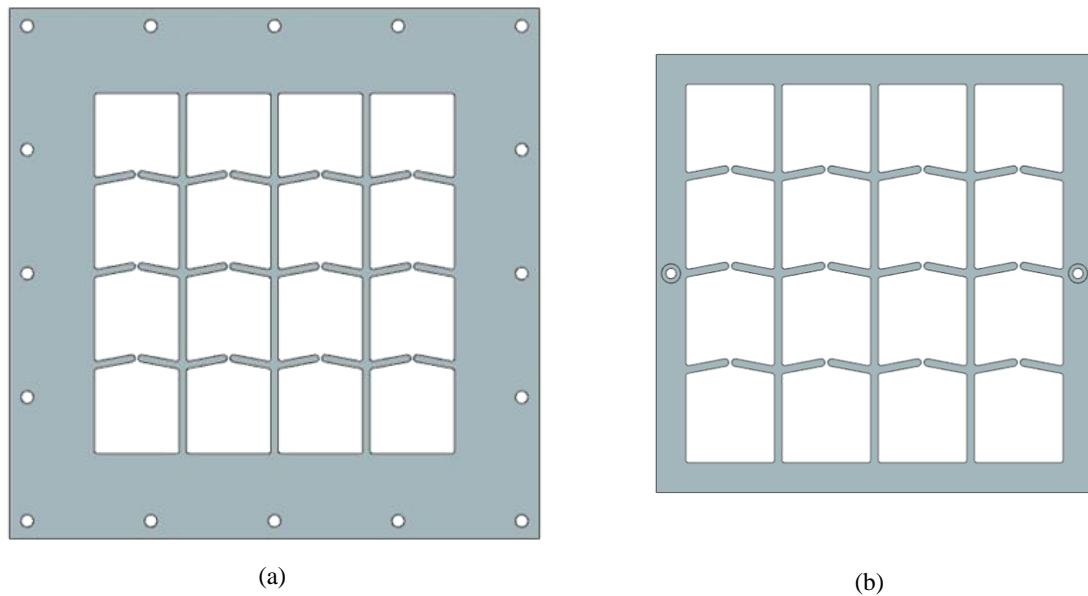


Figure 3.4: Custom profile design of stainless steel plates for PEC reactor, (a) cathode, and (b) anode.

The general arrangement of the PEC reactor and a section view of the MEA is shown in Figure 3.5. The MEA is housed by a rigid high density polyethylene (HDPE) frame with acrylic front and back window panels to allow illumination of the photocathode. Nitrile rubber gaskets provide sealing between each layer. Inlet ports at the base of each compartment supply water to the reactor, and outlet ports at the top of the reactor collect the water gas mixture for collection and separation.

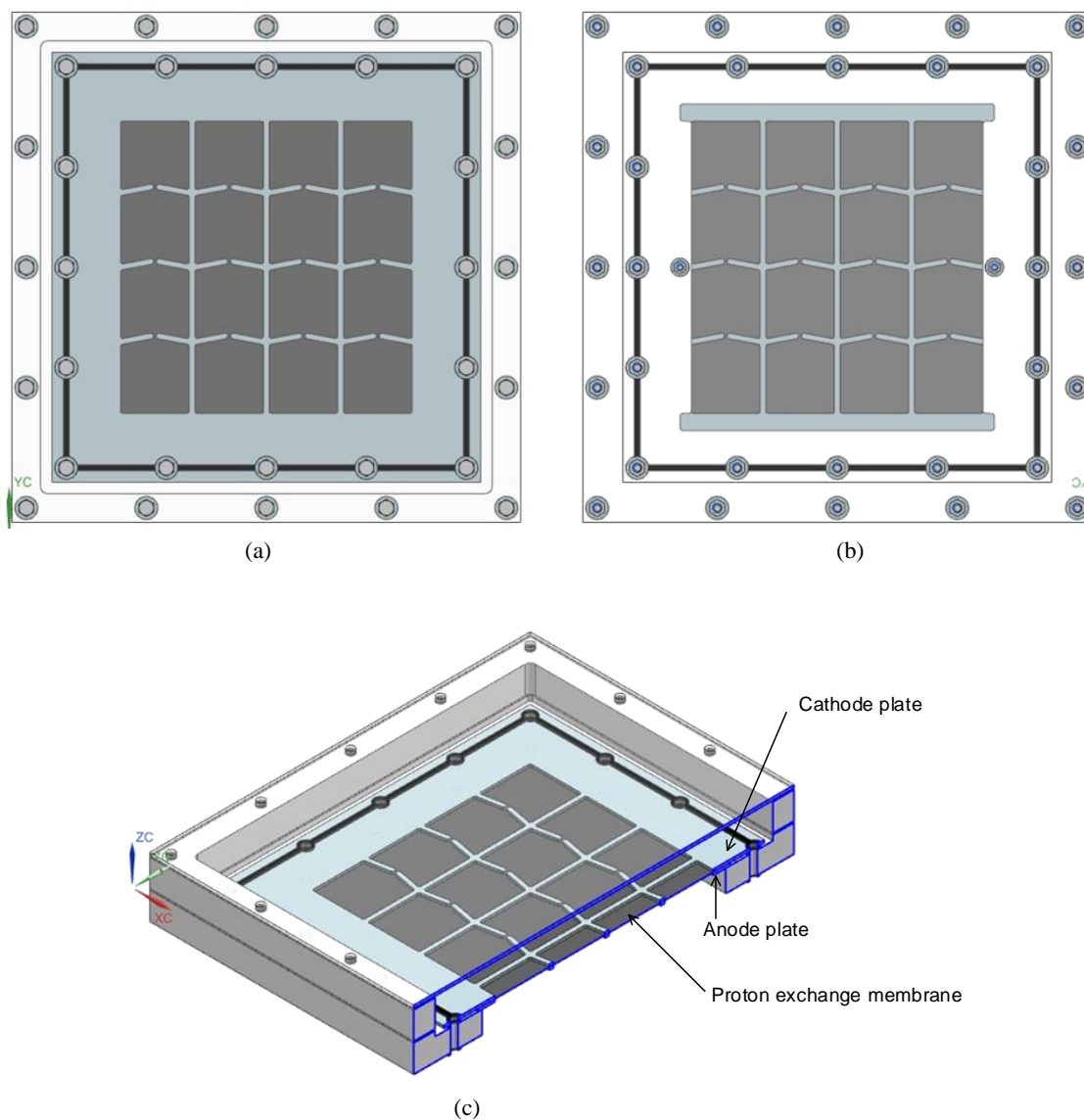


Figure 3.5: CAD model of PEC reactor (a) cathode compartment, (b) anode compartment, (c) membrane electrode assembly.

3.2.2 Concentrating Lens and Dielectric Mirror

The concentrating Fresnel lens is salvaged from a Sony rear projection television set. The lens has an aperture area of 0.86 m^2 , and overall dimensions of $1.06 \text{ m} \times 0.81 \text{ m}$ (42 in \times 32 in nominally). The lens concentrates sunlight onto a spectrum splitting mirror array that reflects a portion of the concentrated light onto the photocathode of the PEC reactor, and transmits the remaining concentrated light onto the PV panel.

The mirror array, shown in Figure 3.7, is made up of 6 dielectric cold mirrors made of borosilicate glass sandwiched between acrylic sheets, and secured around the edges by an aluminum channel frame. The mirror has a dielectric coating that reflects wavelengths from $425 \text{ nm} - 675 \text{ nm}$ and transmits wavelengths ranging from $800 \text{ nm} - 1200 \text{ nm}$. The mirror properties are listed in Table 3.2.



(a)



(b)

Figure 3.6: (a) Concentrating Fresnel lens, and (b) mounting arrangement of the dielectric mirror, PEC, and PV components in the CPV-PEC experimental setup.



Figure 3.7: Dielectric mirror array.

Table 3.2: Spectrum splitting dielectric mirror specifications.

Parameter	Value
Dimensions	101.6 mm x 127.0 mm
Array Dimensions	300 mm x 250 mm
Thickness (mm)	3.3
Angle of Incidence (°)	45
Coating Type	Dielectric
Coating Reflectance Specification	$R_{avg} > 90\%$ @ 425 - 675nm
Coating Transmittance Specification	$T_{avg} > 85\%$ @ 800 - 1200nm
Wavelength Range (nm)	425 - 1200
Type	Cold Mirror

Source: [52]

3.2.3 Photovoltaic (PV) Module

Solar electricity generation for the CPV-PEC uses a 6-Watt single junction Si solar module with 36 cells, manufactured by SunWize [53]. The module is shown in Figure 3.8, and characteristic details are listed in Table 3.3. The module rating is for non-concentrated sunlight, and experimental testing is carried out for concentrated sunlight conditions to

determine I-V characteristics, power output, operating temperature, and efficiency within the integrated system.



Figure 3.8: Sunwise 6 W PV Module.

Table 3.3: Characteristics of the SC6-18V Solar PV module.

Parameter	Value
Semiconductor material	Si
Temperature range	-20 °C – 90 °C
Module dimensions	24 cm x 24 cm
Number of cells in series	36
Open circuit voltage, V_{oc}	22.4 V
Short circuit current, I_{sc}	0.33 A
Max. Power, P_{mp}	6 W
Max. power voltage, V_{mp}	18.7 V
Max. power current, I_{mp}	0.3 A
Fill factor, FF	0.76

Source: [53]

3.3 Experimental Devices and Procedures

3.3.1 Gamry Reference 3000 Potentiostat with 30 K booster

The Gamry Reference 3000 Potentiostat, shown in Figure 3.9, is used to apply voltage to electrode pairs and record current measurements. The device is used in both potentiostatic and galvanostatic modes to record potential and current data for various electrochemical experiments and PV module testing.



Figure 3.9: Gamry Reference 3000 (a) Potentiostat, (b) 30K Booster (images adapted from [54]).

3.3.1 Solar Simulator

Indoor testing of the dielectric mirror, PV module, and photocathode under simulated sunlight conditions utilises the OAI TrisoI™ Solar Simulator [55], shown in Figure 3.10. The simulator has an illuminated area of 208 mm x 208 mm that delivers collimated rays, with spectral match from 400 nm – 1100 nm in 100 nm increases. Light filters imitate Air Mass 1.5 Global (AM 1.5G), and is capable of tuning ray concentration from 0.6 Suns - 1.2 Suns. During testing, the simulated sunlight was set at 1000 W/m² to act as a consistent baseline for characterization of the components prior to outdoor testing under variable conditions.

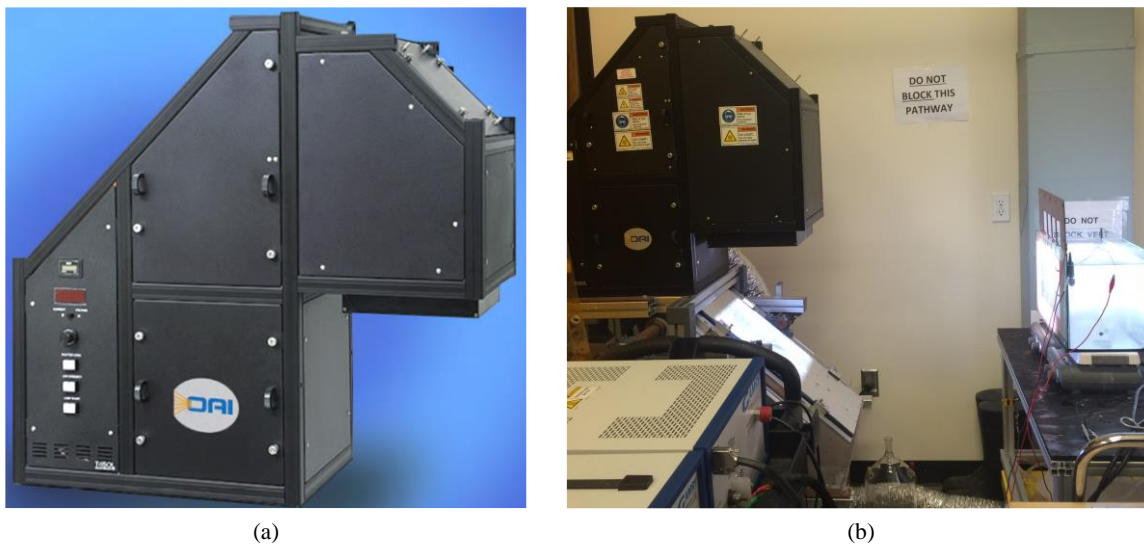


Figure 3.10: (a) TriSol Class AAA Solar Simulator [55], (b) solar simulator in experimental setup for photocathode characterization in simulated light.

Solar spectrum and wavelength measurements are recorded using the Ocean Optics Red Tide USB 650 spectrometer and Spectrasuite software [56]. The device is capable of measuring wavelengths of 350 nm – 1000 nm through a UV-VIS fiber cable (core dia. 400 μm). Temperature and irradiance measurements are recorded using Vernier Technology temperature sensor [57] and pyranometer devices [58]. The device ranges and accuracy details are listed in Table 3.4.

3.3.3 Experimental Procedures

Photocathode Preparation via Cu_2O Electrodeposition

Electrodeposition is used to fix the photoactive semiconductor material Cu_2O , a p-type semiconductor material with an energy band-gap range of 1.9 – 2.2 eV [47] [59] [60], onto the 820 cm^2 surface area of the stainless steel cathode. The deposition process is carried out using a 3-electrode setup, with the deposition substrate as the working electrode (WE, green wire), a counter electrode (CE, red wire), and reference electrode (RE, black wire) –

in this case, an Ag/AgCl electrode. Applied potential is controlled using the Gamry Ref. 3000 Potentiostat with 30 K booster. The substrate is submerged in an electrolyte solution containing $\text{CuSO}_4 \cdot 5\text{H}_2\text{O}$, and lactic acid to produce a copper lactate complex of 0.4 M $\text{CuSO}_4 \cdot 5\text{H}_2\text{O}$ and 3 M lactic acid. The electrodeposition process for coating the stainless steel cathode plate is controlled at an applied voltage of -0.3 V vs. Ag/AgCl RE, and a graphite rod with a platinum wire coil CE. The electrolyte solution of 151.9 g $\text{CuSO}_4 \cdot 5\text{H}_2\text{O}$, 340 mL lactic acid produces a copper lactate complex of 0.4 M $\text{CuSO}_4 \cdot 5\text{H}_2\text{O}$ and 3 M lactic acid. In the mixture, copper is stabilized by complexing with the lactate ion, and approximately 150 g NaOH added to electrolyte to maintain the solution pH at alkaline condition (pH meter: 9.97). The resulting electrolyte is a deep blue solution (seen in Figure 3.11), in which the cathode is fully submerged for the deposition process.

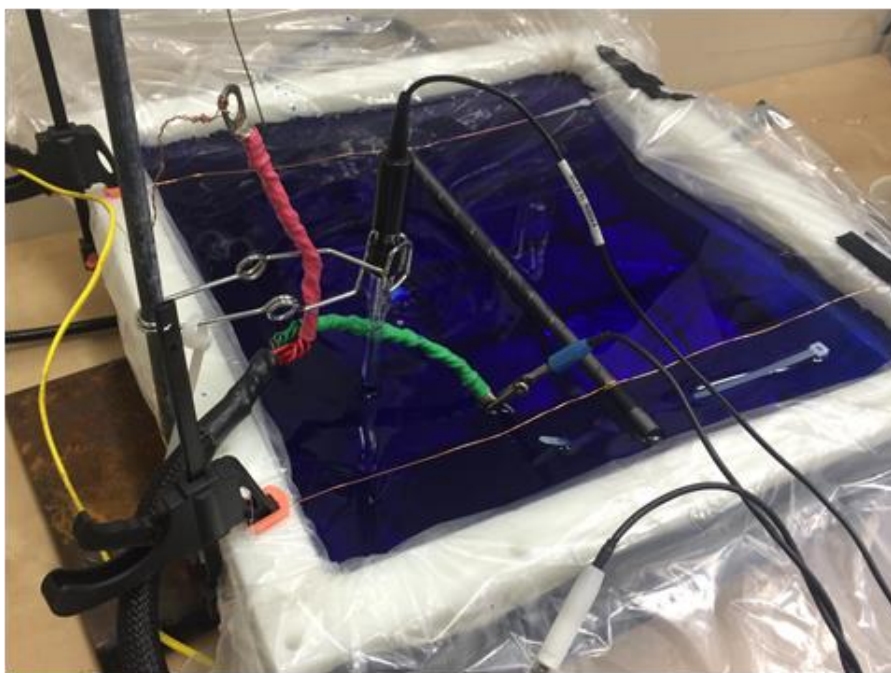


Figure 3.11: Electrodeposition of Cu_2O film on stainless steel cathode plate.

A magnetic stirrer continuously mixes the electrolyte solution during the preparation and electrodeposition process. The solution temperature is maintained at a

temperature of 55.5 °C using temperature controller, and full coating is achieved after four 20-minute intervals in the electrolyte solution, as seen in Figure 3.12.

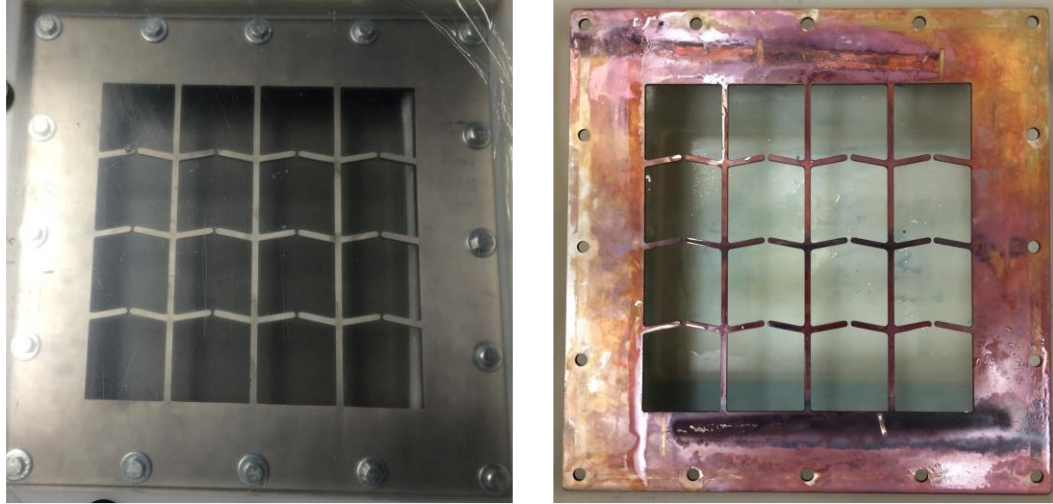


Figure 3.12: Stainless steel cathode plate before (left) and after (right) Cu_2O electrodeposition process.

3.4 Experimental Error and Measurement Uncertainties

Experimental results are subject to the accuracy of measurement devices, as well as bias and precision errors. These effects are quantified in experimental uncertainty, defined by the equation:

$$\sigma_i = \sqrt{(B_i^2 + P_i^2)} \quad (3.1)$$

where B_i and P_i represent the bias and precision error values for a result i [61]. The value of the bias error represents the interval about within which the true value lies [62]. Precision errors represent limitation of the repeatability of a measurement device and are estimated statistically.

The propagation of experimental error in calculations is outlined according to the methods in [61]. Propagation of error in experimental results can be approximated for a function U of one measurement with an associated uncertainty with the following:

$$\sigma_U \approx \left| \frac{dU}{dX} \right| \sigma_x \quad (3.2)$$

For several measurements (X_1, X_2, \dots, X_n) with individual uncertainties, where $U=U(X_1, X_2, \dots, X_n)$, the relative uncertainty becomes:

$$\frac{\sigma_U}{U} \approx \sqrt{\left(\frac{\partial U}{\partial X_1} \right)^2 \sigma_{X_1}^2 + \left(\frac{\partial U}{\partial X_2} \right)^2 \sigma_{X_2}^2 + \dots + \left(\frac{\partial U}{\partial X_n} \right)^2 \sigma_{X_n}^2} \quad (3.3)$$

For approximation of the uncertainty of a function $U=U(X_1^{m_1}, \dots, X_n^{m_n})$, the equation is given by:

$$\frac{\sigma_U}{U} \approx \sqrt{m_1 \left(\frac{\sigma_{X_1}}{X_1} \right)^2 + \dots + m_n \left(\frac{\sigma_{X_n}}{X_n} \right)^2} \quad (3.4)$$

The measurement range and instrumental accuracies of the devices used in the experiments are given in Table 3.4. These are applied to the experimental measurements to determine the absolute uncertainty of the results given in Chapter 6.

Table 3.4: Measurement device accuracy and range.

Variable	Device	Range	Device Accuracy	Applied Accuracy	Measured Accuracy
Potential	Gamry Reference 3000 Potentiostat	± 15 V	± 0.003 V	± 1 mV \pm 0.2% of setting	± 1 mV \pm 0.2% of reading
Current	Gamry Reference 3000 Potentiostat	± 3 A	± 0.007 A	± 5 pA \pm 0.05% of range	$\pm 0.2\%$ of value (3 A -3 nA)
Irradiance	Trisol Solar Simulator TSS-208	600 – 1200 W/m ²	± 20.28 W/m ²	-	-
Spectrum	Ocean Optics Spectrometer	350 -1000 nm	< 0.5%		
Irradiance	Vernier Pyranometer-	0 – 2200 W/m ²	$\pm 5\%$	-	-
Temperature	Vernier Temperature Sensor	-25 – 125 °C	± 0.5 °C		

Source: [54] [55] [56] [57] [58]

CHAPTER 4: INTEGRATED SYSTEMS FOR SOLAR METHANOL FUEL SYNTHESIS

Developing systems that produce fuels that can directly substitute for high-demand liquid fossil fuel derivatives can significantly reduce non-renewable energy dependence at the consumer level. This chapter describes two integrated systems for solar-based methanol synthesis. System I integrates CPV-PEC H_2 production based on the experimental system developed in this study with CO_2 and freshwater supply from seawater. The CO_2 extraction uses a bipolar membrane electrodialysis reactor, and fresh water production uses a reverse osmosis desalination process. Methanol synthesis is carried out in a CO_2 hydrogenation reactor in a small-scale synthesis plant. As a comparison case study, System II utilizes a combined H_2 - CO_2 extraction process from seawater to supply the material streams for the same methanol process. Concentrating linear reflectors illuminate CPV modules ($\eta_{CPV} = 30\%$) at a concentration ratio, C , of 10 suns, which supply electricity input for subsystem processes in both System I and System II.

4.1 Integrated System I: CPV-PEC Based Methanol Synthesis

The solar methanol plant in System I integrates the experimental CPV-PEC with a CO_2 hydrogenation reactor for methanol synthesis, seawater reverse osmosis (SWRO) desalination unit, and a bipolar membrane electrodialysis unit for CO_2 capture from seawater. The arrangement of the subsystems is shown in Figure 4.1 to indicate the general integration of these processes

Seawater is drawn into the system, where a portion is sent to the BPMED unit and the rest to the SWRO to produce desalinated water for the PEC reactor. H_2 produced by the CPV-PEC, and CO_2 extracted from seawater supply the methanol synthesis reactor, producing fuel and water at the outlet. The product water is recirculated to the PEC reactor to reduce energy demand for the SWRO desalination process.

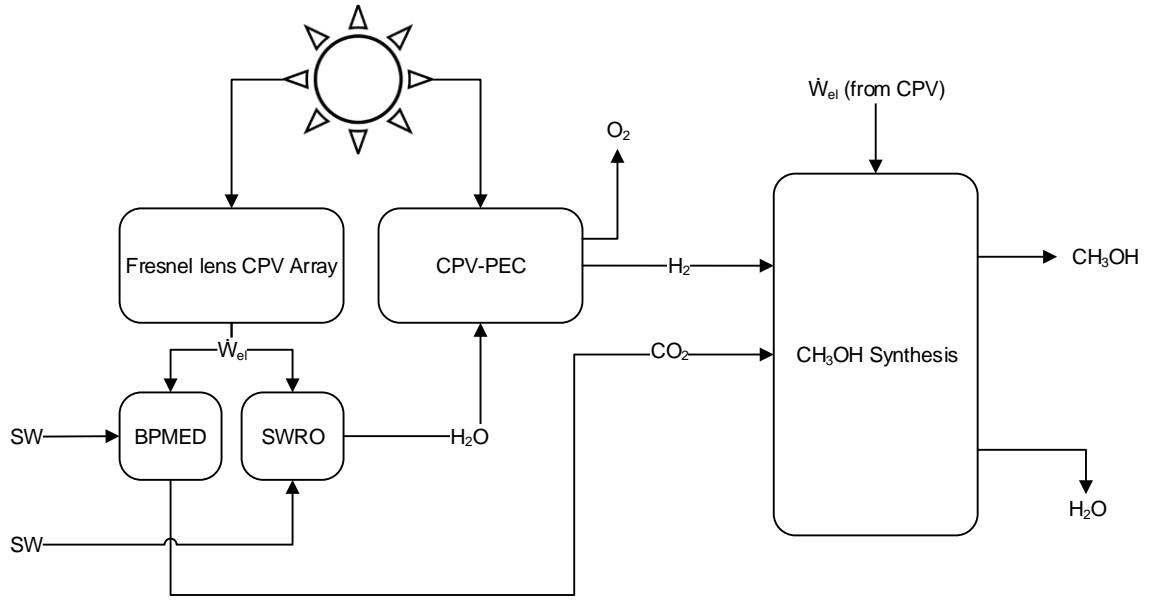


Figure 4.1: System I processes, power, and material flows.

4.1.1 Methanol Synthesis via CO₂ Hydrogenation

CO₂ hydrogenation takes place in a four-stage cascade adiabatic reactor, shown schematically in Figure 4.2, under equilibrium assumptions. The reaction occurs over Cu/ZnO/Al₂O₃ catalyst at a temperature of 493 K, and pressure of 5 MPa, with stoichiometric H₂:CO₂ molar feed ratio of 3:1. The temperature at the inlet to each reactor stage is 493 K, with intercooling after each to remove heat released by the exothermic reaction. H₂ and CO₂ gases undergo compression in the feed compressor in three stages; P_0 to 0.4 MPa, 0.4 to 1.2 MPa, and 1.2 to 3 MPa, with intercooling between stages. The fresh feed gases mix with recycle gases in the mixing chamber, and are compressed to 5 MPa, then heated to 493 K for entering the reactor. The partially reacted gas mixture at the outlet of the reactor is flash-separated and cooled, allowing the methanol and water products to be collected, and the unreacted gases are compressed from 1.2 to 3 MPa to mix with fresh feed gas in a continuous process. The recycle ratio is given as 4.2 for this plant. Heat release by the exothermic reaction is recovered to provide thermal energy to initiate the reactions, and to minimize losses.

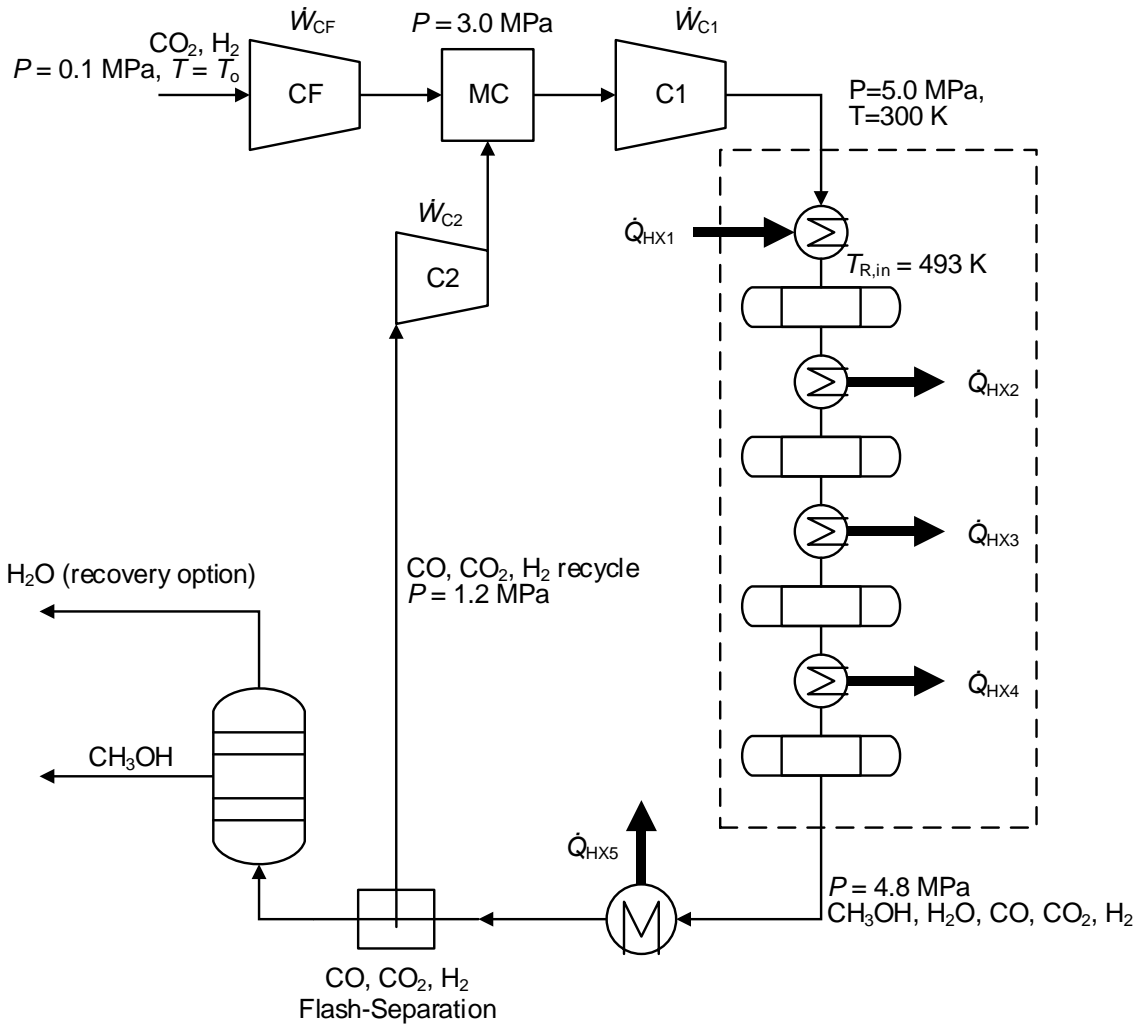


Figure 4.2: Methanol synthesis plant (adapted from [63]).

4.1.2 H₂O Production via Seawater Reverse Osmosis

Reverse osmosis (RO) produces desalinated water for hydrogen production. A typical seawater reverse osmosis (SWRO) plant is shown in Figure 4.3, indicating the major stages and components for the process, and typical operating characteristics are given in Table 4.1. At the intake, a low pressure pump (LPP) with a pressure ratio of 6.5 draws seawater into the system and directs the outlet flow through a filter to remove particulate matter. After physical filtration, the seawater undergoes chemical pre-treatment. Treated seawater is drawn into the reverse osmosis unit by a high pressure pump (HPP), increasing the

pressure to the operating pressure of the RO system; in this case, 6 MPa [64]. A throttling valve extracts a small portion of untreated seawater through a system bypass to mix with the permeate water stream, controlling the final salinity conditions of the product water. Permeate water leaves the RO module at 180 kPa for post-treatment; mixing with the bypass stream at the RO back-pressure to achieve salinity level requirements. Brine leaves the RO module at 5.1 MPa, where an energy recovery turbine (ERT) produces work from the flow energy of the waste stream.

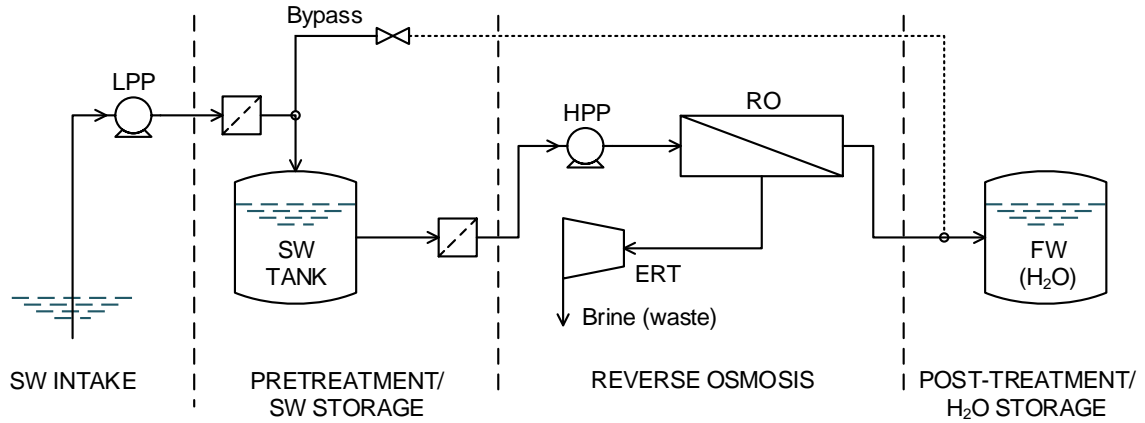


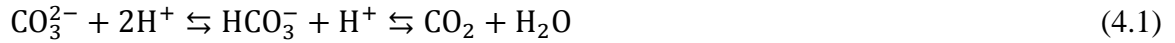
Figure 4.3: SWRO desalination plant (adapted from [64]).

Table 4.1: SWRO desalination plant operating characteristics.

Seawater density, ρ_{sw} (kg/m ³)	1,027
Seawater salinity (ppm)	35,000
Product water salinity (ppm)	450
Recovery ratio, rr	0.35
High pressure pump efficiency, η_{HPP}	90%
Low pressure pump efficiency, η_{LPP}	87%
Energy recovery turbine efficiency, η_{ERT}	79%

4.1.3 CO₂ Capture via Bipolar Membrane Electrodialysis (BPMED)

The process for CO₂ capture is via bipolar membrane electrodialysis (BPMED). In the reactor developed by [65], shown schematically in Figure 4.4, H⁺ and OH⁻ produced on opposite sides of the bipolar membranes (BPMs) acidify and basify seawater streams entering the BPMED compartments. In the acidic compartments, dissolved inorganic carbon (DIC) is converted to dissolved CO₂ according to the reaction:



The CO₂ is collected via vacuum stripping. As indicated in the diagram, the flow of OH⁻ ions into the basic solution drives transport anions from the basic solution to the acidic solution, carrying a large fraction of the current across the anion exchange membrane (AEM). In an experimental prototype, 59% of DIC from seawater is extracted as CO₂ gas, consuming 242 kJ/mol-CO₂ for seawater entering at a flowrate of 3.1 lpm at pH 5, and 68% extraction of CO₂ gas consuming 285 kJ/mol-CO₂ for seawater entering at a flowrate 6.0 lpm at pH 3.7 [65]. The acidic and basic solutions are then mixed together, returning to a neutral condition, and restored to the ocean.

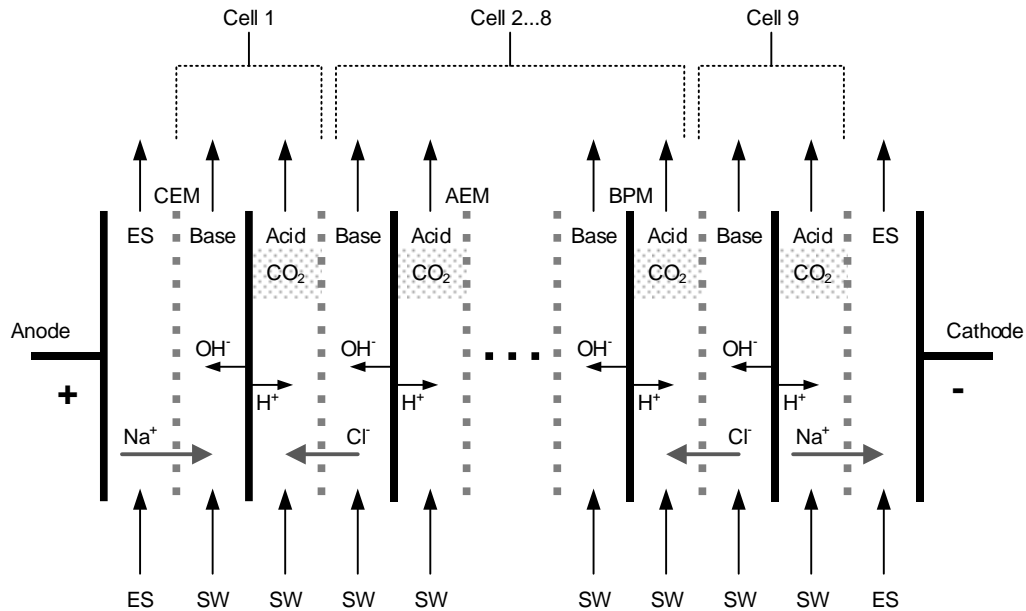


Figure 4.4: Schematic of BPMED unit for CO₂ from seawater (adapted from [65]).

4.2 Integrated System II: Solar Methanol Synthesis via E-CEM H₂ and CO₂

The solar methanol plant in System II comprises a CPV array, CO₂ hydrogenation reactor for methanol synthesis, seawater reverse osmosis (SWRO) desalination unit, and an electrolytic-cation exchange membrane (E-CEM) reactor and separator unit for CO₂/H₂ extraction, and methanol synthesis unit. The arrangement of the subsystems is shown in Figure 4.5 to indicate the general integration of these processes. Seawater is drawn into the system, where a portion is sent directly to the E-CEM reactor and the rest to the SWRO to produce desalinated water for the E-CEM electrolyte supply. H₂ and CO₂ supply the methanol synthesis reactor, producing fuel and water at the outlet.

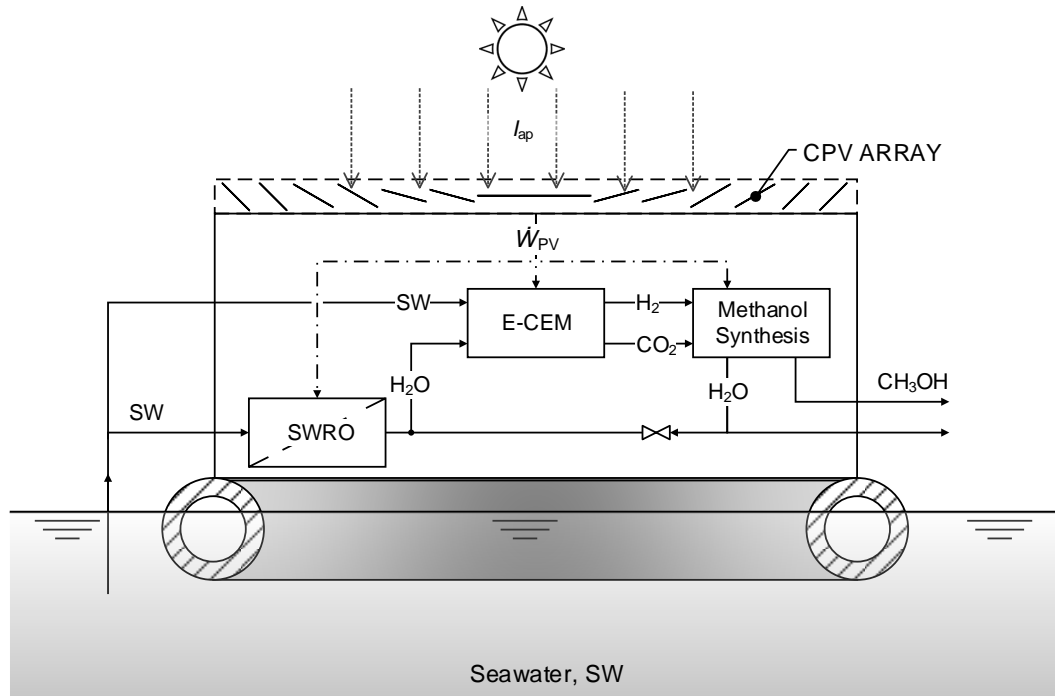


Figure 4.5: System II processes, power, and material flows.

4.2.1 H₂ and CO₂ Capture from Seawater via E-CEM Reactor

Simultaneous extraction of CO₂ and H₂ from seawater and desalinated water takes place through a three-chamber electrolytic cation exchange membrane (E-CEM) reactor

developed by [66], shown schematically in Figure 4.6, which consumes 49 kWh/m³-H₂ (STP). Application of direct current to the cell produces H⁺ and O₂ gas at the anode through electrolysis of water. The H⁺ ions pass through the cation membrane into the centre compartment where they replace Na⁺ in seawater, acidifying the solution and producing CO₂ gas. The Na⁺ ions pass through the cathode-side cation membrane where they react with the catholyte (H₂O) to produce H₂ and NaOH gases. At the electrode compartment outlets, H₂ and CO₂ gases undergo vacuum stripping, and the acidic solution at outlet of the centre compartment mixes with the basic solution at the outlet of the cathode compartment to neutralize effluent seawater.

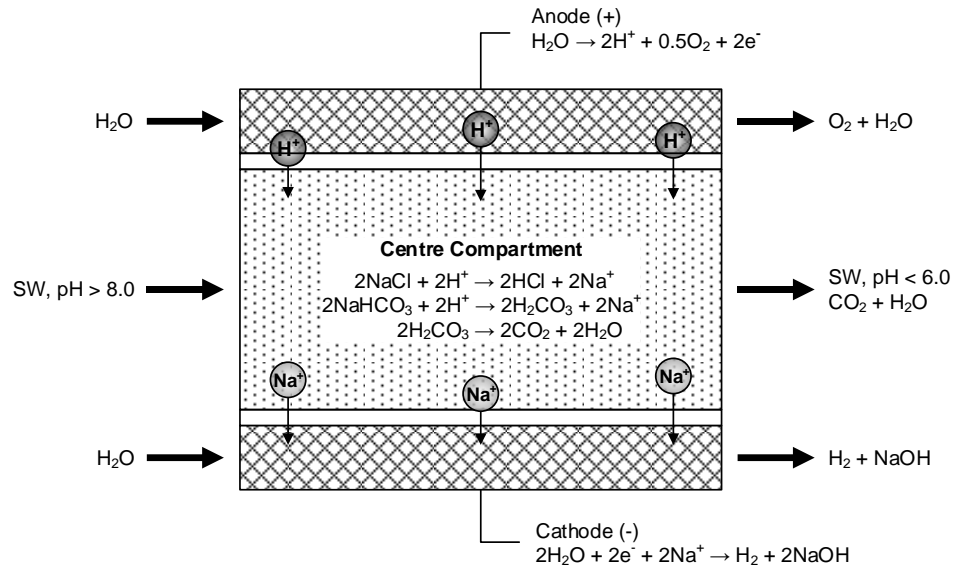


Figure 4.6: Electrolytic cation exchange membrane (adapted from [66]).

CHAPTER 5: ANALYSIS AND MODELING

5.1 Introduction

Assessment of the thermodynamic performance, sustainability, and feasibility of the multigeneration systems requires comprehensive energy, exergy, economic, and environmental analyses to provide a realistic evaluation. This chapter outlines the general assumptions, thermodynamic concepts, exergoeconomic and exergoenvironmental calculations that frame the system models. The following general assumptions apply for the baseline operating case:

- Reference temperature (T_o) and pressure (P_o) are 298 K (25°C) and 100 kPa, respectively.
- Processes occur at steady state.
- Potential and kinetic energies are negligible.
- Chemical reactions proceed to completion.
- All gas and gas mixtures are ideal

5.2 Thermodynamic Analyses

The general definitions for mass, energy, exergy, and entropy balances, thermophysical properties, and system/process efficiencies are given in this section.

From the first law of thermodynamics, the conservation of mass and energy define the mass balance equation (MBE) and energy balance equation (EBE) by:

$$\sum \dot{m}_{in} = \sum \dot{m}_{out} \quad (5.1)$$

$$\sum \dot{E}_{in} = \sum \dot{E}_{out} \quad (5.2)$$

The general energy balance of a device or system with material streams is given by

$$\Delta \dot{E} = \dot{Q} - \dot{W} + \sum(\dot{m}_i h_i)_{in} - \sum(\dot{m}_i h_i)_{out} \quad (5.3)$$

where $\Delta \dot{E} = 0$ under the assumption of steady state conditions. The terms \dot{Q} and \dot{W} are the net heat and work rates, and h values are the specific enthalpies of material streams that cross the system boundary.

Exergy balance of a system may be given as an expression in terms of the exergy destruction, $\dot{E}x_d$, as follows:

$$\dot{E}x_d = \dot{E}x^Q - \dot{W} + \sum(\dot{m}_i ex_i)_{in} - \sum(\dot{m}_i ex_i)_{out} \quad (5.4)$$

where $\dot{E}x_d > 0$, and the specific exergy of a material stream, ex , is the sum of the physical and chemical values:

$$ex_i = ex_{ph} + ex_{ch} \quad (5.5)$$

$$ex_{ph} = h - h_o - T_o(s - s_o) \quad (5.6)$$

The exergetic value of heat, $\dot{E}x^Q$, represents the quality or usefulness of the thermal energy at a source temperature T , and is equal to

$$\dot{E}x^Q = \dot{Q} \left(1 - \frac{T_o}{T} \right) \quad (5.7)$$

Exergy destruction is equivalently determined from the entropy generation rate using the relationship,

$$\dot{E}x_D = T_o \cdot \dot{S}_{gen} \quad (5.8)$$

where \dot{S}_{gen} is the entropy generation rate, and is the result of the entropy balance equation:

$$\dot{S}_{gen} = \dot{Q}/T + \sum(\dot{m}_i s_i)_{out} - \sum(\dot{m}_i s_i)_{in} \quad (5.9)$$

5.2.1 Thermophysical Properties of Material Streams

For modeling of chemical processes that involve various gas mixtures, the heat of the reaction is given by

$$H_P - H_R = \sum n_p (\bar{h}_f^\circ + \bar{h} + \bar{h}^\circ)_p - \sum n_R (\bar{h}_f^\circ + \bar{h} + \bar{h}^\circ)_R \quad (5.10)$$

where H_P and H_R are the enthalpies of the products and reactants, respectively, n is the number of moles of each species, and \bar{h}_f° , \bar{h} , and \bar{h}° are the formation, temperature specific, and standard specific enthalpies for each species.

The flow exergy of a material stream includes physical and chemical components, according to

$$\bar{e}_x = (\bar{h} - \bar{h}_o) - T_o(\bar{s} - \bar{s}_o) + \bar{e}_x^{ch} \quad (5.11)$$

Definitions of the thermophysical properties of specific heat, enthalpy, and entropy of gas mixture streams are according to the Shomate Equation, as stated by the National Institute of Science and Technology [67].

$$\bar{c}_p^\circ = A + B \cdot t + C \cdot t^2 + D \cdot t^3 + E \cdot \frac{1}{t} \quad (5.12)$$

$$(\bar{h} - \bar{h}_o) = A \cdot t + B \cdot \frac{t^2}{2} + C \cdot \frac{t^3}{3} + D \cdot \frac{t^4}{4} - E \cdot \frac{1}{t} + F - H \quad (5.13)$$

$$\bar{s} = A \cdot \ln(t) + B \cdot t + C \cdot \frac{t^2}{2} + D \cdot \frac{t^3}{3} - E \cdot \frac{1}{2t^2} + G \quad (5.14)$$

where the terms A , B , C , D , E , F , G , and H constants given by [67] and summarized in Table 5.1 for each species. The term t relates to the temperature, T (K) with the ratio:

$$t = \frac{T}{1000} \quad (5.15)$$

Table 5.1: Gas phase heat capacity inputs for Shomate Equation.

Parameter/Species	H ₂	O ₂	CO ₂	CO	H ₂ O (l)a	H ₂ O (g)b
A	33.066178	31.32234	24.99735	25.56759	-203.6060	30.09200
B	-11.363417	-20.23531	55.18696	6.096130	1523.290	6.832514
C	11.432816	57.86644	-33.69137	4.054656	-3196.413	6.793435
D	-2.772874	-36.50624	7.948387	-2.671301	2474.455	-2.534480
E	-0.158558	-0.007374	-0.136638	0.131021	3.855326	0.082139
F	-9.980797	-8.903471	-403.6075	-118.0089	-256.5478	-250.8810
G	172.707974	246.7945	228.2431	227.3665	-488.7163	223.3967
H	0.0	0.0	-393.5224	-110.5271	-285.8304	-241.8264

Source: [67]

Note: (a) 298 K ≤ T ≤ 500 K, (b) 500 K ≤ T ≤ 1700 K

5.3 Energy and Exergy of Solar Insolation

Solar insolation over the aperture surface area— G_{ap} and A_{ap} , respectively,—define energy and exergy input to the system according to,

$$\dot{E}_{in} = A_{ap}G_{ap} \quad (5.16)$$

$$\dot{E}_{x_{in}} = A_{ap}G_{Ex} \quad (5.17)$$

where the baseline case takes an average value for direct normal solar insolation to be 1000 W/m². The exergy value of the of the solar insolation at the aperture surface, G_{Ex} (W/m²) is given by [68] with respect to the direct normal beam radiation, G_{DN} , and the solar insolation at the outer surface of Earth's atmosphere, I_o , according to the equation:

$$G_{Ex} = G_{DN} \left(1 - \left(\frac{T_o}{T_s} \right) \left(\frac{G_o}{G_D} \right) \right) \quad (5.18)$$

where T_s is the temperature of the Sun—taken as 5762 K,—and the values of G_o and G_{DN} are given by [69] as the following:

$$G_o = G_{sc} \left(1 + 0.033 \cdot \cos \left(\frac{360 \cdot n_d}{365.25} \right) \right) \quad (5.19)$$

$$G_{DN} = \frac{G_{ap}}{\cos \theta_i} \quad (5.20)$$

The term G_{sc} is the solar constant insolation at the outer surface of Earth's atmosphere, and has a value of 1373 W/m^2 . The term n_d refers to the day of the year (i.e. n_d is equal to 57 for February 26th). The incident angle, θ_i , for a horizontal aperture is equal to the Zenith angle of the sun for a given location, day, and time.

5.3.1 Solar Concentration and Spectrum Splitting

The geometric concentration ratio, CR, is a ratio of the collector aperture and receiver surface areas in terms of 'Suns' (i.e. 1 Sun indicates no concentration) that represents the increase in energy intensity at the receiver, given by:

$$CR = \frac{A_{ap}}{A_r} \quad (5.21)$$

$$G_r = G_{DN} \times \frac{A_{ap}}{A_r} \quad (5.22)$$

In terms of wavelength of light, the definition of solar insolation is given in terms of the irradiance by the general equation:

$$G = \int_0^\infty I_\lambda d\lambda \quad (5.23)$$

where I_λ is the spectral irradiance that represents the light (photon) energy per unit area and wavelength, and is given by [70] as:

$$I_\lambda = e \dot{N}_{ph,\lambda} \quad (5.24)$$

The term $\dot{N}_{ph,\lambda}$ is the number of photons per unit area per second, and e is the energy of a photon at a given wavelength,

$$e = \frac{hc}{\lambda} \quad (5.25)$$

where h is Planck's constant and c is the speed of light.

Energy input to the PEC reactor and CPV components is determined by the amount of insolation received by each component. The points of interest in the model are: (1) the energy received at the aperture (Fresnel lens) surface, (2) energy of measured irradiance at the dielectric mirror surface, (3) energy of measured irradiance at the PEC photocathode surface, and (4) energy of measured irradiance at the PV module surface.

$$\dot{E}_1 = A_{\text{lens}} G_{\text{DN}} \quad (5.26)$$

$$\dot{E}_2 = A_{\text{ma}} \int_{425}^{1000} I_{\lambda} d\lambda \quad (5.27)$$

where A_{ma} is the area of the mirror array, and definition of incoming solar insolation at the surface of the dielectric mirror array is for the range from 425 nm to 1200 nm, according to the specifications given in Table 3.2. The experimental value is The dielectric mirror reflects wavelengths from 425 nm to 750 nm onto the surface of the photocathode (A_{PC}):

$$\dot{E}_3 = f_{A_{\text{PC}}} A_{\text{PC}} \int_{425}^{750} I_{\lambda} R_{\lambda} d\lambda \quad (5.28)$$

where $f_{A_{\text{PC}}}$ is the fraction of photocathode area under concentrated illumination and R_{λ} is the reflectance of the dielectric mirror.

$$\dot{E}_4 = f_{A_{\text{PV}}} A_{\text{PV}} \int_{750}^{1200} I_{\lambda} T_{\lambda} d\lambda \quad (5.29)$$

where $f_{A_{\text{PV}}}$ is the fraction of PV module area under concentrated illumination and T_{λ} is the transmittance of the dielectric mirror.

5.4 Electrochemical Modeling of the PEC Reactor

In the presence of sunlight, the hybrid photoelectrochemical (PEC) cell produces H_2 via photoelectrolysis on the photocathode and PEM electrolysis, supplied by PV electricity. When no light is available, PEM electrolysis uses stored PV electricity. The maximum electrical work requirement is equal to the Gibbs free energy,

$$W_{el} = -\Delta G \quad (5.30)$$

$$\Delta G = -nFE^0 \quad (5.31)$$

where n_e is the number of electrons, F is the Faraday constant (9.6485×10^4 C/mol), and E^0 is the standard cell potential.

For PEM electrolysis, the required cell voltage is a sum of the voltage drops due to the reversible cell potential for the water splitting reaction, and the ohmic, activation, and concentration overpotentials as follows:

$$V_{cell} = V_{rev} + V_{ohm} + V_{act} + V_{con} \quad (5.32)$$

The reversible cell voltage, V_{rev} , is the equilibrium potential defined by the Nernst equation:

$$V_{rev} = E^0 + \frac{RT}{2F} \ln \left(\frac{p_{H_2} \cdot p_{O_2}^{0.5}}{p_{H_2O}} \right) \quad (5.33)$$

where E^0 is 1.23 V, R is the universal gas constant (8.314 J/mol·K), and p_i values are the partial pressures of H_2 and O_2 products.

Ohmic overpotential, V_{ohm} , results from resistance of the membrane, R_{PEM} , to hydrogen ion transport across it as a function of thickness, δ , and ionic conductivity, σ , [35] [71], given by:

$$V_{ohm} = J \times R_{PEM} \quad (5.34)$$

$$R_{\text{PEM}} = \frac{\delta}{\sigma} \quad (5.35)$$

where the ionic conductivity is determined empirically by [72] as a function of water content of the membrane, λ_{wc} , and cell temperature:

$$\sigma_{\text{PEM}} = (0.005319 \times \lambda_{\text{wc}} - 0.00326) \exp \left[1268 \left(\frac{1}{303} - \frac{1}{T_{\text{cell}}} \right) \right] \quad (5.36)$$

Activation overpotentials of the electrodes are determined by the Butler-Volmer equation in terms of the current density, and the exchange current densities of the anode and cathode as follows:

$$J = J_0 \times \left[\exp \left(\frac{\alpha_a n_a F V_{\text{act},a}}{RT} \right) - \exp \left(- \frac{\alpha_c n_c F V_{\text{act},c}}{RT} \right) \right] \quad (5.37)$$

where α_a and α_c are transfer coefficients factors taken as 0.5 and 2, and n_a and n_c are the number of electrons transferred at the anode and cathode, with values of 4 and 2, respectively [35]. The activation overpotential of the electrodes is the sum of the anode and cathode activation overpotentials, given by:

$$V_{\text{act},a} = \frac{RT}{4\alpha_a F} \times \ln \left(\frac{J}{j_{0,a}} \right) \quad (5.38)$$

$$V_{\text{act},c} = \frac{RT}{2\alpha_c F} \times \ln \left(\frac{J}{j_{0,c}} \right) \quad (5.39)$$

where the anode and cathode exchange current densities are associated with the membrane catalyst coatings, and are $3.2 \times 10^{-5} \text{ A/m}^2$ for the Ir-Ru oxide coating on the anode side, and $1.7 \times 10^{-7} \text{ A/m}^2$ for the Pt catalyst on the cathode side [73].

The concentration overpotential does not represent a significant voltage loss for thin electrodes [74] [32] and is considered negligible for modeling purposes, thus $V_{\text{conc}}=0. \text{ V}$.

The work input and energy efficiency of the PEM electrolysis process are given by:

$$\dot{W}_{\text{cell}} = V_{\text{cell}} \times J \times A_{\text{PEM}} \quad (5.40)$$

$$\eta_{\text{PEM}} = \frac{\text{LHV}_{\text{H}_2} \times \dot{m}_{\text{H}_2}}{\dot{W}_{\text{cell}}} \quad (5.41)$$

where the electricity is supplied by the PV module, defined in the following subsection. Exergy efficiency of the PEM electrolysis is given in terms of the exergy destruction according to:

$$\dot{E}_{\text{d,PEM}} = \dot{W}_{\text{cell}} + \dot{m}_{\text{H}_2\text{O}} \text{ex}_{\text{H}_2\text{O}} - \dot{m}_{\text{H}_2} \text{ex}_{\text{H}_2} - \dot{m}_{\text{O}_2} \text{ex}_{\text{O}_2} \quad (5.42)$$

$$\psi_{\text{PEM}} = 1 - \frac{\dot{E}_{\text{d,PEM}}}{\dot{W}_{\text{cell}}} \quad (5.43)$$

The performance of PEC process for the reactor is generally in terms of the Solar-to-Hydrogen (STH) efficiency [75] [76] [77] , defined as:

$$\text{STH} = \left[\frac{|J_{\text{sc}}(\text{W}/\text{cm}^2)| \times 1.23(\text{V}) \times \eta_{\text{F}}}{P\left(\frac{\text{mW}}{\text{cm}^2}\right)} \right]_{\text{AM 1.5G}} \quad (5.44)$$

or, in relation to the applied bias, using the applied-bias photon-to-current efficiency, in the equation:

$$\text{ABPE} = \left[\frac{|J_{\text{sc}}| \times (1.23 - V_{\text{RHE}})}{P} \right]_{\text{AM 1.5G}} \quad (5.45)$$

where V_{RHE} is the applied bias potential of reference electrode (in this case, Ag/AgCl) with respect to the reference hydrogen electrode (RHE) at pH=0, and P is the intensity of light on the photocathode. The measured values are converted to RHE according to the equation:

$$V_{\text{RHE}} = V_{\text{Ag/AgCl}} + E_{\text{AgCl}}^0 + 0.059\text{pH} \quad (5.46)$$

For this case, $E_{\text{Ag/AgCl}}^0$ is 0.197 V at 25°C, and the pH =9 for the electrolyte.

However, this gives a negative result for applied biases greater than 1.23 V. An estimation approach by [77] calculates a maximum power point intrinsic to the photoelectrode, independent of the rest of the cell using the equation:

$$\text{ISTC} = \left[\frac{|J_{\text{photo}}(\text{W}/\text{cm}^2)| \times V_{\text{photo}}(\text{V})}{P\left(\frac{\text{mW}}{\text{cm}^2}\right)} \right]_{\eta_{\text{AM1.5G}}} \quad (5.47)$$

or approximately;

$$\text{ISTC} \cong \frac{1.23 (V_{\text{RHE}})}{U_{\text{dark}}(V_{\text{Rhe}})} \left[\frac{|J_{\text{photo}}(\text{W}/\text{cm}^2)| \times V_{\text{photo}}(\text{V})}{P\left(\frac{\text{mW}}{\text{cm}^2}\right)} \right]_{\eta_{\text{AM1.5G}}} \quad (5.48)$$

where the photocurrent, J_{photo} , is the difference between experimental current density values for dark and illuminated conditions for a photoelectrode, according to:

$$J_{\text{photo}}(\text{V}) = J_{\text{dark}}(\text{V}) - J_{\text{light}}(\text{V}) \quad (5.49)$$

The photovoltage, V_{photo} , represents the difference in applied potential for dark and light conditions to reach the same current density:

$$V_{\text{photo}}(\text{J}) = V_{\text{dark}}(\text{J}) - V_{\text{light}}(\text{J}) \quad (5.50)$$

5.3.2 PV Electricity Generation

Determination of the power generation of the PV cell supplying the electrolysis process considers an equivalent circuit (Figure 5.1) of a current source in parallel with a diode, to define the relevant current densities. It should be noted that the equations given in this subsection represent values associated with the PV only, and like terms (i.e. J_0) are not the same as those defined for current densities in the previous PEC equation definitions.

In dark conditions the cell does not generate a photocurrent and the PV cell acts as a diode. As light intensity increases, photocurrent is generated. The ideal case is given by the equation:

$$J_{\text{ph}} = J_{\text{PV}} + J_0 \left(e^{\left(\frac{qV_{\text{D}}}{k_{\text{B}}T_{\text{PV}}} \right)} - 1 \right) \quad (5.51)$$

where J_{ph} is the photocurrent density, J_{PV} is the current density across the load, and the last term represents the dark current density, where J_o is the dark saturation current density approximated by:

$$J_o = 1.5 \times 10^9 \times \exp\left(-\frac{T_g}{T_{cell}}\right) \quad (5.52)$$

for a cell emitting blackbody radiation at temperature T_{cell} , and T_g is the effective bandgap temperature defined by:

$$E_g = qV_g = kT_g \quad (5.53)$$

The photocurrent of a PV cell is given in terms of the series and shunt resistances by the equation:

$$J_{ph} = J_{PV} - J_o \left[\exp\left(\frac{q(V_{PV} + J_l A_{PV} R_s)}{n_d k T_{PV}}\right) - 1 \right] - \frac{V_l + J_l A_{PV} R_s}{R_p} \quad (5.54)$$

where V_{PV} is the voltage drop across the load, n_d is the non-ideality factor for the diode (1...2), and R_s and R_p are the series and shunt resistances. The equation for the output voltage of a solar cell when the photocurrent generation is known is given by [78] as:

$$V_{PV} = \frac{N}{\lambda_N} \ln\left(\frac{I_{ph} - I_{PV} - M I_o}{M I_o}\right) - \frac{N}{M} R_s I_{PV} \quad (5.55)$$

where N is the number of cells in series, λ_N is a material constant (given by [78] as 1/0.05 V for an Si cell), and M is the number of parallel cells.

When there is no load, the value of V_{PV} is the open circuit voltage, given by:

$$V_{oc} = n_d \left(\frac{k T_{PV}}{q} \right) \ln\left(\frac{J_{ph}}{J_o} + 1\right) \quad (5.56)$$

For the load in short circuit, the dark and shunt current densities may be considered negligible with respect to J_{ph} and is given by [70] by the equation:

$$J_{sc} \cong J_{ph} = \left(\frac{e}{h c} \right) \int_0^\infty \lambda \Phi_{e,\lambda} I_{ph,\lambda} d\lambda \quad (5.57)$$

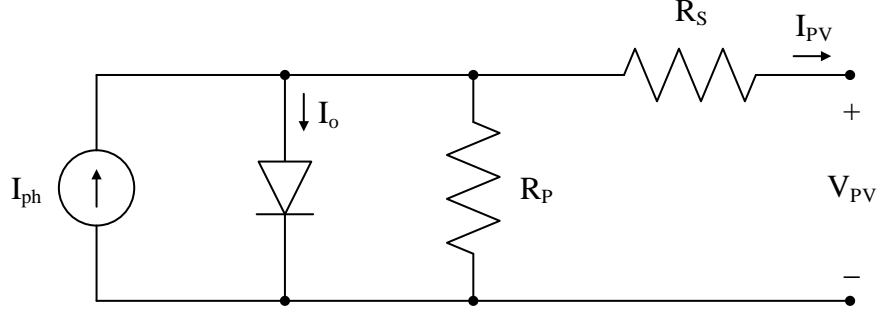


Figure 5.1: Simplified circuit diagram of a PV cell.

The fill factor and efficiency of the PV module are given for the maximum power to a resistive load in terms of V_{oc} and J_{sc} , given by:

$$FF = \frac{P_{mp}}{V_{oc} \times J_{sc} \times A_{PV}} \quad (5.58)$$

$$\eta_{PV} = \frac{P_{mp}}{G_{PV} \times A_{PV}} \quad (5.59)$$

For concentrated sunlight, the efficiency is given in terms of the solar insolation and area of the aperture (Fresnel lens), can be estimated by the equation:

$$\eta_{CPV} \approx \frac{W_{PV}}{G_{ap} \times A_{ap}} \quad (5.60)$$

However, this should also take into account the increase in temperature of the panel. According to [79], this is as a function of the concentration ratio, CR, and PV surface temperature for CPV cells with concentration less than or equal to 200 Suns with the expression:

$$\eta_{CPV} = \eta_{PV} + 0.0142 \cdot \ln(CR) + [-0.000715 + 0.0000697 \cdot \ln(CR)] \times [T(^{\circ}C) - 25^{\circ}C] \quad (5.61)$$

5.5 CPV-PEC Component and Integrated System Efficiencies

Modeling of the experimental CPV-PEC is carried out for validation of the experimental results with the integrated system analysis.

Energy and exergy efficiencies for the PEC reactor are defined as:

$$\eta_{\text{PEC}} = \frac{\text{LHV}_{\text{H}_2} \times \dot{m}_{\text{H}_2}}{\dot{E}_3 + \dot{W}_{\text{cell}}} \quad (5.62)$$

$$\psi_{\text{PEC}} = 1 - \frac{\dot{E}_{\text{xd,PEC}}}{\dot{E}_{\text{x}_3} + \dot{W}_{\text{cell}}} \quad (5.63)$$

where the exergy destruction is given by:

$$\dot{E}_{\text{xd,PEC}} = \dot{E}_{\text{x}_3} + \dot{W}_{\text{cell}} + \dot{m}_{\text{H}_2\text{O}} \text{ex}_{\text{H}_2\text{O}} - \dot{m}_{\text{H}_2} \text{ex}_{\text{H}_2} - \dot{m}_{\text{O}_2} \text{ex}_{\text{O}_2} \quad (5.64)$$

Performance of the integrated CPV-PEC must account for the efficiencies of the PEC and PV module as well the transmission losses from the concentrating lens to the respective components. For solar concentration and splitting, losses occur between from lens to mirror (1-2), mirror to PEC (2-3), and mirror to PV (2-4). The equations are given by:

$$\eta_{1-2} = \frac{\dot{E}_2}{\dot{E}_1} \quad (5.65)$$

$$\psi_{1-2} = \frac{\dot{E}x_2}{\dot{E}x_1} \quad (5.66)$$

$$\eta_{2-3} = \frac{\dot{E}_3}{\dot{E}_2} \quad (5.67)$$

$$\psi_{2-3} = \frac{\dot{E}x_3}{\dot{E}x_2} \quad (5.68)$$

$$\eta_{2-4} = \frac{\dot{E}_4}{\dot{E}_2} \quad (5.69)$$

$$\psi_{2-4} = \frac{\dot{E}x_4}{\dot{E}x_2} \quad (5.70)$$

Overall energy and exergy efficiencies of the CPV-PEC for hydrogen production are given by the equations:

$$\eta_{\text{CPV-PEC}} = \frac{\dot{m}_{\text{H}_2} \text{LHV}_{\text{H}_2}}{\dot{E}_1} \quad (5.71)$$

$$\Psi_{\text{CPV-PEC}} = \frac{\dot{m}_{\text{H}_2} \text{ex}_{\text{H}_2}}{\dot{E}x_1} \quad (5.72)$$

Where \dot{E}_1 and $\dot{E}x_1$ are the energy and exergy values for the solar input according to eqs. (5.16) and (5.17).

5.6 Analysis of Integrated Systems for Solar Fuel Synthesis

5.6.1 Methanol Synthesis Plant

For the integrated methanol plant analysis, the general equations for energy and exergy balances are given for the common components present in the system for modeling purposes.

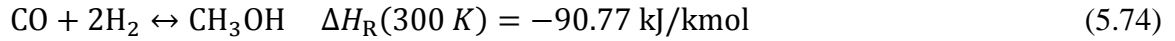
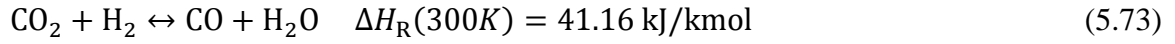
Table 5.2: Mass, energy, entropy, and exergy balance equations of common components.

Component	Balance Equations ^a	Component Efficiency
Compressor	<ul style="list-style-type: none"> $\dot{m}_i = \dot{m}_e$ $\dot{m}_i h_i + \dot{W}_j = \dot{m}_e h_e$ $\dot{m}_i s_i + \dot{S}_{\text{gen},j} = \dot{m}_e s_e$ $\dot{m}_i \text{ex}_i + \dot{W}_j = \dot{m}_e \text{ex}_e + \dot{E}x_{d,j}$ 	<ul style="list-style-type: none"> $\eta_{C,s} = (h_{e,s} - h_i)/(h_e - h_i)$ $h_{e,s} = h(P_e, s_i)$
Turbine	<ul style="list-style-type: none"> $\dot{m}_i = \dot{m}_e$ $\dot{m}_i h_i = \dot{m}_e h_e + \dot{W}_j$ $\dot{m}_i s_i + \dot{S}_{\text{gen},j} = \dot{m}_e s_e$ $\dot{m}_i \text{ex}_i = \dot{m}_e \text{ex}_e + \dot{W}_j + \dot{E}x_{d,j}$ 	<ul style="list-style-type: none"> $\eta_{T,s} = (h_i - h_e)/(h_i - h_{e,s})$ $h_{e,s} = h(P_e, s_i)$
Pump	<ul style="list-style-type: none"> $\dot{m}_i = \dot{m}_e$ $\dot{m}_i h_i + \dot{W}_j = \dot{m}_e h_e$ $\dot{m}_i s_i + \dot{S}_{\text{gen},j} = \dot{m}_e s_e$ $\dot{m}_i \text{ex}_i + \dot{W}_j = \dot{m}_e \text{ex}_e + \dot{E}x_{d,j}$ 	<ul style="list-style-type: none"> $\eta_{P,s} = (h_{e,s} - h_i)/(h_e - h_i)$ $h_{e,s} = h(P_e, s_i)$
Heat Exchanger	<ul style="list-style-type: none"> $\sum \dot{m}_i = \sum \dot{m}_e$ $\sum \dot{m}_i h_i = \sum \dot{m}_e h_e + \Delta \dot{Q}_j$ $\sum \dot{m}_i s_i + \dot{S}_{\text{gen},j} = \sum \dot{m}_e s_e + \frac{\Delta \dot{Q}_j}{T_o}$ $\sum \dot{m}_i \text{ex}_i = \sum \dot{m}_e \text{ex}_e + \dot{E}x_j^Q + \dot{E}x_{d,j}$ 	<ul style="list-style-type: none"> $\varepsilon_{\text{HX}} = \dot{Q}_{\text{useful}}/\dot{Q}_{\text{max}}$ $\dot{Q}_{\text{max}} = (\dot{m}_i c_{p,i})_{\text{min}} \cdot (T_{\text{max}} - T_{\text{min}})$
Expansion valve	<ul style="list-style-type: none"> $\dot{m}_i = \dot{m}_e$ $h_i = h_e$ $\dot{m}_i s_i + \dot{S}_{\text{gen},j} = \dot{m}_e s_e$ $\dot{m}_i \text{ex}_i = \dot{m}_e \text{ex}_e + \dot{E}x_{d,j}$ 	<ul style="list-style-type: none"> --

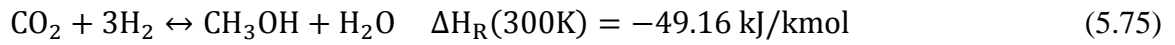
a. Balance equations refer to inlet (i) and exit (e) streams of j-component.

CO₂ Hydrogenation Reaction

Methanol synthesis takes place in two steps: first, the reverse water gas shift (RWGS) produces CO product, which leads to the second step of direct CO hydrogenation. The reactions are stated as follows:



The overall reaction for CO₂ hydrogenation occurs according to:



For the reversible reaction, definitions for the equilibrium constants of the CO hydrogenation (K_{PA}), RWGS (K_{PB}), and CO₂ hydrogenation (K_{PC}) reactions are given by [80] according to:

$$\ln K_{\text{PA}} = \frac{9.8438 \times 10^4}{RT} - 29.07 \quad (5.76)$$

$$\ln K_{\text{PB}} = \frac{-4.3939 \times 10^4}{RT} + 5.639 \quad (5.77)$$

$$K_{\text{PC}} = K_{\text{PA}} \times K_{\text{PB}} \quad (5.78)$$

Methanol Plant Efficiency

Energy and exergy efficiencies describe the performance of the solar methanol plant with the ratio of useful output (fuel) to total solar energy input, given by:

$$\eta = \frac{\dot{m}_{\text{CH}_3\text{OH}} \cdot \text{LHV}_{\text{CH}_3\text{OH}}}{\dot{E}_{\text{in}}} \quad (5.79)$$

$$\psi = \frac{\dot{m}_{\text{f}} \cdot \text{ex}_{\text{f}}}{\dot{E}_{\text{xin}}} \quad (5.80)$$

where LHV_{f} and ex_{f} are the lower heating value and chemical exergy of methanol, with values of 23 MJ/kg and 22.2 MJ/kg, respectively.

5.6.2 Freshwater Production via Seawater Reverse Osmosis (SWRO)

The recovery ratio of the RO desalination process, r_r , determines the intake seawater mass flowrate to produce the necessary fresh water to supply for electrolysis according to the expression:

$$\dot{m}_{\text{SWRO}} = \dot{m}_{\text{PW}}/r_r \quad (5.81)$$

where \dot{m}_{SWRO} and \dot{m}_{PW} are mass flowrates of the intake seawater and permeate water, respectively, and the process recovery rate is 35% [64] for the system assumptions. Through mass balance, the brine flowrate is the difference of the seawater and permeate streams, given by

$$\dot{m}_{\text{SWRO}} = \dot{m}_{\text{PW}} + \dot{m}_{\text{brine}} \quad (5.82)$$

The pump work for the low and high pressure pumps, and the energy recovery turbine are determined from the volume flow rate of seawater brine streams according to

$$\dot{W}_p = \frac{\dot{V}_{\text{SWRO}} \Delta P}{\eta_p} \quad (5.83)$$

$$\dot{W}_{\text{ERT}} = \dot{V}_{\text{brine}} \Delta P \times \eta_T \quad (5.84)$$

The specific energy demand defines the performance of the RO process, and is the net pumping and recovery work to produce the permeate water flowrate, given by:

$$w_{\text{SWRO}} = \frac{\dot{W}_{\text{SWRO}}}{\dot{V}_{\text{PW}}} \quad (5.85)$$

where \dot{V}_{PW} is the permeate volumetric flowrate, and \dot{W}_{SWRO} is the net work of the low and high pressure pumps and energy recovery turbine components,

$$\dot{W}_{\text{SWRO}} = \dot{W}_{\text{LPP}} + \dot{W}_{\text{HPP}} - \dot{W}_{\text{ERT}} \quad (5.86)$$

The value of w_{SWRO} is typically in the range of 6.5 to 24 kWh/m³ for RO desalination with no energy recovery [81], and 3.0 to 3.5 kWh/m³ for processes with recovery options.

5.6.3 CO₂ Capture from Seawater

Bipolar Membrane Electrodialysis (BPMED) (System I)

The BPMED process for CO₂ extraction from seawater, shown schematically in Figure 4.4, converts dissolved carbon in seawater to CO₂ gas according to the overall reaction:



The specific electrochemical energy consumption of the electrodialysis process is 242 kJ/mol-CO₂ [82], and the power requirement is calculated:

$$\dot{W}_{\text{BPMED}} = \frac{VJA_{\text{mem}}}{\dot{N}_{\text{CO}_2}(T_o, P_o)} \quad (5.88)$$

where V is the applied voltage, J is the current density applied to the BPMED unit, and A_{mem} is the total membrane area for the unit. The required flowrate of seawater for CO₂ is given by:

$$\dot{V}_{\text{SW,BPMED}} = \dot{m}_{\text{CO}_2} / (\eta_{\text{CO}_2, \text{BPMED}} \times 0.1) \quad (5.89)$$

where $\eta_{\text{CO}_2, \text{BPMED}}$ is the ratio of extracting CO₂ from seawater containing 0.1 kg-CO₂/m³, and has a value of is 59% [65].

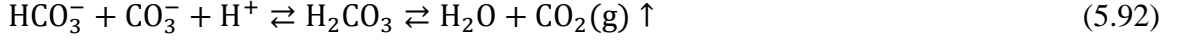
H₂ and CO₂ Capture via Electrolytic Cation Exchange Membrane (E-CEM) (System II)

Extraction of H₂ and CO₂ from seawater uses the E-CEM by [66]. The reactor has three compartments, shown schematically in Figure 4.6. The reactions in the anode and cathode compartments are as follows:





In the centre compartment, bicarbonate and carbonate ions equilibrate to carbonic acid with addition of protons according to the reaction:



The specific energy demand of the E-CEM process is given by [66] as 49 kWh/m³-H₂ (STP), and defines the total electricity demand according to the equation:

$$\dot{W}_{\text{ECEM}} = w_{\text{ECEM}} \times \dot{V}_{\text{H}_2}(\text{T}_0, \text{P}_0) \quad (5.93)$$

where the theoretical molar flowrates of H₂ and CO₂ result from the stoichiometric ratios for the methanol synthesis reaction in eq.s (5.53)-(5.55), and have a mole ratio of 3:1 at the outlet of E-CEM. The flowrate of seawater is taken on the basis of CO₂ content and conversion efficiency, according to

$$\dot{V}_{\text{SW}} = \dot{m}_{\text{CO}_2} / (\eta_{\text{CO}_2} \times 0.1) \quad (5.94)$$

where η_{CO_2} is the ratio of extracting CO₂ from seawater containing 0.1 kg-CO₂/m³, and has a value of is 92% when the pH of the effluent stream from the centre compartment is ≤ 4 , and ranges from approximately 70% to 92% for less acidic streams from $4 \leq \text{pH} \leq 6$.

5.6.4 Energy and Exergy Efficiencies of Integrated Systems

System I

The energy and exergy efficiencies for System I considers the CPV-PEC, and additional CPV-generated electricity input for freshwater production, CO₂ capture, and methanol synthesis, according to the equations:

$$\eta_{\text{SysI}} = \frac{\dot{m}_{\text{CH}_3\text{OH}} \cdot \text{LHV}_{\text{CH}_3\text{OH}}}{\dot{E}_{\text{CPV-PEC}} + \frac{\dot{W}_{\text{el}}}{\eta_{\text{CPV}}}} \quad (5.95)$$

$$\psi_{\text{SysI}} = \frac{\dot{m}_{\text{CH}_3\text{OH}} \cdot \text{ex}_{\text{CH}_3\text{OH}}}{\dot{\text{Ex}}_{\text{CPV-PEC}} + \frac{\dot{W}_{\text{el}}}{\psi_{\text{CPV}}}} \quad (5.96)$$

Integrated System II

For System II, The equations are given for energy and exergy efficiencies as follows:

$$\eta_{\text{SysII}} = \frac{\dot{m}_{\text{CH}_3\text{OH}} \cdot \text{LHV}_{\text{CH}_3\text{OH}}}{\frac{\dot{W}_{\text{el}}}{\eta_{\text{CPV}}}} \quad (5.97)$$

$$\psi_{\text{SysII}} = \frac{\dot{m}_{\text{CH}_3\text{OH}} \cdot \text{ex}_{\text{CH}_3\text{OH}}}{\frac{\dot{W}_{\text{el}}}{\psi_{\text{CPV}}}} \quad (5.98)$$

5.7 Exergoeconomic Analysis

The exergoeconomic analysis first considers the three-step SPECO method [83]; (i) identification of exergy streams, (ii) fuel and product definition, and (iii) application of cost equations. The cost rate, \dot{C} , for input and output exergy streams is defined as,

$$\dot{C} = c \cdot \dot{\text{Ex}} \quad (5.99)$$

where c is the unit cost of exergy in \$/kWh for matter, electricity, and heat flows as inputs or outputs of the system. The general balance for the cost rate considering heat, work, materials, and capital cost is given by,

$$\sum \dot{C}_{\text{in}} + \dot{W} c_{\text{in}} + \dot{Z} = \sum \dot{C}_{\text{out}} + \dot{W} c_{\text{out}} \quad (5.100)$$

A component capital cost, \dot{Z} , represents the lifecycle cost in \$/h for a component for the construction, operation and maintenance, and disposal stages.

$$\dot{Z} = \frac{Z_k \text{CRF} \phi}{N \cdot 3600} \quad (5.101)$$

where CRF is the capital recovery factor that relates to the lifetime of the equipment and the interest rate, according to:

$$CRF = \frac{i(1+i)^n}{(1+i)^n - 1} \quad (5.102)$$

where i is the interest rate and n is the operating lifetime of the system in years. Total cost of the system in \$/h considers capital costs and operation and maintenance cost, and divides the total by number of hours of operation per year. Operation and maintenance costs are determined as a ratio of the capital cost for a type of application and material according to:

$$OM = CC \times OM_{ratio} \quad (5.103)$$

The total capital cost of equipment is given by:

$$TCC = CRF(CC \times OM_{ratio}) \quad (5.104)$$

The lifecycle component cost, \dot{Z} , is now given in terms of the capital and O&M cost rate by the equation:

$$\dot{Z} = \frac{TCC}{t_{op}[h/year]} \quad (5.105)$$

Estimation of the purchase cost of various system components uses an equipment capacity based equation [84] [85],

$$\log(Z) = K_1 + K_2 \log(A) + K_3 [\log(A)]^2 \quad (5.106)$$

where the resulting value is the cost estimation in 2001\$, A is the capacity of the component, and K_i values are equipment-specific coefficients, listed in Table 5.3. Cost rate of exergy destruction, \dot{C}_D , takes into account capital and lifecycle costs, and is used to define the exergoeconomic cost factor, f , according to the equations:

$$\dot{C}_D = c_{in} \cdot \dot{E}x_D \quad (5.107)$$

$$f = \frac{\dot{Z}}{\dot{Z} + \dot{C}_D} \quad (5.108)$$

Table 5.3: Equipment coefficients for purchase cost estimations.

Coefficient \ Component	Heat Exchanger	Compressor	Pump	Reactor	Mixer
A	Area (m2)	Power (kW)	Power (kW)	Volume (m3)	Volume (m3)
K1	4.3247	2.2897	3.8696	3.4974	5.0141
K2	-0.303	1.3604	0.3161	0.4485	-0.4133
K3	0.1643	-0.1027	0.122	0.1074	0.3224

Source: [85]

5.8 Exergoenvironmental Analysis

Exergoenvironmental analysis combines the concepts of exergy analysis and lifecycle analysis (LCA) to assess the performance of a system by quantifying the environmental impact(s) of the exergy streams and system components. The method for exergoenvironmental analysis is analogous to the exergoeconomic analysis in the study by [86], following three steps: (i) definition of the exergy streams, (ii) conduct life cycle analysis, and (iii) assign an environmental impact factor to matter, electricity, and heat exergy streams. The environmental impact rate, \dot{B} , is given by:

$$\dot{B} = b \cdot \dot{E}_x \quad (5.109)$$

where b is the environmental impact per unit exergy.

For chemical reactions, it is important to define both the chemical and physical exergy components for the process.

$$\dot{B} = b^{ch} \dot{E}_x^{ch} + b^{ph} \dot{E}_x^{ph} \quad (5.110)$$

Component related impact, \dot{Y} , and the impact of pollutant formation, \dot{B}^{PF} , (i.e. GHG emissions) is considered within the environmental impact rate by the equation:

$$\dot{B}_p = \dot{B}_p + (\dot{Y} + \dot{B}^{PF}) \quad (5.111)$$

Environmental impact of exergy destruction, \dot{B}_{dest} , the exergoenvironmental impact factor, f_b , are given by:

$$\dot{B}_D = b_{\text{in}} \cdot \dot{E}x_D \quad (5.112)$$

$$f_b = \frac{\dot{Y}}{\dot{Y} + \dot{B}_D} \quad (5.113)$$

The relative difference for a specific impact term, r_b , indicates the impact and potential for improvement within a system, defined by:

$$r_b = \frac{b_p - b_{\text{in}}}{b_{\text{in}}} \quad (5.114)$$

5.9 Optimization

The CPV-PEC system performance including the exergy efficiency of the CPV-PEC system, exergy efficiency of the concentrator, energy efficiency of the PV and the exergy efficiency of the PV. The main inputs of the system are the temperature of the ambient and the temperature of the PV. These are the main inputs since the system is expected to produce hydrogen from the photovoltaic reactions at any irradiance as long as there is light to excite the photochemical reaction.

The multi-objective optimization of the CPV-PEC system is done through the integration of the neural network, which produces a relationship between the inputs and the outputs of the system. Then the neural network generated function is used to optimize the overall system through the genetic algorithm in Matlab. The objective function of the multi-objective optimization can be written as follows:

$$(\dot{W}_{\text{PV}}, \psi_{\text{CPV-PEC}}, \psi_{\text{conc}}, \psi_{\text{PV}}) = f(T_{\text{PV}}, T_o) \quad (5.115)$$

Optimization of the CPV-PEC system is carried out through the integration of neural network and the genetic algorithm using Matlab software. The developed model was

ran through a set of ranges of the main operating parameters mentioned above and presented in Equation (--). The resulting outputs of the simulated model based on the selected ranges of the operating parameters were exported to the neural network. The neural network in the carried out optimization presents only a connection point between the Matlab based multi-objective optimization and the developed model on EES. This connection is made in order to be able to use the multi-objective optimization using the genetic algorithm method in Matlab.

The neural network as mentioned earlier is the connection link between the GA and the EES model. Rather than having the GA run different cases through its evolution derived algorithm in EES model, all generated different cases based on the simulation in ESS parametric studies are passed to the neural network to establish the connection with the genetic algorithm. Finding the relationship describing analytically the relationship between the system inputs and outputs is a very complex due to couple of reasons, first, the system is simulated with process simulation software with a number of material properties that it a function of a thermophysical properties and, second, the system has a large number of components and streams. Alternatively, the relationship can be found by using regression modeling for a specific range of inputs, while another alternative is to use one of the computer learning methods, the Neural Network. The Neural Network is a computer artificial learning model that simulates the deep learning in a human brain, specifically the structure and connection of the brain neurons and tries to find a relationship between a group of variables and outputs. Neurons are often used in the network simulate nonlinear and typically analog computational features. There are a various models of the neural network and the selected is the two-layer feed-forward Neural Network with sigmoid

hidden neurons and liner output neurons. The selected model can fit a multi-dimensional mapping problems as long as there is an appropriate number of neurons in the hidden layers and a consistent data.

The data produced by the developed model that are used to train the neural network model for the proposed and developed system in this study include two input and four output data sets. The selected neural network training method is the Bayesian Regulation method, which is utilized for training the neural network model, using Matlab as mentioned earlier. The selection of the training method was based on the literature, where several research such as Bicer et al [87] have adapted that method during the development of a dynamic response and modeling the behavior of a proton exchange membrane fuel cell. Bicer et al [87] reported that the Bayesian Regulation method consumed less time and provided a better accuracy compared to other available training methods.

The GA method is inspired by natural evolution theory [87] [88], where the strongest individuals in a species have a better opportunity to pass along genes to offspring and eventually become dominant within a population. Natural selection eliminates unsuccessful individuals. In the GA method, a solution vector \mathbf{x} is identified as an individual (or chromosome) [88] with a certain set of genes, and a collection of these individuals are a population that is randomly initialized. GA uses two operators to form new solutions from the existing ones – crossover and mutation. For crossover, two individuals (parents) combine to form new chromosomes, or offspring. The parents are selected from the existing population by a preference toward fitness, in that the offspring inherit good genes and the parents are considered fitter. Through iteration of the crossover operator, genes of good individuals occur more frequently throughout the population and

eventually converge to an optimal solution. Mutation introduces diversity at the gene level, where the mutation rate is the probability of property changes in a gene. This allows the search to escape local optima [88] and find global optima.

CHAPTER 6: RESULTS AND DISCUSSION

6.1 Introduction

This chapter presents the results of the CPV-PEC experimental and theoretical investigation, modeling results of the integrated solar H₂ and methanol synthesis processes for Systems I and II. Experimental and modeling results for the CPV-PEC sub processes and for the integrated system study are given in the following order:

- Solar concentration and spectrum splitting,
- PEC reactor performance: electrolyser and photoelectrochemical characterization and H₂ production ,
- PV electricity generation in ambient and concentrated sunlight,
- Integrated CPV-PEC performance,
- Exergoeconomic and environmental modeling and optimization of the CPV-PEC H₂ production process.

Resulting operating conditions for the CPV-PEC H₂ process are applied in the System I model for solar-based methanol synthesis, and results are compared with those of the initial case study for System II.

6.2 CPV-PEC Experimental Results and Model Validation

The experimental measurements and calculated values are subject to device and statistical error that propagate within the results. Table 6.1 summarizes the error values for measurements associated with the primary devices used while conducting experiments for measuring and recording data. Furthermore, efforts to conduct the outdoor experiments in a consistent manner reduce additional random/rough errors. Outdoor placement of the

CPV-PEC apparatus is maintained, and data with significant outliers due to overhead cloud passage are re-taken under more consistent sky conditions.

Table 6.1: Measurement Uncertainties

Variable	Device	Ref. Value	Bias Error	Rel. Bias Error %	Statistical Uncertainty %	Absolute Uncertainty %
Potential	Gamry Reference 3000 Potentiostat	2 V	0.006 V	0.3	2.13	2.15
Current	Gamry Reference 3000 Potentiostat	2 A	0.012 A	0.24	1.30	1.32
Irradiance	Trisol Solar Simulator TSS-208	1000 W/m ²	± 20.28 W/m ²	2.03	0.23	2.04
Irradiance	Vernier Pyranometer	1000 W/m ²	50 W/m ²	5.0	2.74	5.70
Temperature	Vernier Temperature Sensor	53 °C	0.5 °C	0.94	2.24	2.43
Spectrum	Ocean Optics Red Tide USB 650 Spectrometer	700 nm	0.350 nm	0.05	0.56	0.56

6.2.1 Solar Concentration and Spectrum Splitting

Modeling of ambient and concentrated solar irradiance uses the ASTM G173 reference spectra data from NREL [89] to determine the ambient and concentrated energy of the reflected and transmitted wavelengths of light. Extraterrestrial insolation entering Earth's atmosphere loses energy as it travels to ground level due to reflection and refraction with air, and environmental interference (i.e. water vapour).

The global insolation at ground level is made of direct beam insolation, which is normal to Earth's surface, and diffuse insolation, which scatters light. This distribution is shown for the full spectrum (microwave, visible, and infrared) in Figure 6.1.

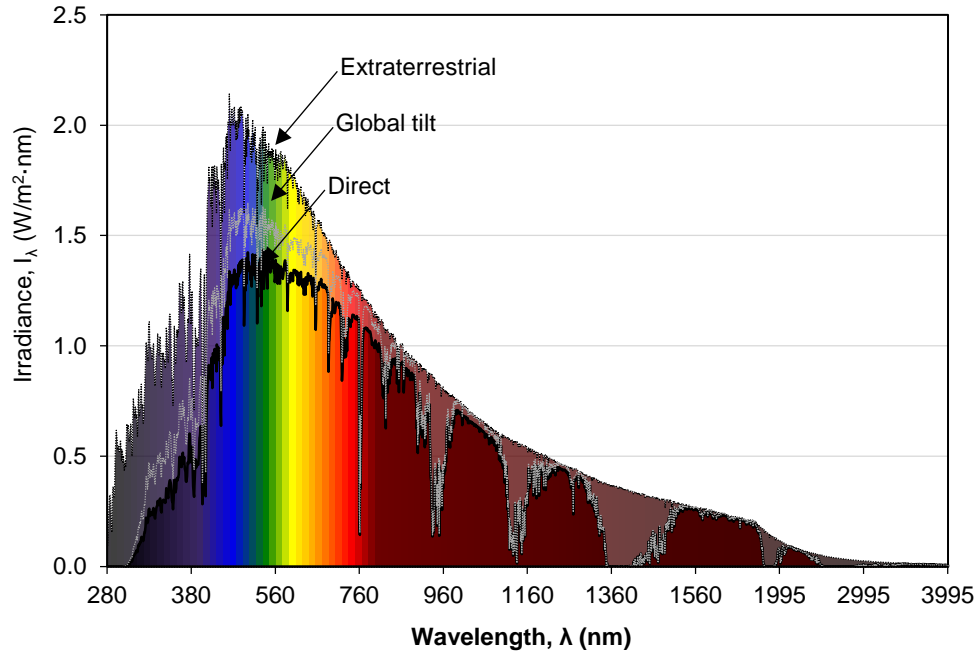


Figure 6.1: Spectral irradiance levels (ASTMG173 spectra data from [89]).

For solar concentration, the Fresnel lens focuses only direct beam radiation, and the dielectric mirror interacts with wavelengths ranging from 425 nm to 1200 nm. This useable range is shown in Figure 6.2 for the non-concentrated (ambient) level.

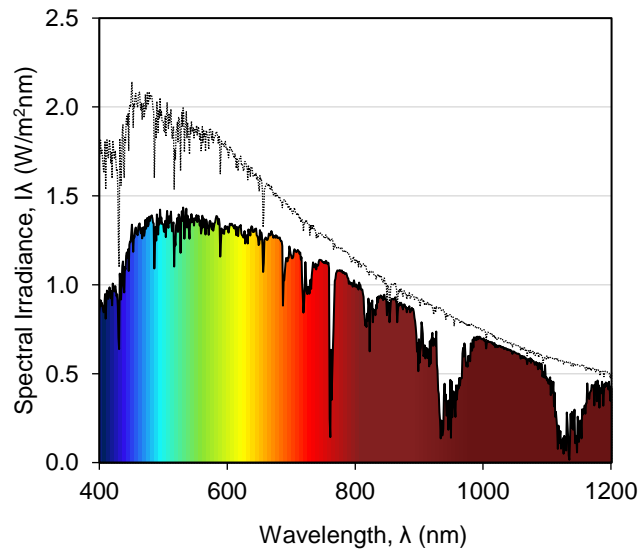


Figure 6.2: Direct beam spectral irradiance for dielectric mirror range.

Integration of the direct irradiance values determines the solar energy flux at the surface of the concentrating Fresnel lens, which represents the energy input for the CPV-PEC system. The spectrum data are applied in the solar model to determine the theoretical concentrated solar irradiance received by each component based on the transmission and reflection range specifications of the dielectric mirror, and plotted in Figure 6.3. Integrating these ranges gives the theoretical values of solar energy input to each device.

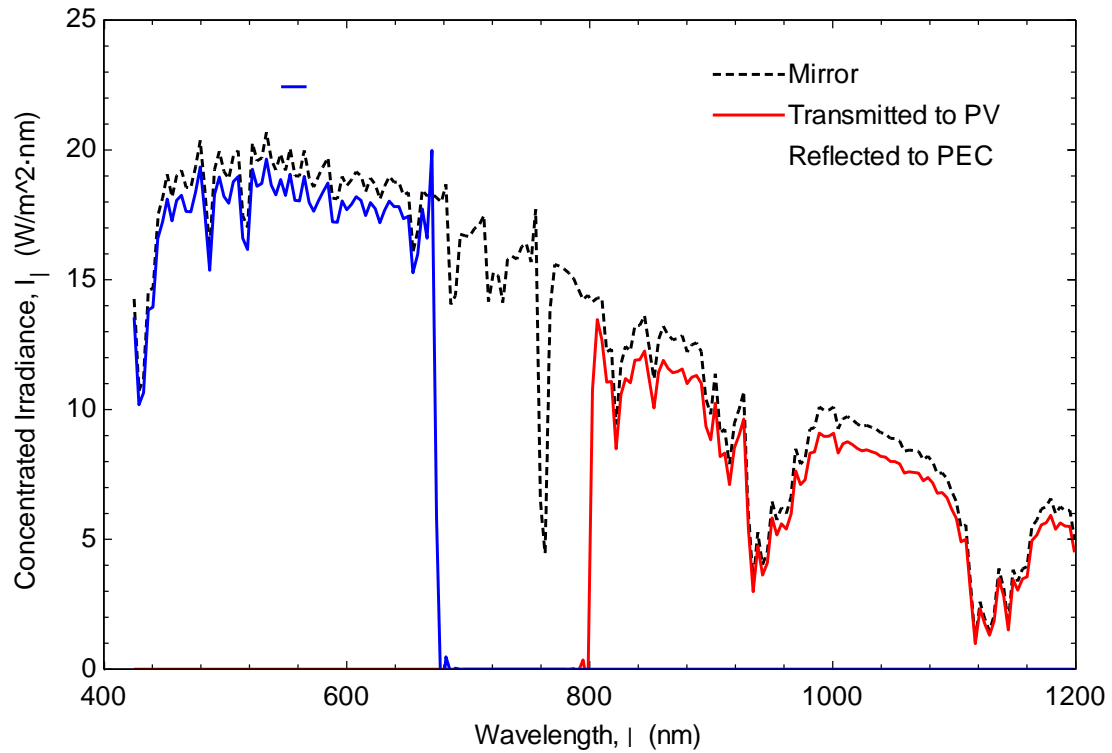
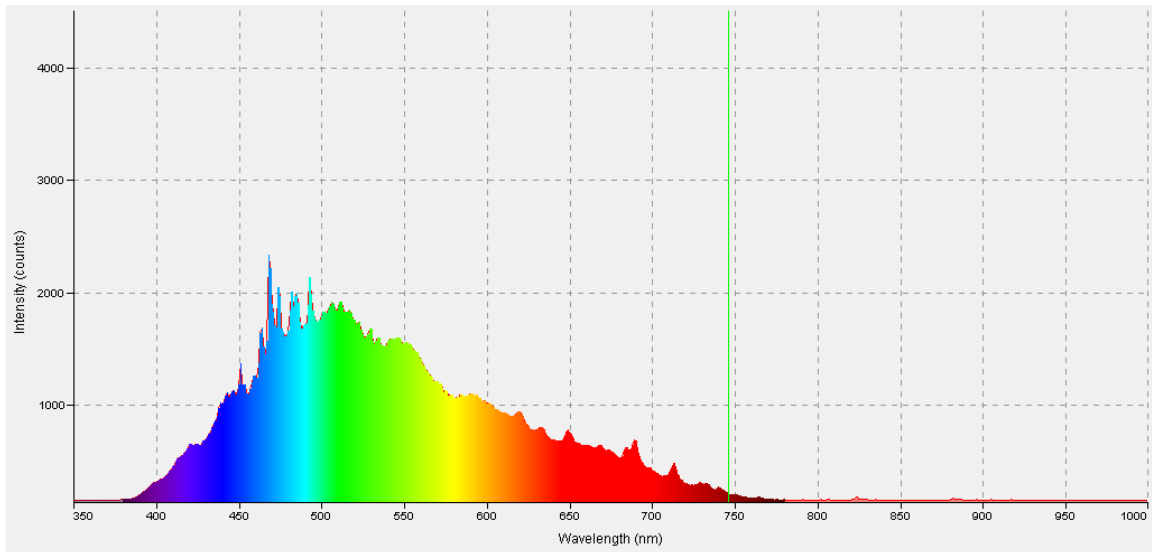


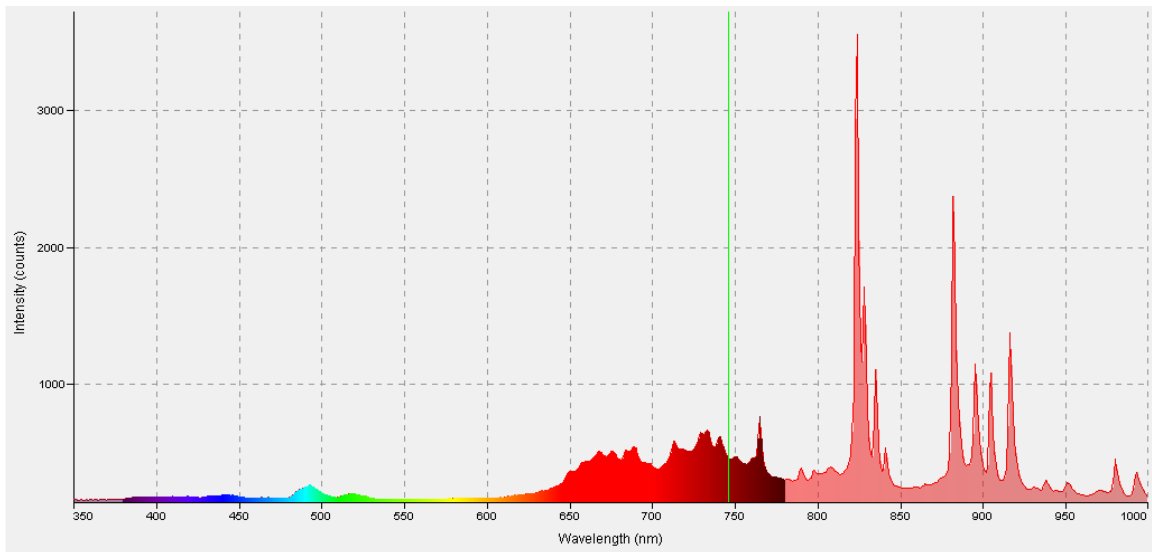
Figure 6.3: Concentrated direct solar irradiance for mirror, PV, and PEC surfaces.

Figure 6.4 shows the measured intensity of the reflected and transmitted irradiance (in counts per second) of concentrated sunlight for a clear day with ambient solar insolation measuring approximately 707.4 W/m^2 at the time of the reading. During the experiments, intensity measurements taken at the approximate centre location of each component surface record the intensity of solar light. These data determine experimental transmission and reflection percentages by the mirror at each wavelength shown in Figure 6.5, however, the

pyranometer saturates at 1000 W/m^2 cutting off a significant portion of the spectrum transmission information for the PV, which receives solar energy in the range of $800 \text{ nm} - 1200 \text{ nm}$.



(a)



(b)

Figure 6.4: Measured intensity (counts) of concentrated sunlight (a) reflected, and (b) transmitted by dielectric mirror.

Another challenge is the possibility of diffuse irradiance interference while taking measurements, but this is less significant due to the much higher intensity of concentrated light than ambient diffuse irradiance. Figure 6.6 shows the comparison of the spectral values. It is clear that there is some disagreement in the irradiance – most significantly for the light transmitted to the PV.

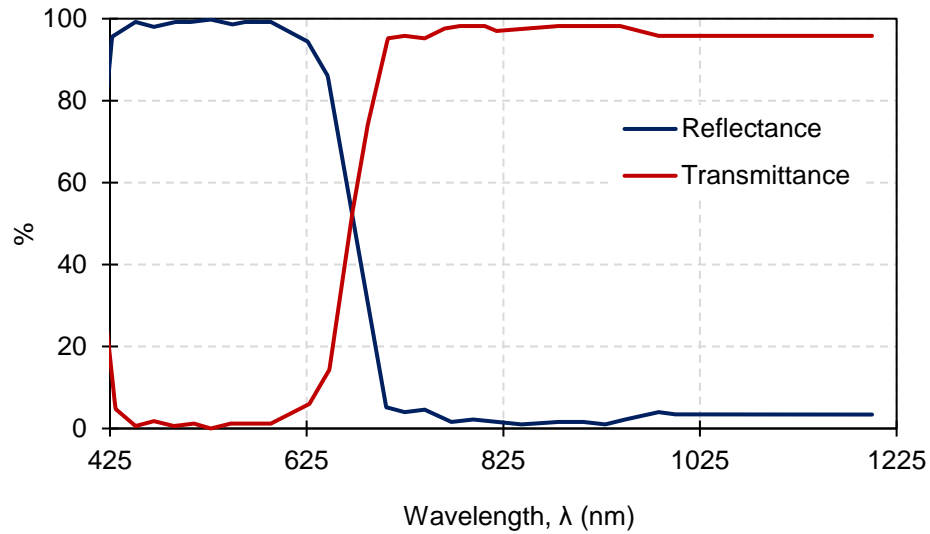


Figure 6.5: Measured reflectance and transmittance of the dielectric mirror concentrated light conditions.

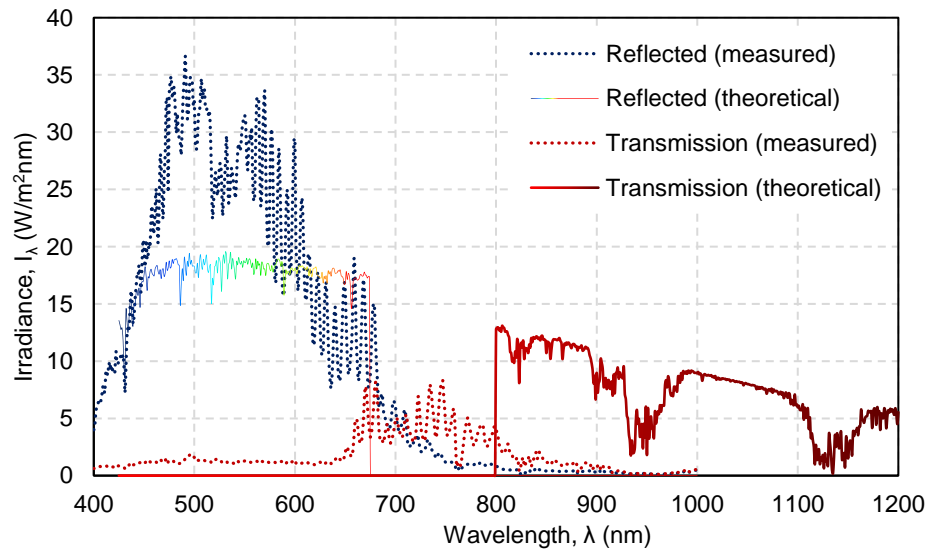


Figure 6.6: Measured and theoretical reflected solar irradiance onto PEC photocathode.

The integrated values for solar insolation, listed in Table 6.2, indicate a small percent difference between the measurement and modeled values for ambient and concentrated insolation at the lens aperture and mirror values. The theoretical model takes into account location (latitude), date, and time of day and assumes an air mass of AM1.5 to be consistent with the ASTM-G173 irradiance data. More significant percent difference values arise in the reflected and transmitted results, due in part to the difference in integration range of the measurement and modeled results – the measurement range cuts off half of the wavelength range for the PV surface by limitation at 1000 W/m².

Table 6.2: Solar insolation values for measured aperture (lens) and concentrated values.

Irradiance	Ambient (W/m ²)	Concentrated (W/m ²)		
Component	Fresnel lens, G ₁	Dielectric Mirror, G ₂	PEC, G ₃	PV, G ₄
Measurement	707.4	9330	6113	1075
Model	700.2	8597	4457	1876
% Difference	1.02	8.17	31.3	54.2

The CPV-PEC model applies the theoretical solar irradiance values to consider the wavelength range of 425nm - 1200 nm for determination of the maximum solar energy input to each component for the integrated system in Section 6.2.4.

6.2.2 Experimental PEC Reactor and PV Results

The experimental results for the PEC reactor and PV module testing under simulated and concentrated sunlight are given in this section. The concentrated sunlight results include spectrum splitting by the dielectric mirror. The Cu₂O photocathode characterization results for the photocurrent, PEC H₂ generation, and the PV electricity results are summarized.

Cu₂O Photocathode

Evaluating the photo response of the Cu₂O coating on the cathode uses linear sweep voltammetry tests under dark and light conditions. Figure 6.7 shows the increase in current density with respect to the reference hydrogen electrode (V_{RHE}) with illumination of 1000 W/m² (AM1.5) simulated sunlight over approximately 250 cm² of the 425 cm² photocathode submersed in the electrolyte (seen in Figure 6.8) with the difference between light and dark current densities representing the photocurrent density. The photocurrent and photovoltage indicated in the figure have approximate values of 0.6 mA/cm² and 0.61 V, respectively. The photovoltage represents the difference between applied voltage values in dark and light conditions for the photoelectrode to reach the same current density. According to eq. 5.48, the intrinsic conversion efficiency is 0.29% at this point.

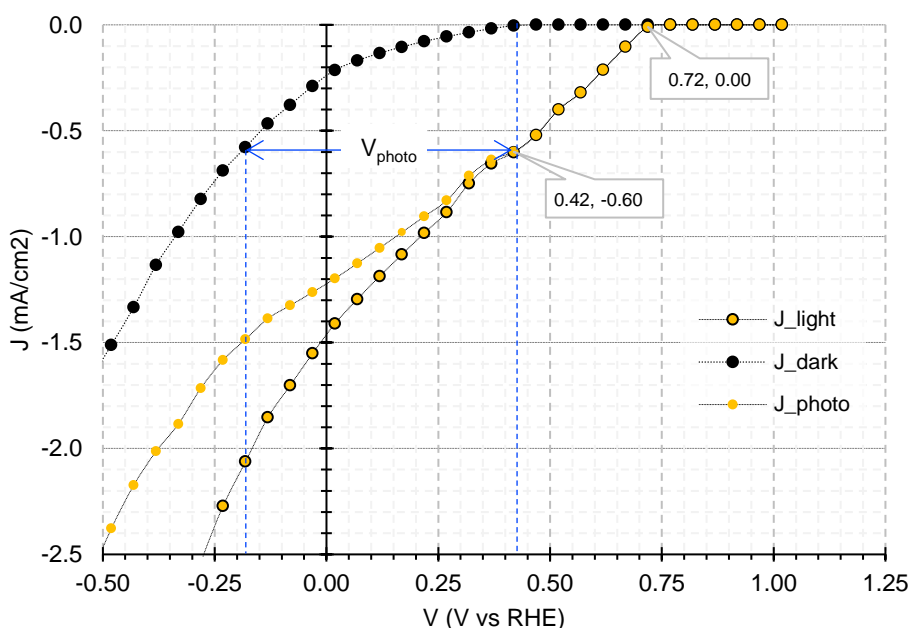


Figure 6.7: Photocurrent (J_{photo}) and photovoltage (V_{photo}) for J-V voltammograms of Cu₂O coated stainless steel photocathode plate (0.05 M NaOH electrolyte) under dark and simulated light conditions (1000 W/m² AM 1.5G).

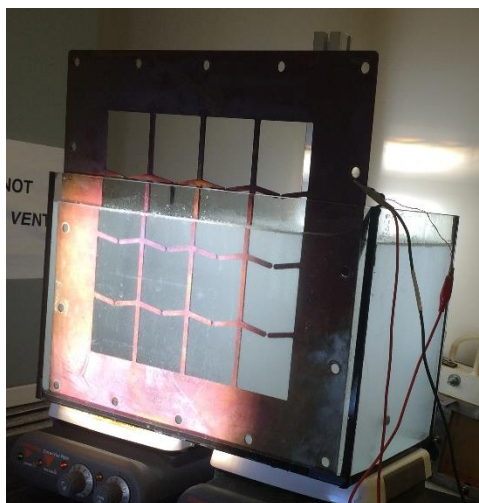


Figure 6.8: Partial illumination of Cu_2O coated stainless steel photocathode plate (0.05 M NaOH electrolyte) to simulated sunlight (1000 W/m^2 AM1.5).

The photoresponse of the cathode is tested under dark and concentrated sunlight illumination. When illuminated, the concentrated light covered approximately 25% of the total area ($\sim 200 \text{ cm}^2$), and the remaining area was exposed to ambient solar insolation, seen in Figure 6.9. The ambient solar irradiance in the solarium during the time of the scan was an average of 425 W/m^2 , and the concentrated light was approximately 1330 W/m^2 .



Figure 6.9: Photocathode testing under concentrated solar illumination.

The results of the cyclic voltammetry scan over the range of 3 V to -3 V are shown in Figure 6.10. The scan shows that in the negative sweep (0 V to -3 V), there is an increase in the magnitude of the generated current for the illuminated case indicating a p-type cathodic response by the Cu_2O photocathode.

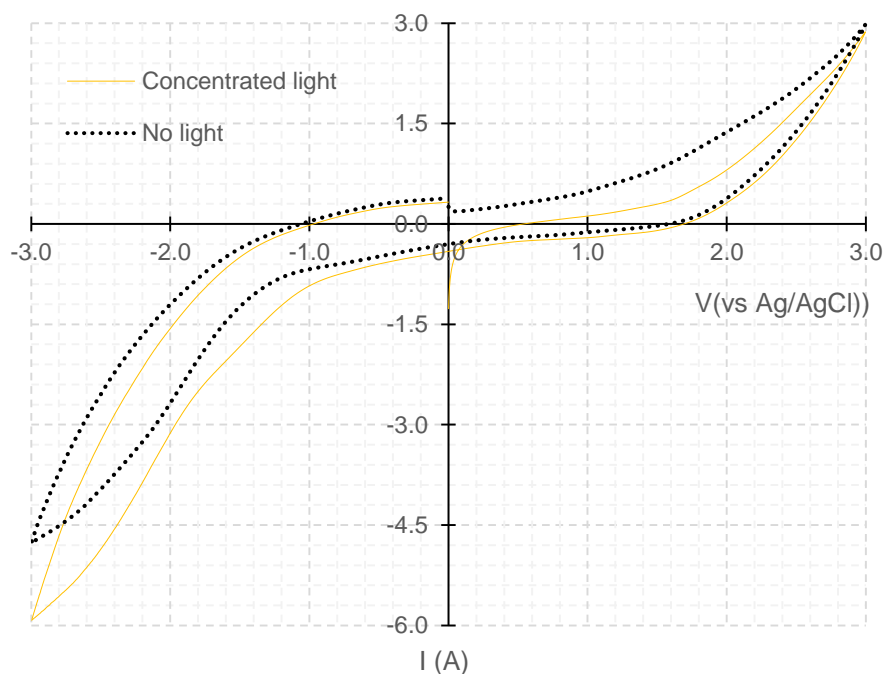


Figure 6.10: Cyclic voltammetry curve of Cu_2O photocathode plate in 0.05 M NaOH electrolyte solution under dark and concentrated light conditions.

This response is further investigated by observing the current-potential response of the photocathode to a linear potentiodynamic scan at a rate of 1 mV/s to chopped (on/off) concentrated light illumination, shown in Figure 6.11. Photocurrent density increases in magnitude with increasingly negative applied potential, consistent with p-type signal for Cu_2O coating on metal. The results show a maximum photocurrent density of approximately 0.3 mA/cm^2 for the total active surface, of which 25% was exposed to concentrated light, and the remaining to ambient light.

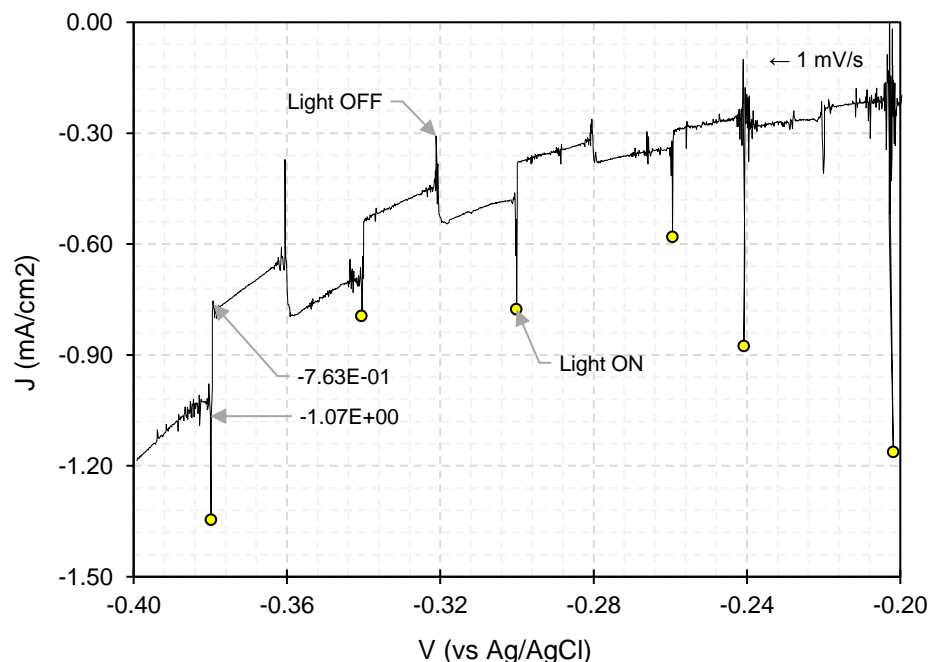


Figure 6.11: Linear sweep voltammetry for Cu_2O coated photocathode plate in 0.05 M NaOH electrolyte solution under chopped concentrated light.

PEC Hydrogen Production

A series of PEC experiments under ambient and solar concentration conditions observe the effect of applied bias on the cell current density and H_2 production rate under (reasonably) constant environmental conditions. Current measurement recordings of the PEC under concentrated light and in shadowed (low-level ambient) are taken at 1.6 V, 1.8 V, 2.0 V applied bias. Determination of photocurrent density considers an average value of 940 W/m^2 solar insolation, which ranged from 900 W/m^2 – 980 W/m^2 over the course of the testing period. Furthermore, an area factor of 0.4 is applied to the photocathode area to determine the PEC concentrated photocurrent density.

Figure 6.12 shows the current generated under concentrated and low-light conditions. It is assumed that under the low-light conditions there is insufficient light incident on the PEC cathode to generate a significant photocurrent, and is essentially

operating as a PEM electrolyser. The average photocurrent for the concentrated conditions is approximately 0.025 mA/cm^2 . The hydrogen generation for 1.6 V applied current is shown in Figure 6.13. For the concentrated conditions, the H_2 generation averages 2.65 mg/h , and for the low-light case reaches an average of 1.95 mg/h .

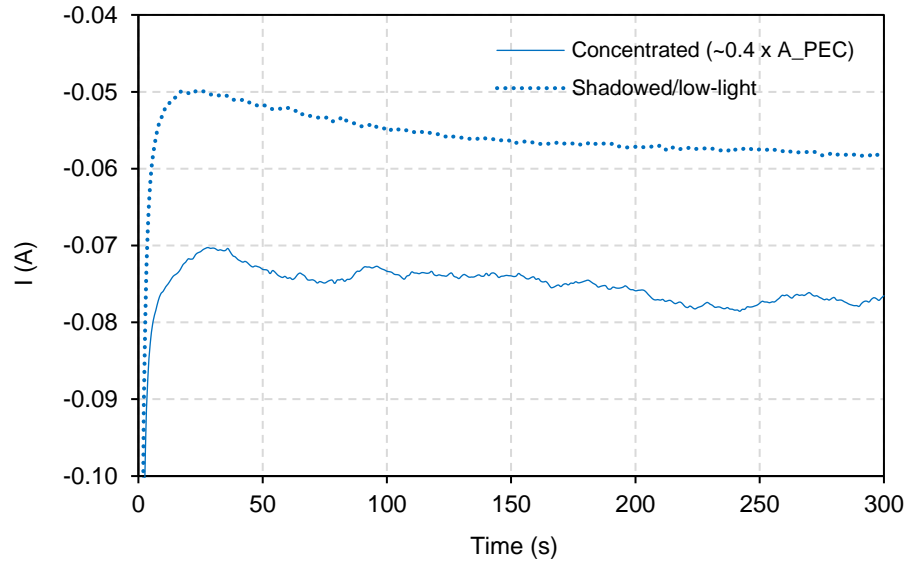


Figure 6.12: Measured current at 1.6 V for PEC operation under shadowed (low light) and concentrated solar concentration.

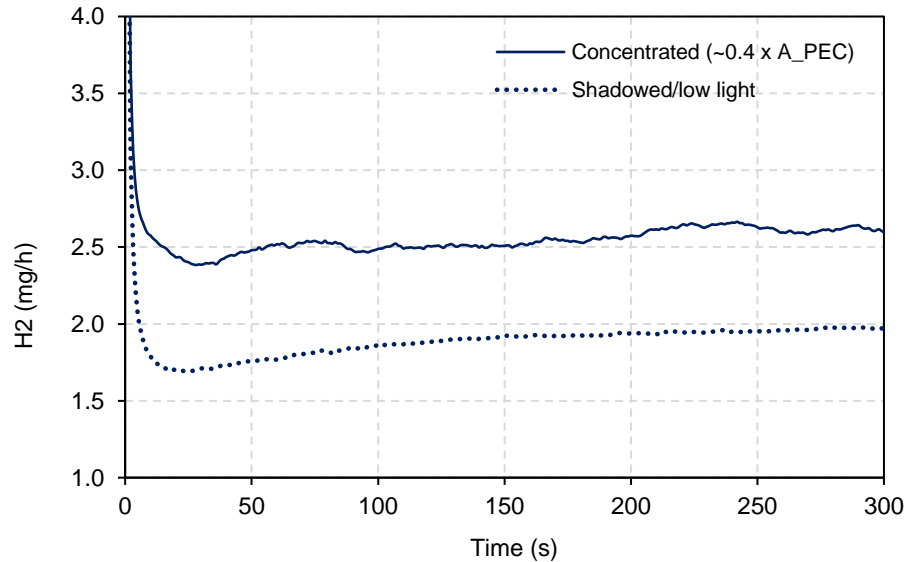


Figure 6.13: Measured H_2 production at 1.6 V for PEC operation under shadowed (low light) and concentrated solar concentration.

Figure 6.14 shows the current generation for the PEC reactor for an applied voltage of 1.8 V for the concentrated and low light case. The respective current generation for these cases show an increase for the concentrated case with spectrum splitting.

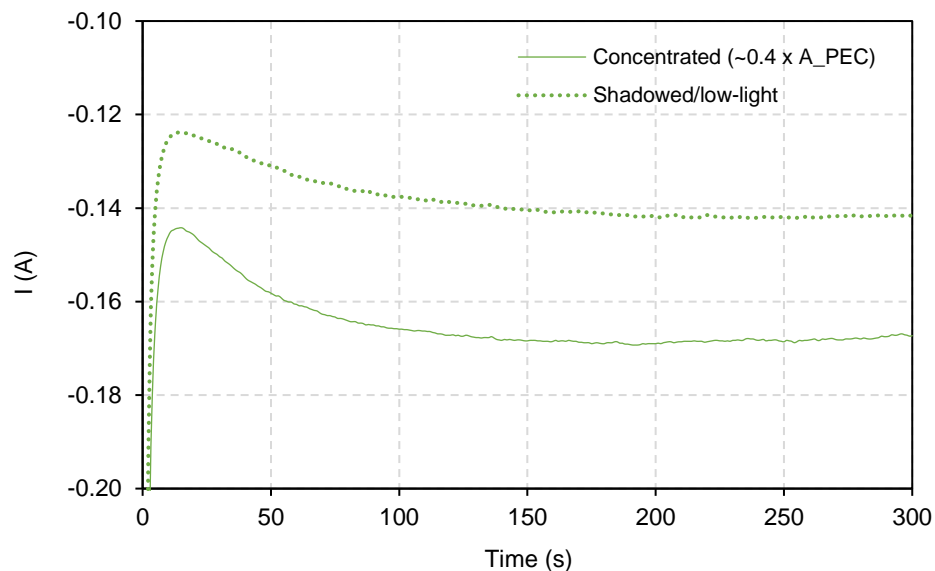


Figure 6.14: Measured current at 1.8 V for PEC operation under shadowed (low light) and concentrated solar concentration.

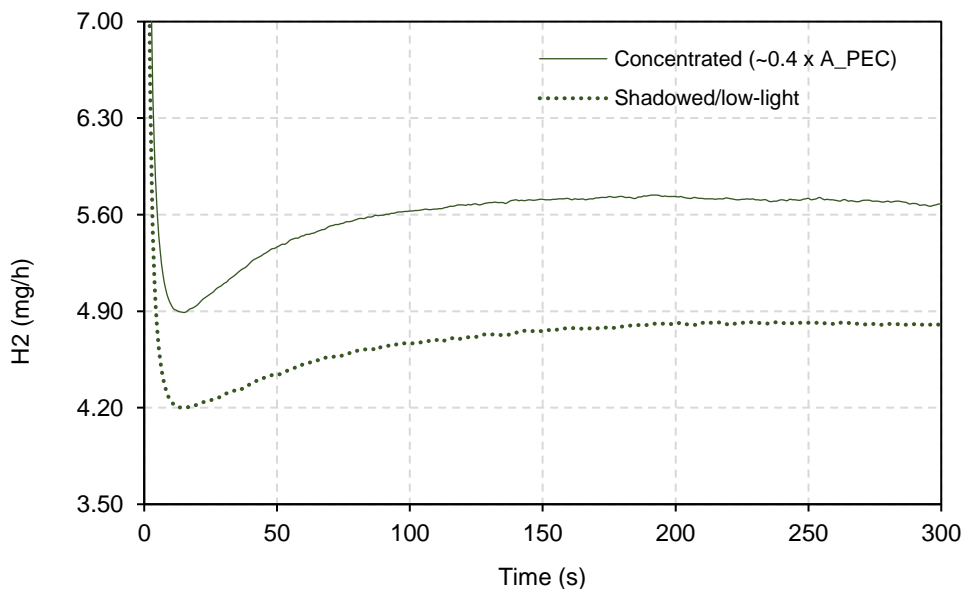


Figure 6.15: Measured H₂ production at 1.8 V for PEC operation under shadowed (low light) and concentrated solar concentration.

Figure 6.15 shows the measured hydrogen production rate 1.8 V for PEC operation under shadowed (low light) and concentrated solar concentration. It is to be noted that under low light condition the amount of hydrogen produced is less compared to the one produced under concentrated light.

Figure 6.16 shows the current generation for the PEC reactor for an applied voltage of 2.0 V for the concentrated and low light case. It is to be noted that higher current generation is observed under concentrated light compared to low light conditions.

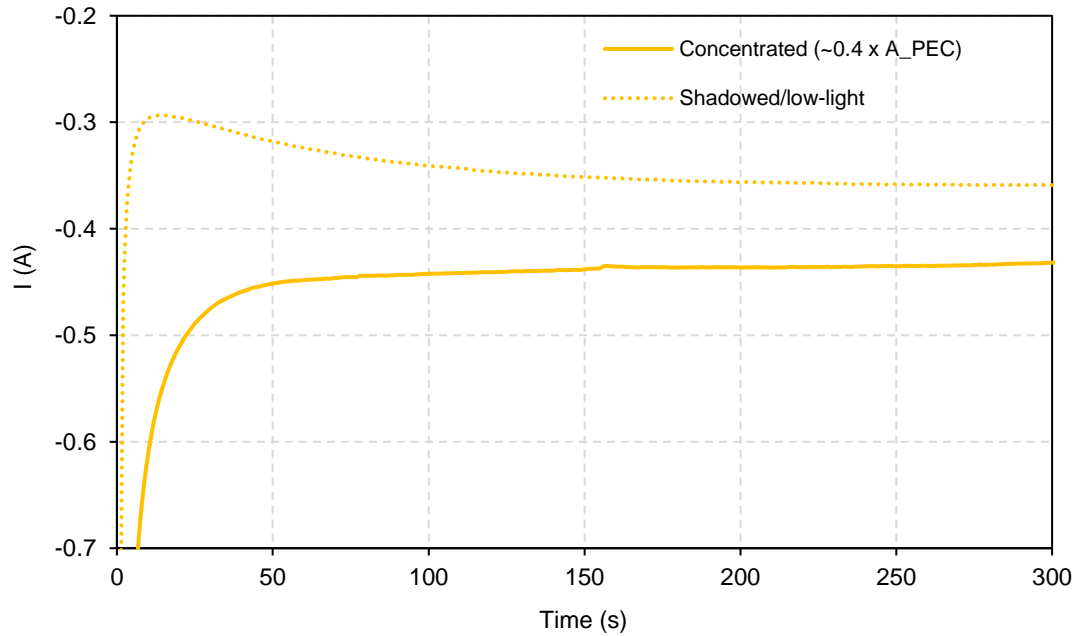


Figure 6.16: Measured current at 2.0 V for PEC operation under shadowed (low light) and concentrated solar concentration.

Figure 6.17 shows measured H_2 production at 2.0 V for PEC operation under shadowed (low light) and concentrated solar concentration. It is seen that as the time increases, the H_2 production for the both the cases start increases and then approaches an almost constant value.

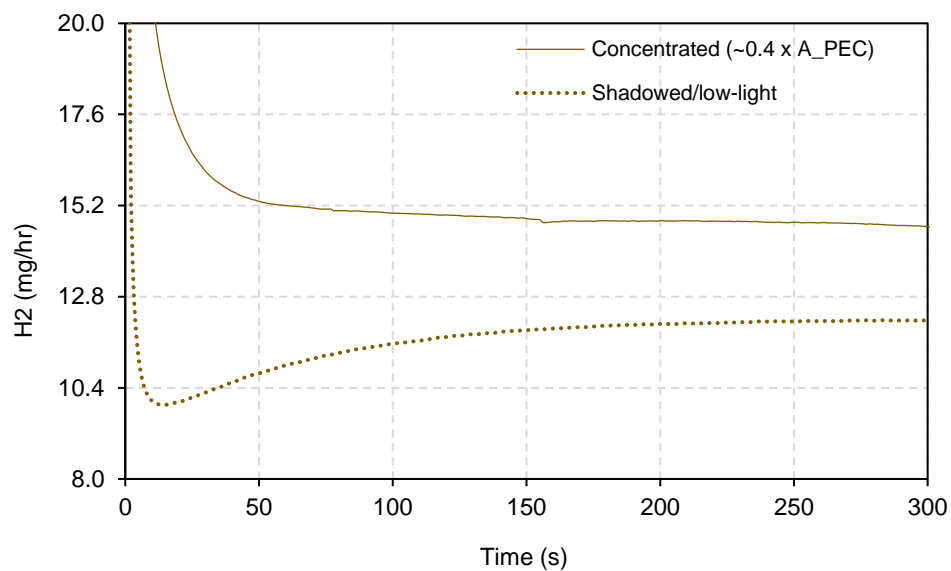


Figure 6.17: Measured H₂ production at 2.0 V for PEC operation under shadowed (low light) and concentrated solar concentration.

Figure 6.18 and Figure 6.19 shows measured current and measured hydrogen production at 3.0 V for PEC operation under shadowed (low light) and concentrated solar concentration, respectively.

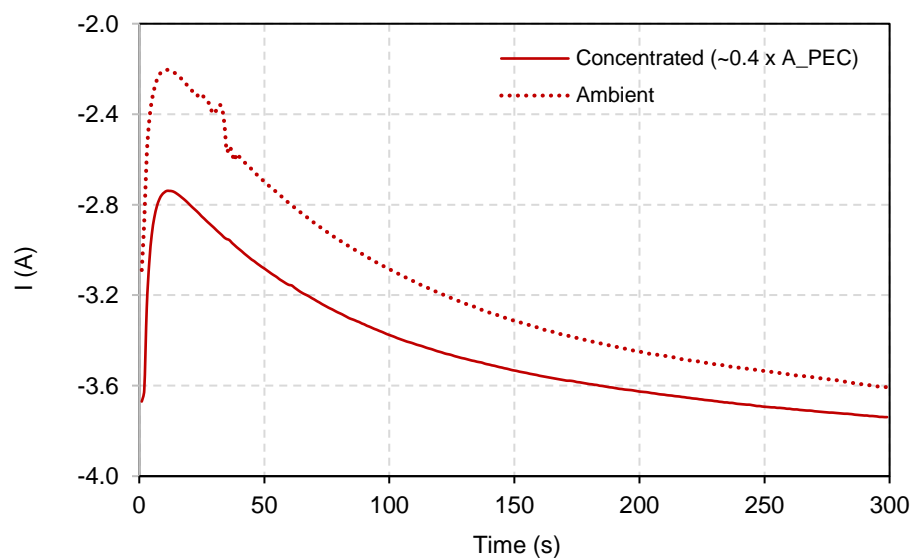


Figure 6.18: Measured current at 3.0 V for PEC operation under shadowed (low light) and concentrated solar concentration.

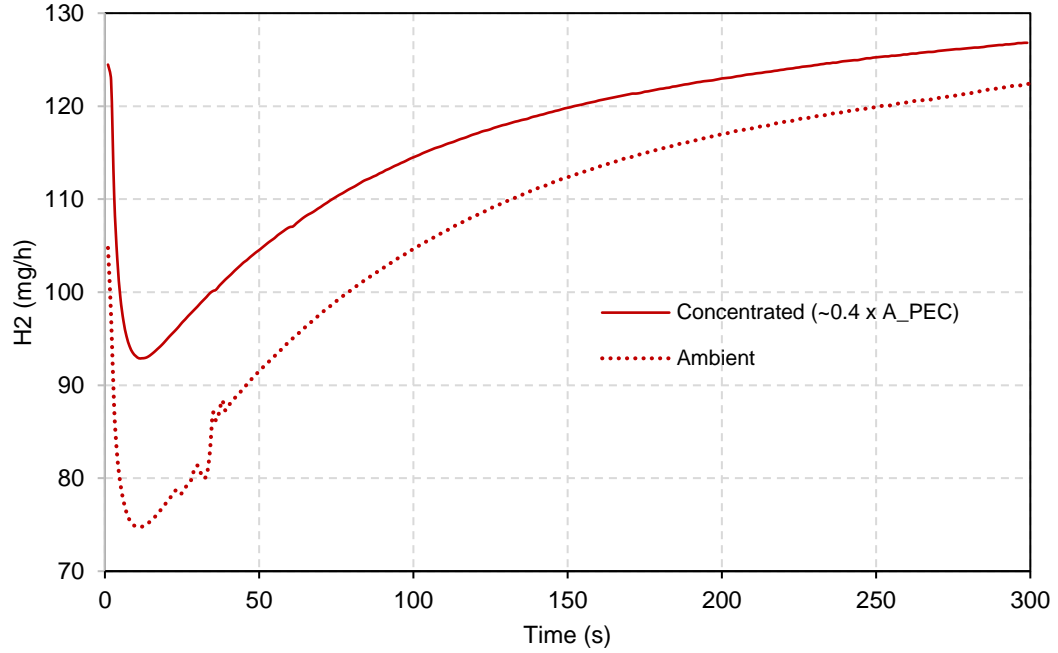


Figure 6.19: Measured H₂ production at 3.0 V for PEC operation under shadowed (low light) and concentrated solar concentration.

Experimental PV Electricity Generation

Figure 6.20 shows the experimental results in terms of I-V and P-V curves of the first case considered for the case when the PV module is under the ambient sunlight, where the maximum power is indicated on the graph and the corresponding voltage and current.

Figure 6.21 shows the variation of the I-V and P-V values obtained from the experiment where the PV module was subjected to concentrated sunlight. Figure 6.22 shows the case for the module under concentrated sunlight with spectrum-splitting, with only wavelengths 800 nm to 1200 nm transmitted to the PV.

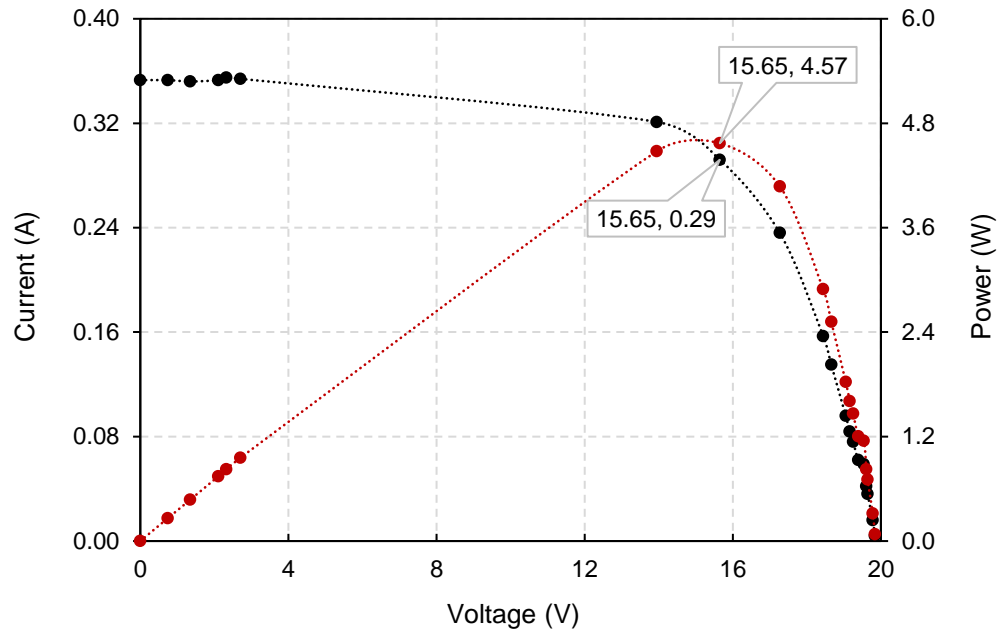


Figure 6.20: Experimental I-V and P-V curves for PV module under ambient sunlight.

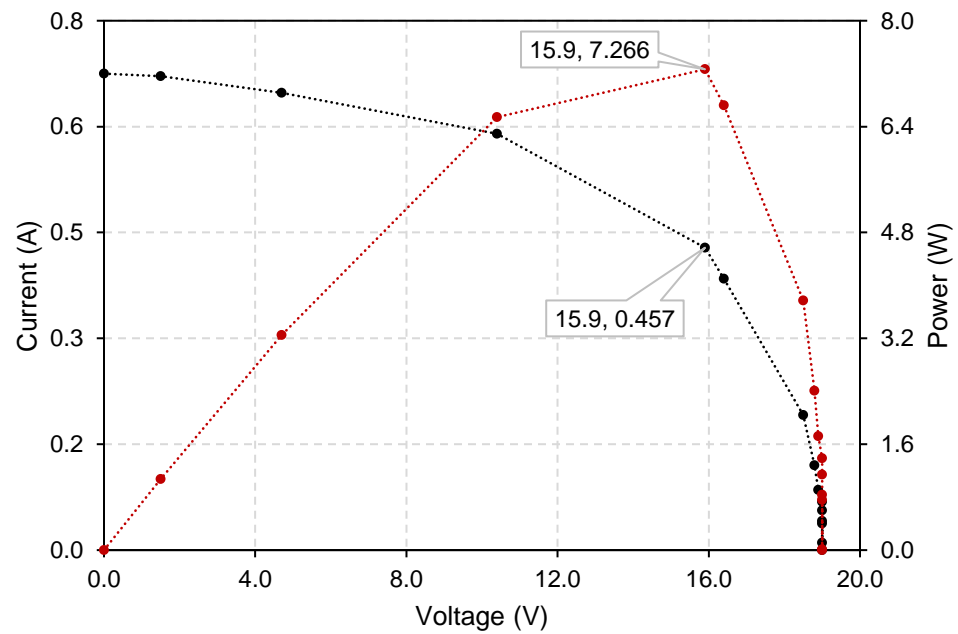


Figure 6.21: Experimental I-V and P-V curves for PV module under concentrated sunlight.

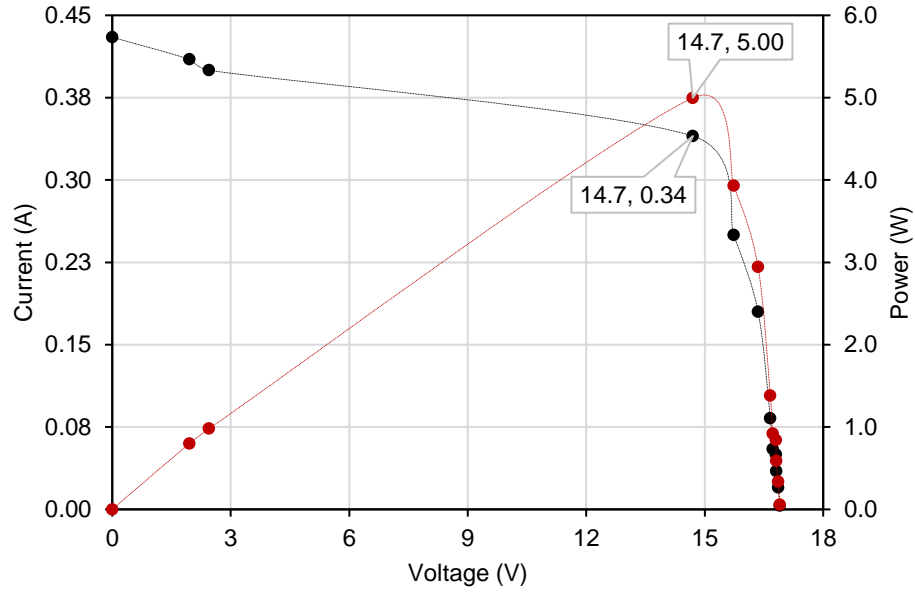


Figure 6.22: Experimental I-V and P-V curves for PV module under concentrated sunlight with spectrum-splitting.

Table 6.3 summarizes the results for the three different sunlight scenarios for experimental PV electricity generation including the energy and exergy efficiency. Although the highest efficiencies are achieved under concentrated full-spectrum sunlight, it is promising to observe the increase in efficiency between ambient full-spectrum sunlight and concentrated spectrum splitting cases. With effective wavelength splitting it is possible to take advantage of the photoactive properties of different PV and PEC technologies for more efficient solar energy capture.

Table 6.3: PV electricity generation and efficiencies for the experimental cases.

Case	Maximum Power (W)	I_{mp} (A)	V_{mp} (V)	Energy efficiency (%)	Exergy efficiency (%)
Ambient sunlight	4.57 ± 0.115	0.27 ± 0.004	15.65 ± 0.336	6.53 ± 0.407	6.92 ± 0.431
Concentrated sunlight	7.27 ± 0.183	0.457 ± 0.006	15.9 ± 0.342	10.4 ± 0.648	11 ± 0.686
Concentrated sunlight with spectrum-splitting	5.0 ± 0.126	0.34 ± 0.0045	14.7 ± 0.316	7.14 ± 0.445	7.58 ± 0.472

6.2.3 Integrated CPV-PEC Performance

Electrolyser Modeling Results

The PEC reactor operates as a PEM electrolyser when no light is present on the surface of the photocathode. Modeling of the PEM operation gives a performance baseline for the integrated PEC when H₂ production is via electricity input only (i.e. no light on the photocathode).

The overpotentials are determined according to the equations given in Chapter 5, and modeled at a nominal current density of 100 mA/cm², or for a range from 20 mA/m² – 100 mA/m² to reflect the operating conditions of electricity supply from the PV module. The properties of the membrane are given in Table 3.1 according to the manufacturer data provided by [51]. Ohmic overpotential represents the resistance by the membrane to the passage of ions across it. Figure 6.23 shows the effect of temperature on the membrane conductivity and resistivity with temperature.

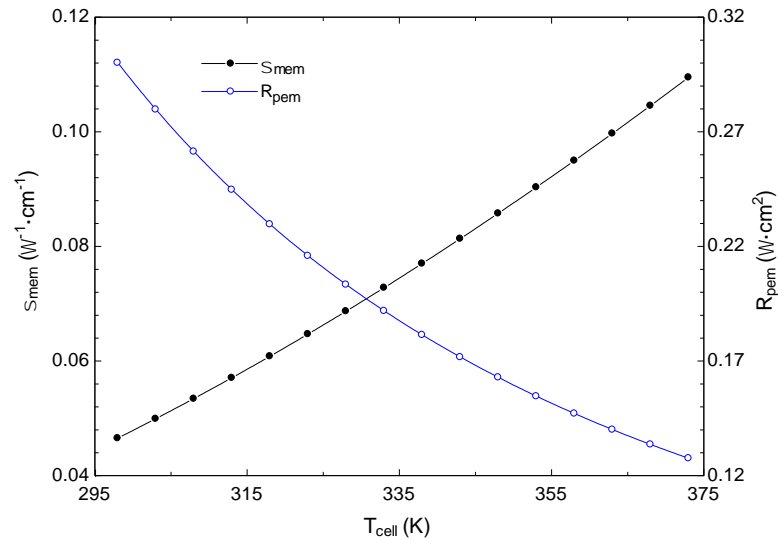


Figure 6.23: Variation of membrane conductivity (σ) and resistivity (R) with operating temperature at $J = 100 \text{ mA/cm}^2$.

As temperature increases, the membrane becomes more conductive, allowing ions to pass more easily across the membrane (resistivity decreases). The effect of increasing temperature for all overpotentials considered in the model is shown in Figure 6.24, demonstrating the tendency for all voltage drops to reduce with increasing operating temperature of the PEM electrolyser. Although this trend does continue as temperature increases further, the range is limited to a maximum operating temperature of 353 K (80 °C) to avoid water vapour formation in the electrolyser compartments.

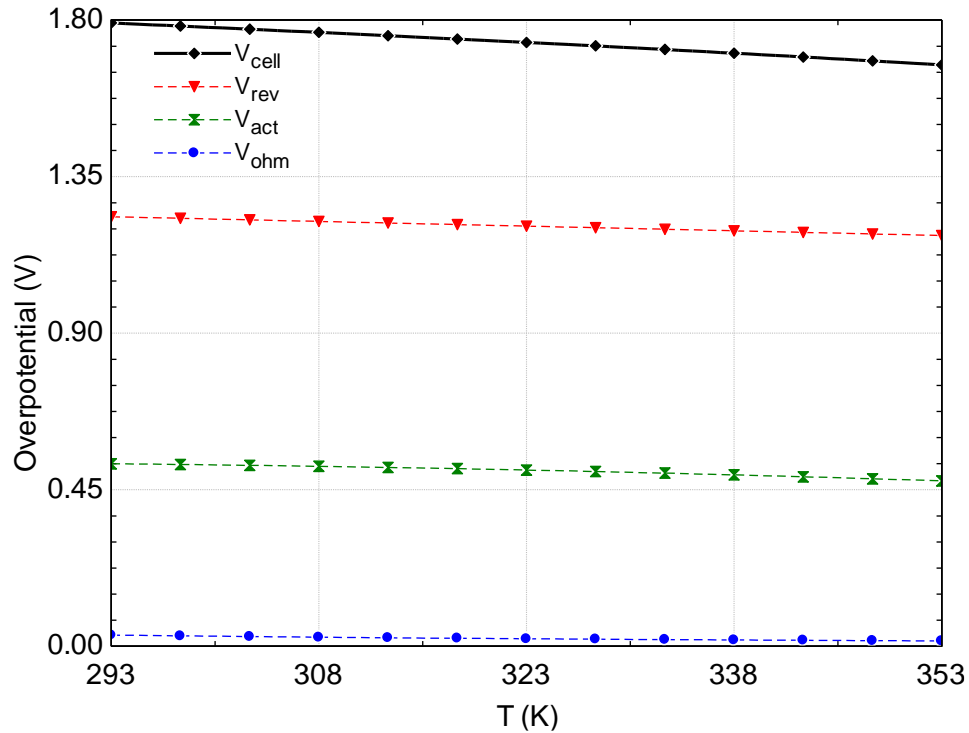


Figure 6.24: Variation of modeled cell overpotentials with operating temperature for PEM electrolysis ($J=100 \text{ mA/cm}^2$).

The effect of current density on the overpotential values of shown in Figure 6.25. While the values do increase, the increase is not significant, with the cell potential remaining between 1.7 V and 1.8 V over the current density range for this case.

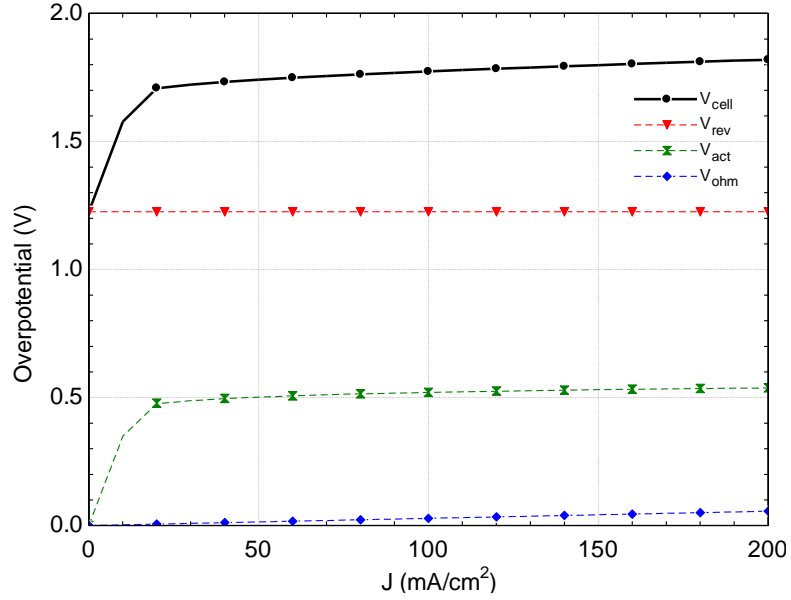


Figure 6.25: Variation of cell overpotentials with current density for PEM electrolysis model (T=303 K, P=1 atm).

Figure 6.26 shows the variation of work input and exergy destruction for PEM electrolysis with the current density. As the current density increases, both the work input and exergy destruction of the electrolyser increase. This trend is attributed to the increase in voltage losses at higher current density, resulting in higher power input.

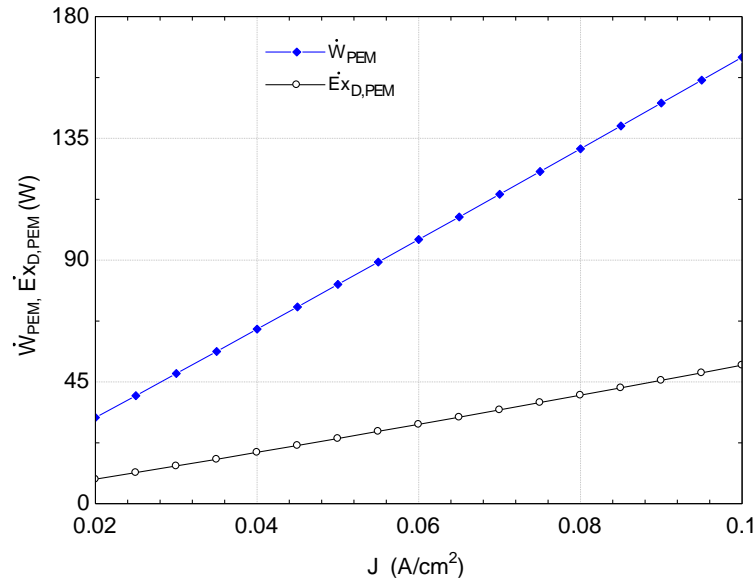


Figure 6.26: Effect of current density on work input and exergy destruction for PEM electrolysis.

Figure 6.27 shows the effect of operating temperature on energy and exergy efficiencies of the PEM electrolyser. It should be noted that as the temperature increases, both efficiencies increase. Membrane conductivity increases with temperature, reducing the voltage drop due to Ohmic losses.

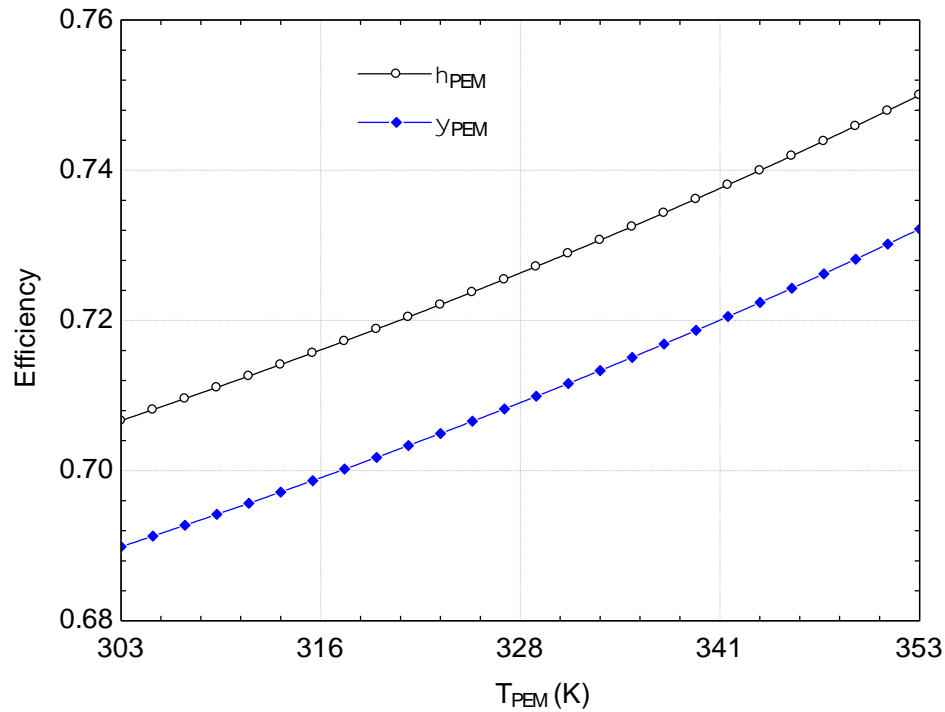


Figure 6.27: Effect of operating temperature on PEM energy and exergy efficiencies ($J=100 \text{ mA/cm}^2$).

As shown in Figure 6.28, energy and exergy efficiencies decrease with the increase in current density. The exergy efficiency decreases due to the increase in the voltage losses highlighted earlier, which translate to higher exergy destruction rate. The voltage losses also contribute to the decrease of the energy efficiency.

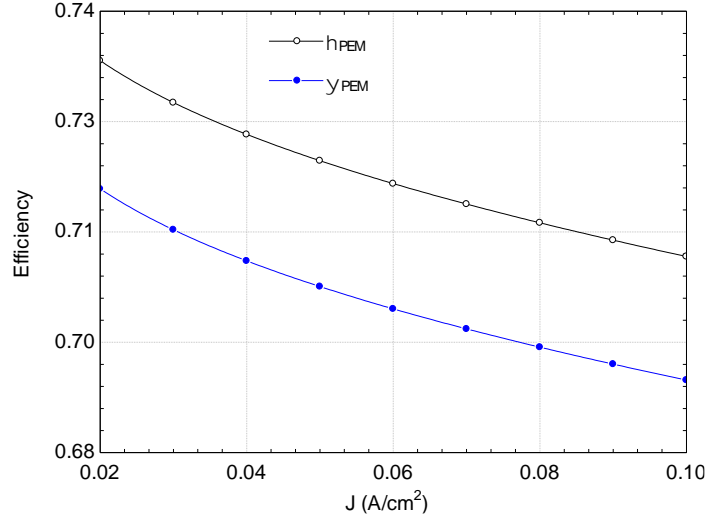


Figure 6.28: Variation of PEM energy (η) and exergy (ψ) efficiencies with current density ($V=2$ V).

Integrated CPV-PEC Modeling Results

The ambient solar and location details for the integrated CPV-PEC model are detailed in Direct beam radiation is concentrated onto the dielectric mirror focal area, which then reflects and transmits sunlight onto the PEC photocathode and PV module surfaces, respectively. Table 6.4 lists the component surface areas, as well as the geometric concentration ratio of the dielectric mirror receiver with respect to the lens.

Although the mirror is not a collimating lens, the initial assumption is made that no further concentration of light occurs between the mirror-PV and mirror-PEC surfaces for the estimation of maximum energy input to each component. Given the close values of the mirror and PV areas, this assumption is valid for the case with full illumination of the PV. To account for this assumption in the PEC energy input model, a concentrated area fraction of 0.4 applies to the PEC illuminated surface area, and the remaining surface area illumination applies diffuse solar irradiance. This factor is chosen by observation of the photoactive area of the Cu_2O coated cathode that receives concentration during the experiments, and the associated surface area.

Table 6.4: CPV-PEC component energy and exergy input.

Component	Fresnel lens, A_1	Dielectric Mirror, A_2	PEC ^a , A_3	PV, A_4
Component Surface area, m^2	0.867	0.075	0.144	0.058
Illuminated surface area, m^2	0.867	0.070	0.072	0.046
Maximum concentration ratio, CR_{max}	--	12	1	1

a. Total photocathode surface area is 0.082 m^2

The total energy and exergy input to each component is shown in Figure 6.29. From these values, the modeled efficiencies are determined for the components and overall system.

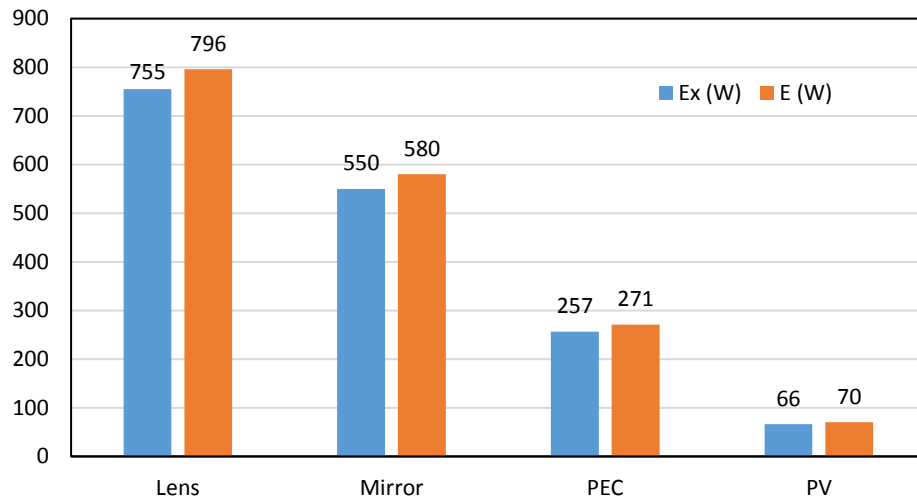


Figure 6.29: Energy and exergy inputs to each component of the CPV-PEC.

6.2.5 CPV-PEC Exergoeconomic Results

For comparison to current methods of hydrogen production, it is necessary to determine the exergetic cost of hydrogen production by the CPV-PEC system. The cost breakdown for the PEC reactor is listed in Table 6.5. The dominant cost is due to the proton exchange membrane, which amounts to approximately half of the reactor total cost.

The cost of the integrated CPV-PEC apparatus is given in Table 6.6. For the present case. The lens is salvaged from a rear-projection television at no cost, however commercially available Fresnel lenses of comparable size are available at prices ranging from \$50 - \$100, and lab grade lenses can exceed \$1000 depending on the material grade and application. It is considered more sustainable to use the approach taken in this study when available – the salvaged lens is capable of greater than 10x solar concentration and utilizes materials in a sustainable manner (i.e. – does not require manufacture from new raw materials).

Table 6.5: Capital cost of PEC Reactor.

Item	Material	Qty.	Unit Price (\$)	Total Price (\$)
Proton exchange membrane	Nafion	1	2000.00	2000.00
Electrodes	Stainless steel	2	200.00	400.00
Electrodeposition chemicals	Lactic acid, CuSO ₄	3	150.00	450.00
Reactor casing	HDPE	2	130.00	260.00
Reactor window	Acrylic sheet	1	100.00	100.00
Gaskets	Nitrile rubber	6	10.00	60.00
Tubing	Plastic	4	25.00	100.00
Fasteners/hardware	Steel/Stainless steel	-	50.00	50.00
Other (Adhesives, silicon sealant, etc.)	-	-	120.00	120.00
Machining	-	-	450.00	450.00
TOTAL				\$3,990.00

Based on these system costs, the exergoeconomic factor of the CPV-PEC is plotted under various interest-rate scenarios in Figure 6.30. Increasing the lifetime of the system significantly decreases the exergoeconomic factor. Membrane lifetime and cost have a

significant effect on the system total cost and have a relatively short lifetime, however this may change as these technologies are continuing to develop and improve

Table 6.6: Capital cost of integrated CPV-PEC.

Item	Component Capital Cost (\$)
PEC Reactor	\$3,990.00
Dielectric Mirror Array	\$1,200.00
PV Module	\$150.00
Concentrator structural materials and hardware	\$200.00
TOTAL	\$5,540.00

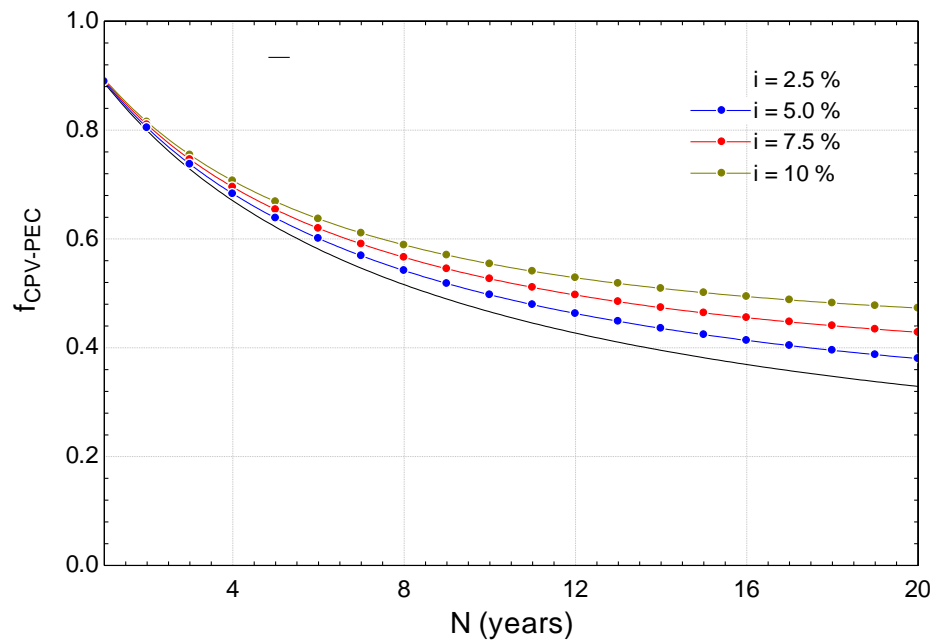


Figure 6.30: Exergoeconomic factor of integrated CPV-PEC reactor for different interest rate scenarios.

6.2.6 CPV-PEC Optimization

By using the generated data through the parametric studies done the developed model on EES are used to produce the objective function in Matlab. The main parameters that are use to produce the objective function in neural network are provided in Table 6.7.

Table 6.7: Parameters used to generate the objective function through neural network.

Parameter	Value (unit)
Number of data points used to generate the objective function	102 x 7 (data points)
Percentage of the data points used for training	70%
Percentage of the data points used for testing	15%
Percentage of the data points used for validating	15%
Selected Training algorithm	Bayesian Regularization

The results of the neural network training are having the training mean square error of 2.23×10^{-3} , the validation mean square error of the validation step had it equal to zero, and finally the means square error for the testing stage is 3.44×10^{-3} .

Three dimensional plots of the developed parametric studies that are generated in the aim of developing the objective function of the optimized system through the neural network are presented in Figure 6.31, Figure 6.32, Figure 6.33 and Figure 6.34 are the power produced by the PV, exergy efficiency of the PV, energy efficiency of the PV, and energy efficiency of the concentrator respectively.

Figure 6.31 shows the variation and the response of the developed system model of EES in terms of the PV power output with the variation of the two considered operating parameters, the ambient temperature and the temperature of the PV. Figure 6.31 shows that the system has its maximum at one of the edges of the considered operating ranges.

The second parametric study considers the exergy efficiency of the PV, where the variation of the exergy efficiency of the PV with the main selected operating parameters are presented in Figure 6.32. Figure 6.32 shows that the exergy efficiency of the PV experienced a different behavior than that of the PV power production at a constant solar irradiance.

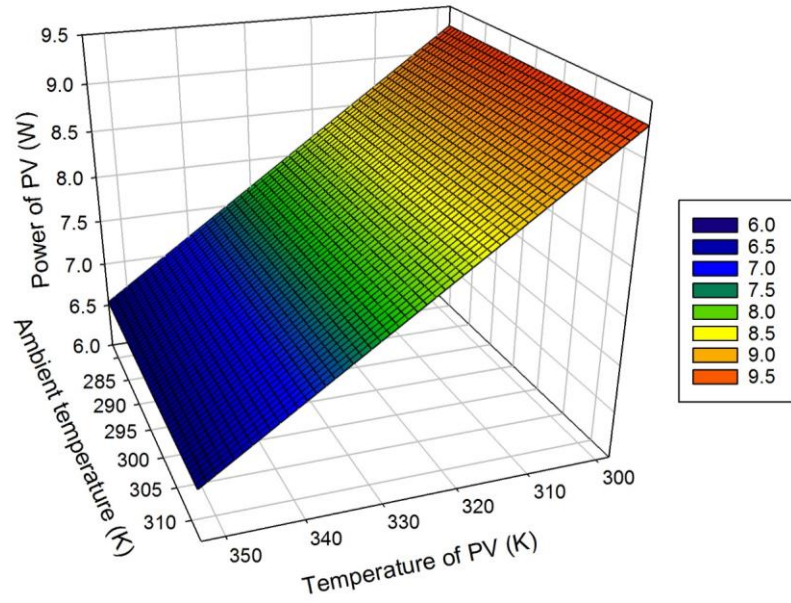


Figure 6.31: Considered parameters and the corresponding PV power output used to train the neural network in generating the objective function.

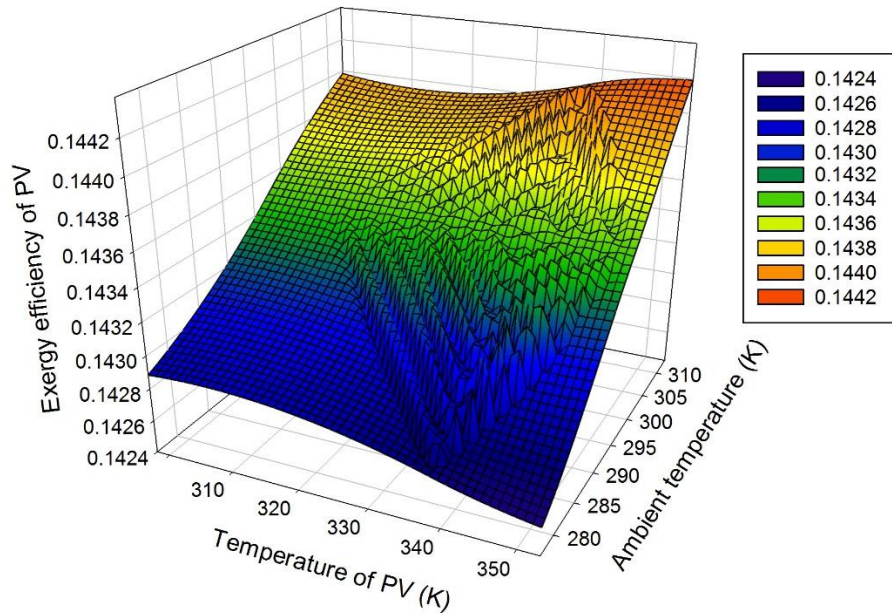


Figure 6.32: Considered parameters and the corresponding exergy efficiency of the PV used to train the neural network in generating the objective function.

Although the exergy efficiency of the PV had a different behavior than that of the PV power output, however the exergy efficiency had similar location of its maximum value. The remaining two outputs are the energy efficiencies of the PV and the solar concentrator, which are presented in Figures 6.33 and 6.34.

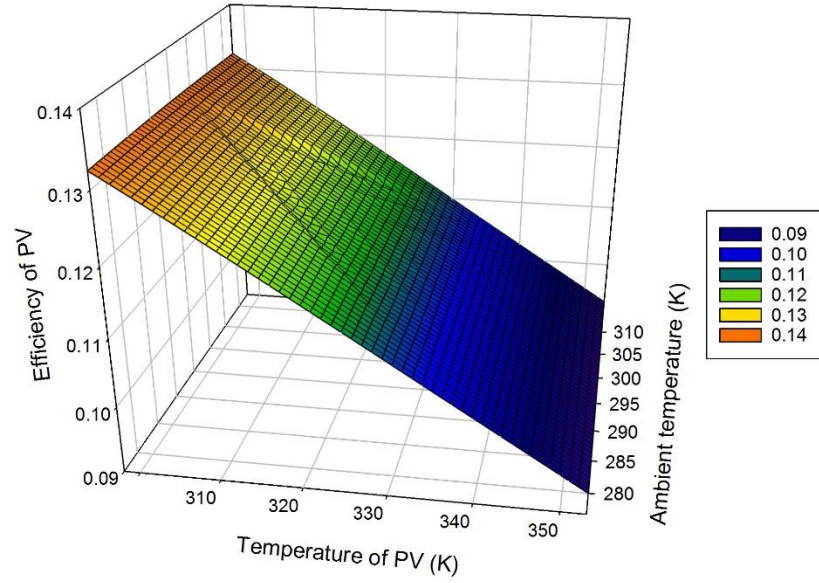


Figure 6.33: Considered parameters and the corresponding energy efficiency of the PV used to train the neural network in generating the objective function.

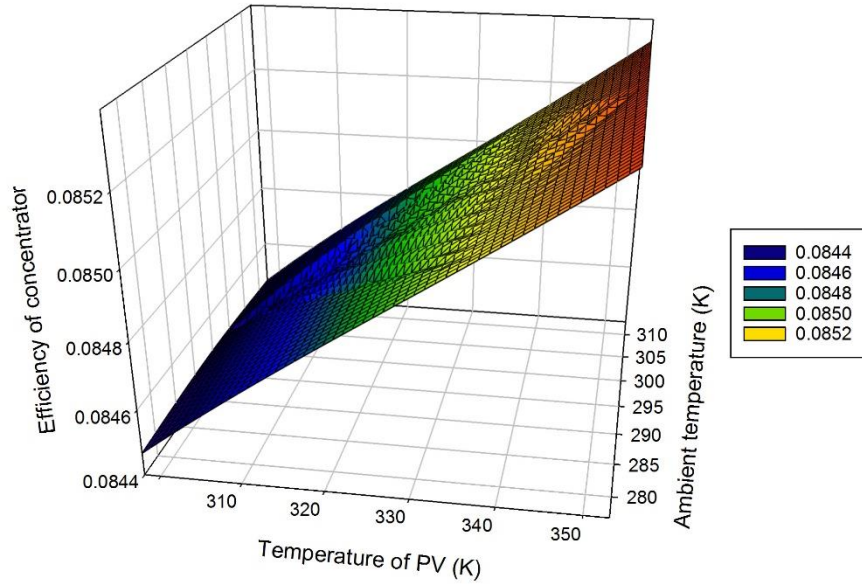


Figure 6.34: Considered parameters and the corresponding energy efficiency of the concentrator used to train the neural network in generating the objective function.

The error histogram of the generated objective function is presented in **Error! Reference source not found.** It is shown that maximum errors from both side of having larger or smaller than the correct value are 0.24 and -0.15 respectively.

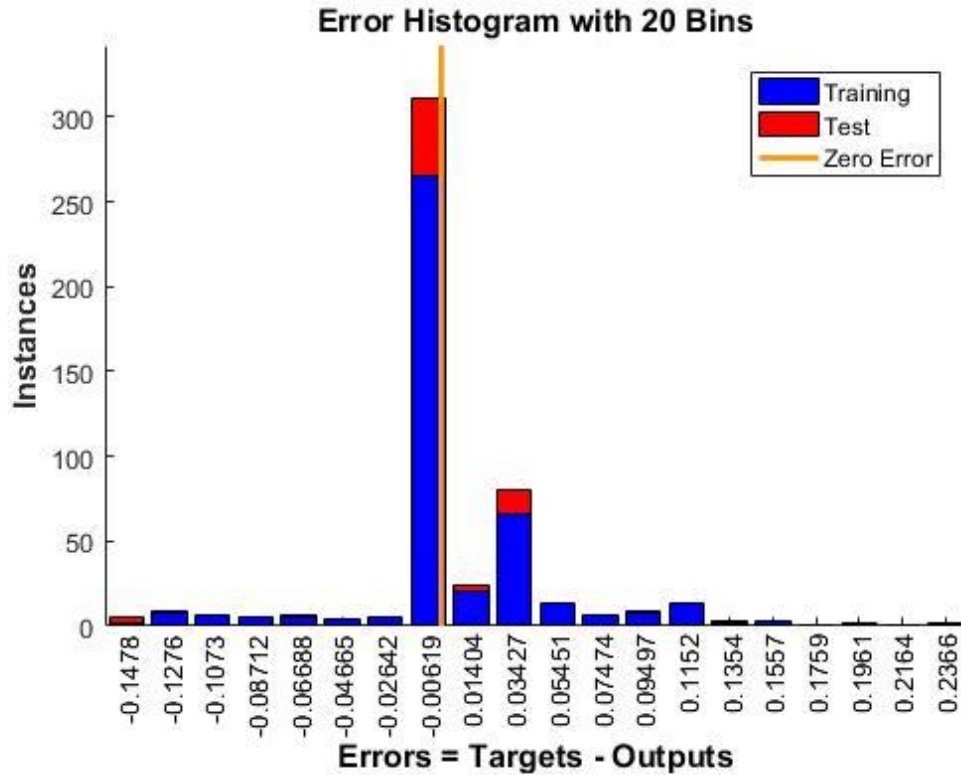


Figure 6.35: Error histogram of the trained, validated and tested objective function of the proposed system.

The training performance of the neural network through the iterations are shown in Figure 6.36. The regression plots of the generated models against the supplied data are shown Figure 6.37. Figure 6.37 shows that the model is had a high agreement with the supplied data and due to that it is used to optimize the system using the genetic algorithm.

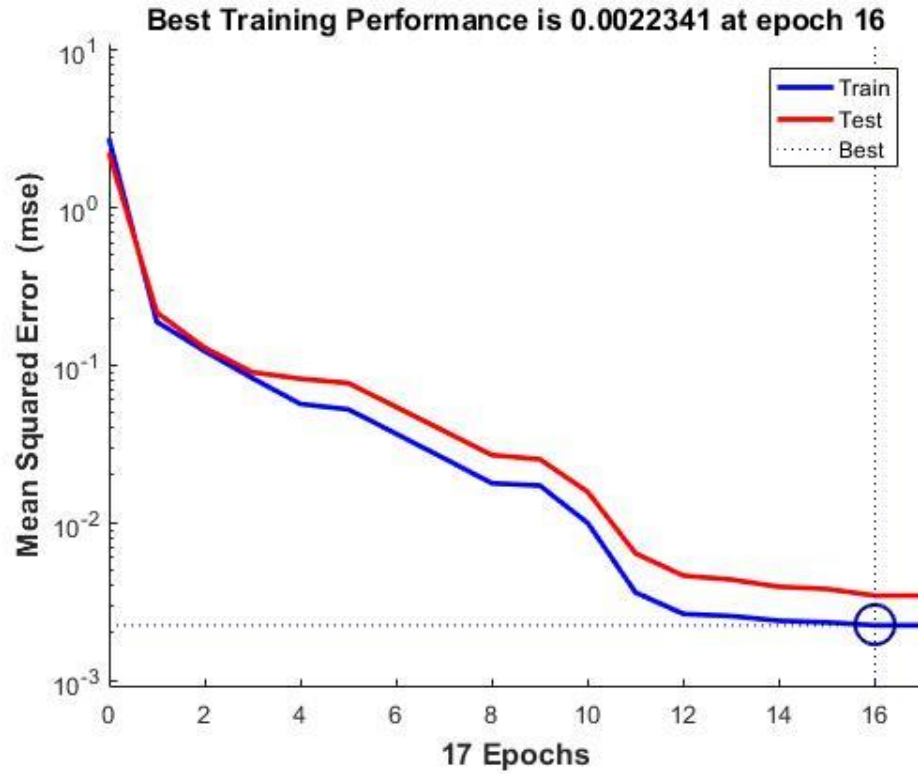


Figure 6.36: Performance of the model with the iterations through the training of the objective function.

The results of the multi-objective optimization are presented in Table 6.8. Note that the genetic algorithm resulted in a single Pareto point, which reflect that the system had a one point that presented all the global optima the system can have.

Table 6.8: The results of the multi-objective optimization.

Parameter	Value (unit)
Power produced by the PV	9.87 W
Exergy efficiency of the PV	31.7%
Energy efficiency of the PV	8.5%
Energy efficient of the concentrator	0.19 %

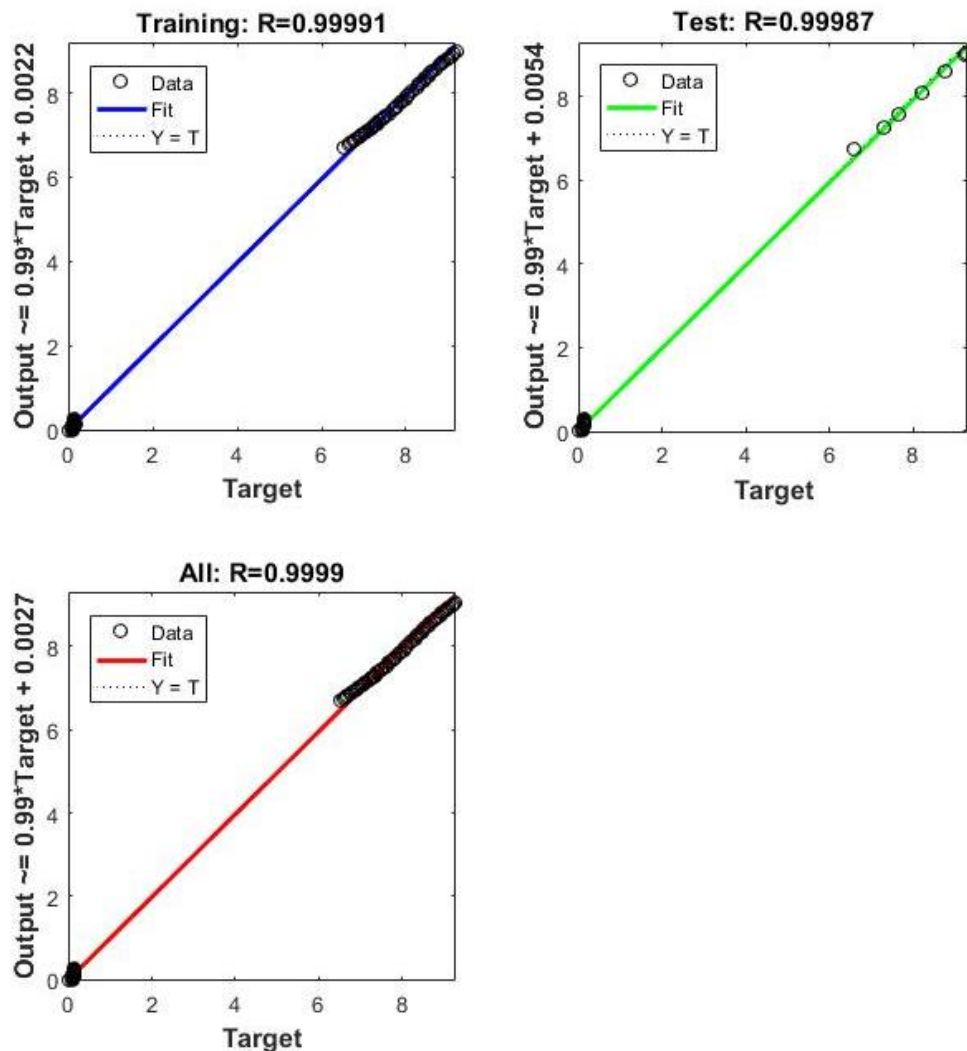


Figure 6.37: Regression plots of the generated models against the supplied data

6.3 Integrated System Results

The system assessment results to produce liquid methanol fuel in a CO₂ hydrogenation plant are given for two integrated system case studies, which differ according to the supply of the H₂ and CO₂ inputs for the methanol synthesis process. Integrated System I utilizes H₂ produced by CPV-PEC, and CO₂ from seawater extracted via bipolar membrane electrodialysis. Integrated System II case study assesses a conceptual multigeneration system integrating an offshore concentrator photovoltaic (CPV) array with simultaneous H₂ and CO₂ extraction from seawater.

6.3.1 Aspen Plus Results for Methanol Synthesis Plant

The layout of the CO₂ hydrogenation plant is shown in Figure 6.38, and the state point properties are provided in Table 6.9. These are used as the basis for the integrated system case studies. Table 6.10 summarizes the work and heat duties for the methanol synthesis process from the Aspen Plus model results in terms of kWh/kmol-H₂ input. Internal heat recovery of the feed compressor intercooling process to the gases entering the synthesis reactor improve performance during steady state operation and avoid the requirement of additional heat input.

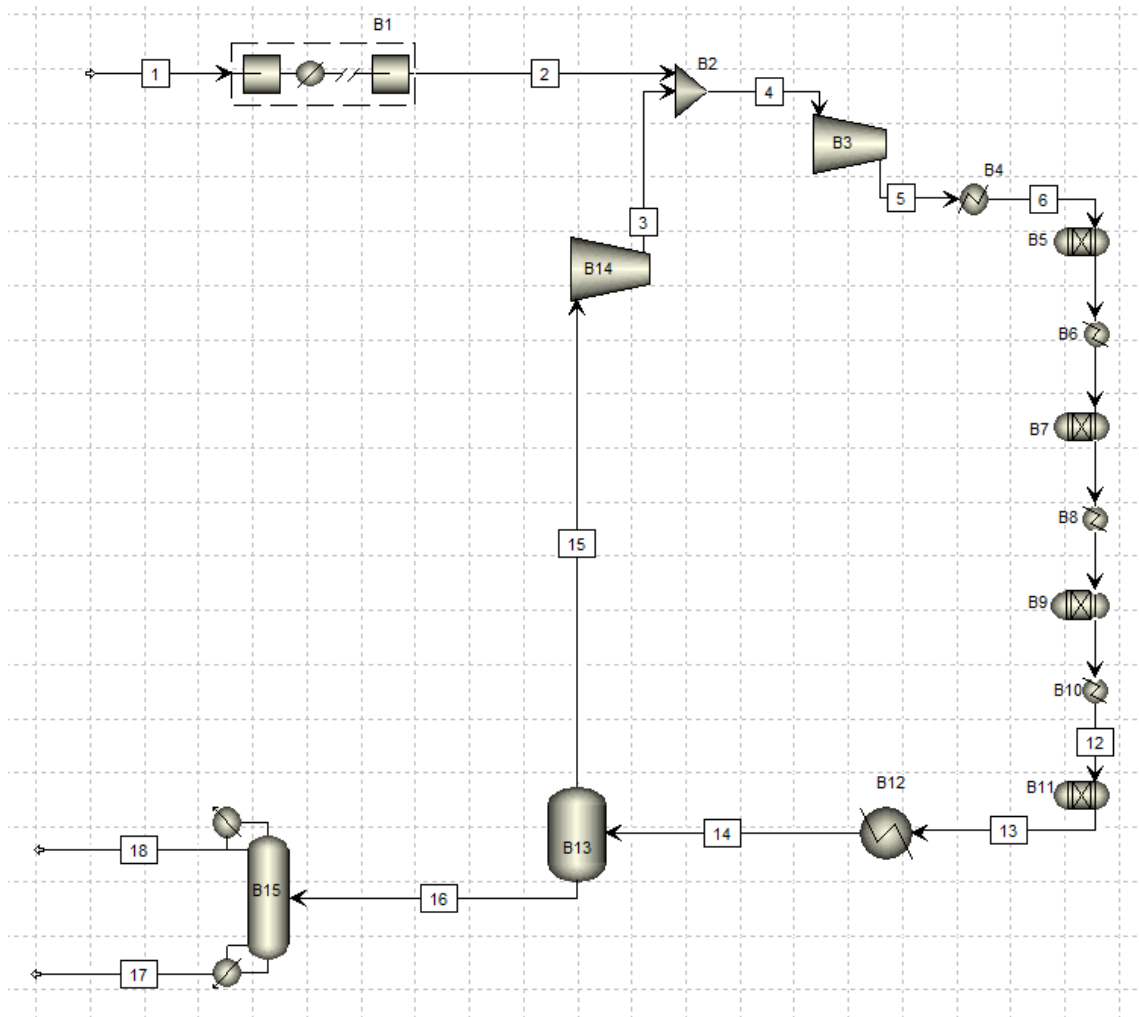


Figure 6.38 Aspen Plus flowsheet of methanol synthesis plant.

Table 6.9: State points for Aspen Plus methanol plant.

[i]	Phase	T (K)	P (MPa)	\dot{n} (kmol/hr)	\dot{m} (kg/s)	\dot{V} (lpm)	\dot{E}_x (kW)	ex_i (kJ/kg)	\overline{ex}_i (kJ/kmol)
1	g	300.0	0.10	4.00	1.4E-02	1641.45	0.00	0.01	0.18
2	g	323.0	3.00	4.00	1.4E-02	60.22	9.38	674.81	8444.7
3	g	448.4	3.00	14.30	3.0E-02	300.33	37.61	1267.99	9470.1
4	g	423.8	3.00	18.30	4.4E-02	362.95	46.16	1059.57	9082.2
5	g	507.9	5.00	18.30	4.4E-02	262.85	57.66	1323.55	11345.1
6	g	493.0	4.95	18.30	4.4E-02	257.75	56.54	1297.82	11124.4
7	g	493.0	4.95	16.25	4.4E-02	227.78	50.75	1164.96	11247.2
8	g	493.0	4.90	16.25	4.4E-02	230.07	50.64	1162.33	11221.8
9	g	493.0	4.90	16.26	4.4E-02	230.35	50.68	1163.40	11219.4
10	g	493.0	4.85	16.26	4.4E-02	232.68	50.57	1160.74	11193.7
11	g	493.0	4.85	16.28	4.4E-02	232.97	50.62	1161.81	11191.3
12	g	493.0	4.80	16.28	4.4E-02	235.35	50.50	1159.12	11165.4
13	g	493.0	4.80	16.30	4.4E-02	235.64	50.55	1160.20	11162.9
14	g,ℓ	323.0	4.80	16.30	4.4E-02	134.57	38.30	879.07	8458.0
15	g	323.0	1.20	14.30	3.0E-02	536.15	24.50	826.76	6168.1
16	ℓ	323.0	1.20	2.00	1.4E-02	1.02	0.08	5.84	146.4
17	ℓ	457.3	1.10	1.00	5.0E-03	0.37	0.80	159.19	2870.1
18	ℓ	403.7	1.10	1.00	8.9E-03	0.82	0.57	63.59	2038.6

The exergy destruction fractions by each component is shown in Figure 6.39, indicating the dominant sources of loss within the plant – the flash separation process and cooling of the fuel and recycle gas products in HX5 following the four-stage hydrogenation reactors.

Table 6.10: Component work, entropy generation, and exergy destructions for 1 kmol/hr CH₃OH production.

Tag	Component	Electrical Work Input, \dot{W} (kW)	Entropy Generation, \dot{S}_{gen} (kW/K)	Exergy Destruction ^a , \dot{E}_{XD} (kW)
B1	Feed Compressor, CF ^b	16.01	21.9×10^{-3}	6.57
B2	Mixing Chamber, MC	-	3.64×10^{-3}	1.09
B3	Compressor, C1	12.95	7.81×10^{-3}	2.34
B4	Heat Exchanger, HX1	-	0.27×10^{-3}	8.14×10^{-2}
B5	Reactor Stage 1	-	4.24×10^{-3}	1.27
B6	Heat Exchanger 2, HX2	-	0.38×10^{-3}	0.11
B7	Reactor Stage 2	-	0.69×10^{-3}	0.21
B8	Heat Exchanger 3, HX3	-	0.39×10^{-3}	0.12
B9	Reactor Stage 3	-	0.69×10^{-3}	0.21
B10	Heat Exchanger 4, HX4	-	0.39×10^{-3}	0.12
B11	Reactor Stage 4	-	0.69×10^{-3}	0.21
B12	Heat Exchanger 5, HX5	-	22.98×10^{-3}	6.89
B13	Flash Separation, FS	-	46.56×10^{-3}	13.97
B14	Compressor, C2	14.52	10.06×10^{-3}	3.02
B15	Distillate Separation, DS	-	13.62×10^{-3}	4.09
TOTAL		43.48	11.75×10^{-2}	35.24

Note: (a) Component exergy destruction calculated using $\dot{E}_{\text{XD}} = T_o \times \dot{S}_{\text{gen}}$,
(b) $\dot{S}_{\text{gen,CF}}$ includes 15.3 kW intercooling.

The CO_{2e} balance for each component is shown in Figure 6.40. Reactor component B5 consumes the majority of CO₂ in the reverse water-gas shift to produce syngas for final conversion to methanol in the remaining stages.

Figure 6.41 shows the exergoeconomic factor of methanol synthesis plant for different interest rates with the increase in number of year. As the year increases, the exergoeconomic factor decreases while it increases with the increase in interest rate.

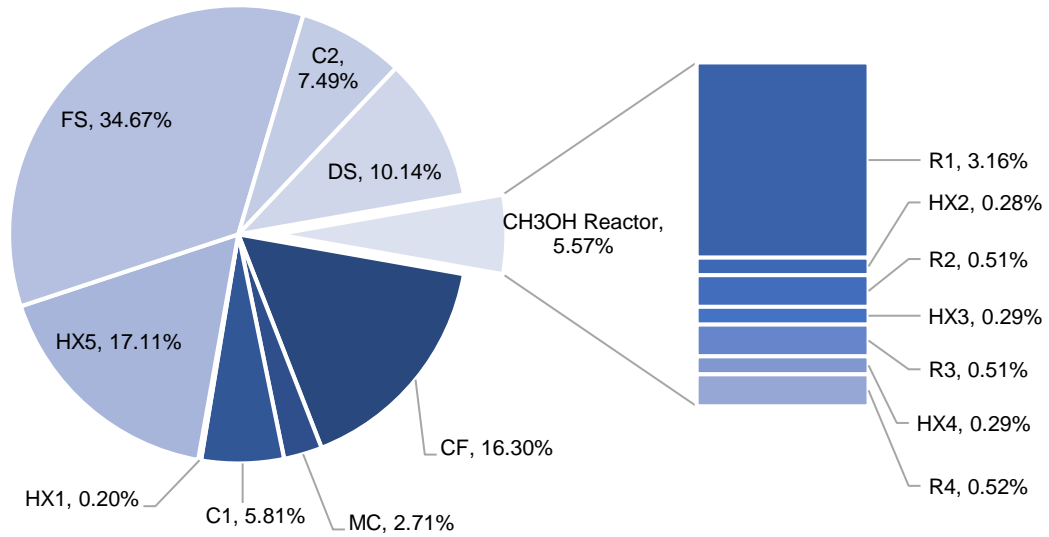


Figure 6.39: Exergy destruction fraction of methanol plant components

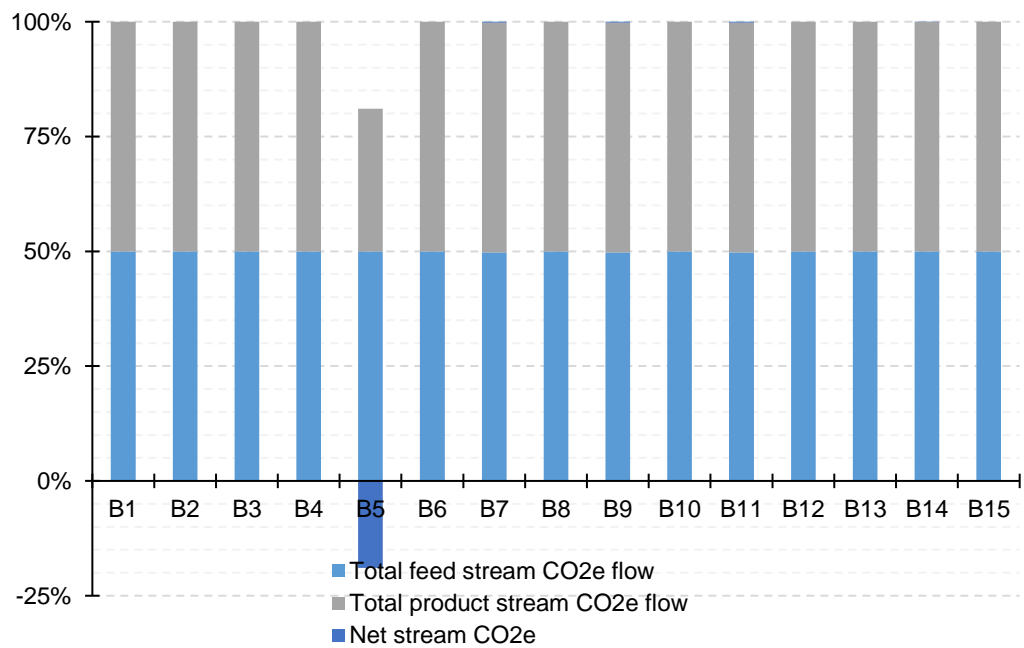


Figure 6.40: CO_{2e} balance of methanol plant components.

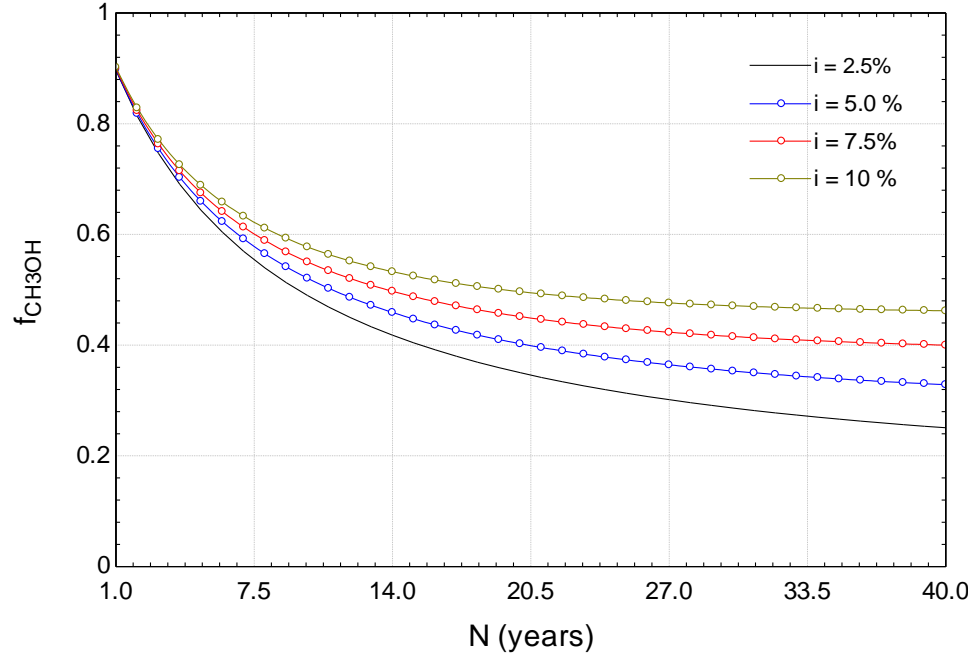


Figure 6.41: Exergoeconomic factor of methanol synthesis plant for different interest rate scenarios.

6.3.3 System I Case Study Results

System I integrates the CPV-PEC reactor with SRWO freshwater production and BPMED carbon capture to supply H_2 and CO_2 . The energy and exergy analyses of the integrated is found to be 7.1% and 7.0%, respectively. Figure 6.42 shows the variation of energy and exergy efficiencies of the integrated system with the solar irradiation. It is found that as the irradiation changes from 400 W/m^2 to 800 W/m^2 , the value of energy efficiency decreases from 7.4% to 7.0% while the exergy efficiency reduces from 7.3% to 7.9%.

The effect of area of the collector on the energy and exergy efficiencies of the overall integrated system is shown in Figure 6.43. It is to be noted that as the area changes from 4400 m^2 to 5200 m^2 , both the energy and exergy efficiencies decreases. This is attributed to the fact that with the increase in the area of the collector, the mass flow rate of methanol does not vary as it is keep constant in the analysis.

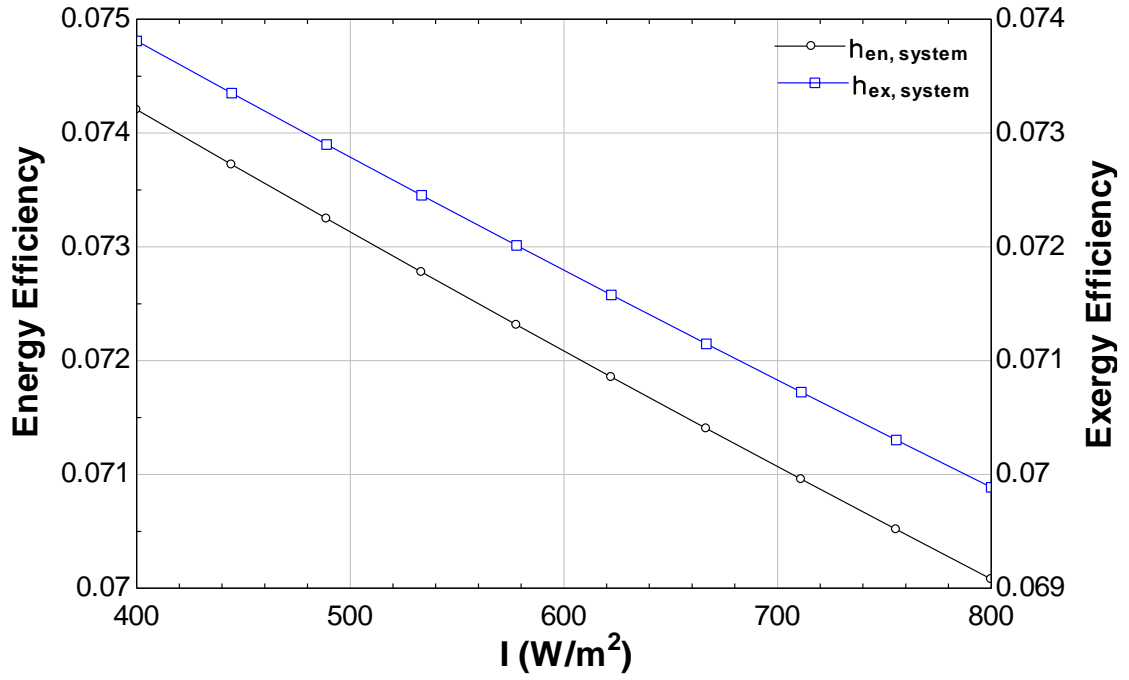


Figure 6.42: Variation of energy and exergy efficiencies of the integrated system with the solar irradiation.

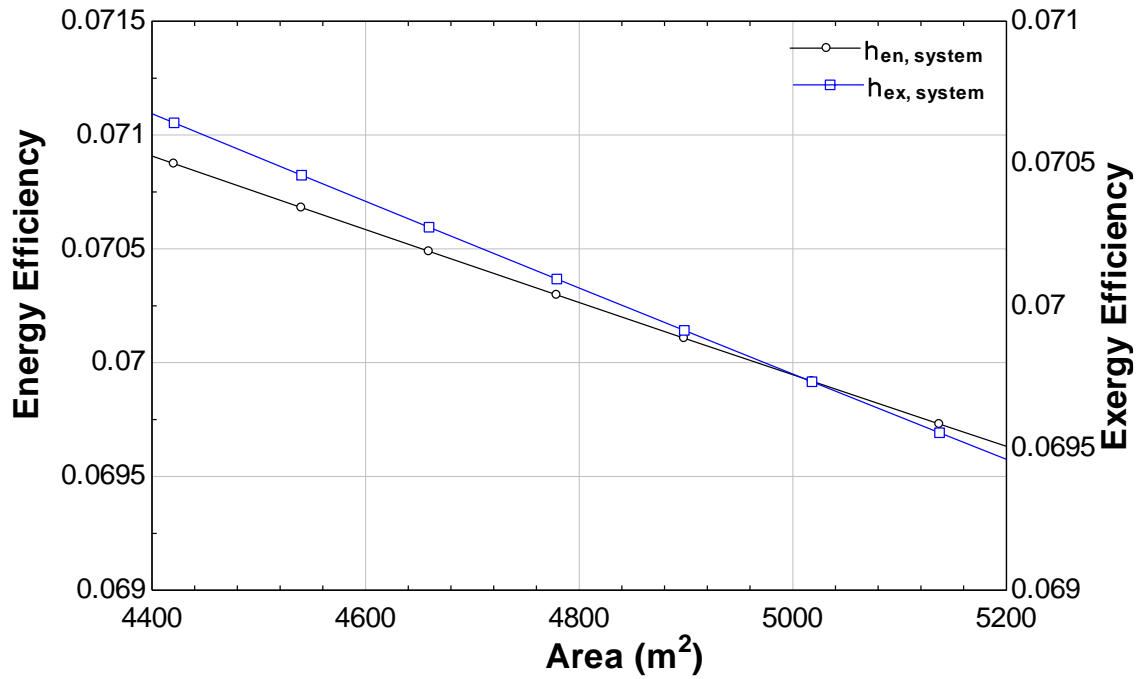


Figure 6.43: Effect of area of the collector on the energy and exergy efficiencies of the integrated system.

6.3.4 System II Case Study Results

System II case study assesses the thermodynamic performance of a conceptual multigeneration system, shown schematically in Figure 4.5, proposed by [90] and investigated in [91], integrating an offshore concentrator photovoltaic (CPV) array with a synthetic methanol plant, including processes to extract H₂ and CO₂ feedstocks from seawater (shown in Figure 4.6), on a floating artificial island. The multigeneration system comprises a linear Fresnel CPV array, CO₂-hydrogenation methanol reactor (shown schematically in Figure 4.2), reverse osmosis seawater desalination, and electrolytic cation exchange membrane for simultaneous hydrogen and carbon dioxide extraction.

The baseline performance assessment considers the system under steady state conditions and reference conditions T_o and P_o of 25°C and 101 kPa, respectively. The surface area solar island is taken as the aperture area for the linear Fresnel reflector array, which focuses direct normal radiation at a concentration, $C = 10$ Suns onto PV modules ($\eta_{PV}=30\%$). Solar insolation normal to the collector aperture surface is taken to be 1000 W/m², amounting to an annual value of 2.0 MWh/m²·year.

The assessment also considers large scale operation at 1500 tonnes/year methanol production to determine the power and seawater/water consumption by the SWRO and E-CEM subsystems to supply the CO₂ and H₂ feeds to the methanol reactor. Converting mass values results with the annual molar feed rates of H₂ and CO₂, and H₂O products of

$$1500 \times 10^3 \text{ [kg/year]} / M_{\text{CH}_3\text{OH}} \text{ [kg/kmol]} = 46.8 \times 10^3 \text{ kmol CH}_3\text{OH/year}$$

where the mole ratio for hydrogen and carbon dioxide ($n_{\text{H}_2}/n_{\text{CO}_2}$) is 3:1 for every mole of methanol product. Thus, the stoichiometric feed rates are:

$$3 \left[\frac{\text{kmol H}_2}{\text{kmol CH}_3\text{OH}} \right] \times \left(46.8 \times 10^3 \left[\frac{\text{kmol CH}_3\text{OH}}{\text{year}} \right] \right) = 140.4 \times 10^3 \text{ kmol H}_2/\text{year} \quad (283 \times 10^3 \text{ kg H}_2/\text{year})$$

$$1 \left[\frac{\text{kmol CO}_2}{\text{kmol CH}_3\text{OH}} \right] \times \left(46.8 \times 10^3 \left[\frac{\text{kmol CH}_3\text{OH}}{\text{year}} \right] \right)$$

$$= 46.8 \times 10^3 \text{ kmol CO}_2/\text{year} \quad (2060 \times 10^3 \text{ kg CO}_2/\text{year})$$

Table 6.11 provides details for the specific work requirement by each subsystem process, and the electricity consumption for 1500 tonnes per year methanol production.

Table 6.11: Subsystem energy consumption for System II.

Processes		Methanol Production	
Subsystem	Specific work, w_i	Specific work, w_i [kWh/kg-CH ₃ OH]	Electricity consumption ^a , \dot{W}_{el} , [GWh/year]
E-CEM Reactor	49 kWh/m ³ -H ₂ (STP)	110.9	166
SWRO	3.089 kWh/m ³ -H ₂ O	14.6	22
Methanol Reactor	1.33 kWh/kg-CH ₃ OH	1.33	2.0
TOTAL		126.8	190

a. Annual electricity consumption for 1500 tonne/year methanol production.

Assuming a 98% CO₂ conversion efficiency for the methanol synthesis process, the total feed rate requirement for CO₂ is 2100 tonnes/year. For 90% CO₂ extraction from seawater containing 0.1 kg-CO₂/m³, the E-CEM must process approximately of 28 million cubic metres of seawater annually.

Reference environment conditions are also important considerations for the efficiencies of the system due to the high rate of thermal losses associated with such an expansive solar array, and the effect of increasing ambient temperature on cell efficiency for the PV array. For the system with an average solar insolation of 1000 W/m², the efficiencies are shown in Figure 6.44 for the integrated system.

The results for the specific and total electricity consumption indicate that the most energy intensive process is the simultaneous H₂-CO₂ production by the E-CEM reactor. According to [66], optimization of the reactor may reduce its specific work to approach that of conventional water electrolysis (4.3 kWh/m³-H₂ STP). The impact on the total energy consumption by the E-CEM, SWRO, and methanol plant subsystems is shown in

Figure 6.45. Reducing the specific work requirement of the novel E-CEM reactor process is critical to the performance of the system; not only reducing the power consumption, but also the fresh water demand (and therefore power consumption) by the SWRO unit.

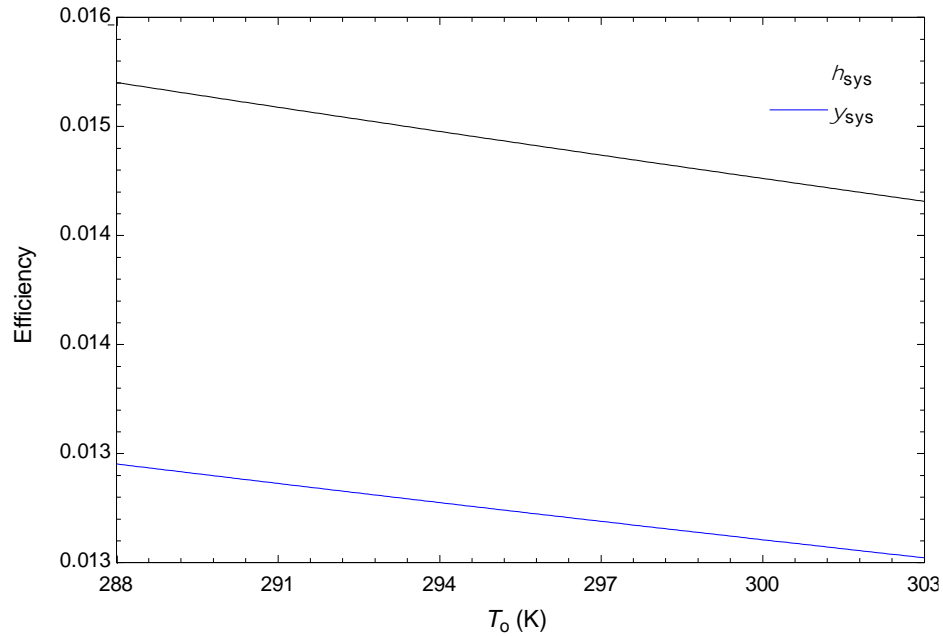


Figure 6.44: Effect of environmental temperature on System II energy and exergy efficiencies.

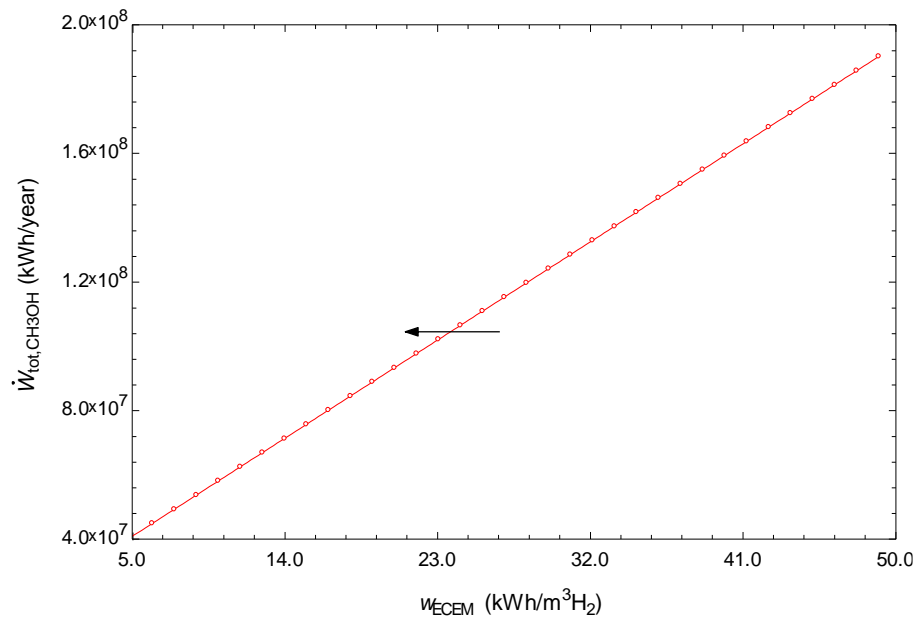


Figure 6.45: Effect of E-CEM specific-work reduction on total electricity consumption by SWRO, E-CEM, and methanol plant subsystems.

Figure 6.46 observes the effect on the energy and exergy efficiencies for the electrical-to-methanol conversion, which range from 0.049–0.233 and 0.047–0.225, respectively, and the integrated solar-methanol plant, which range from 0.015–0.070, and 0.013–0.060, respectively.

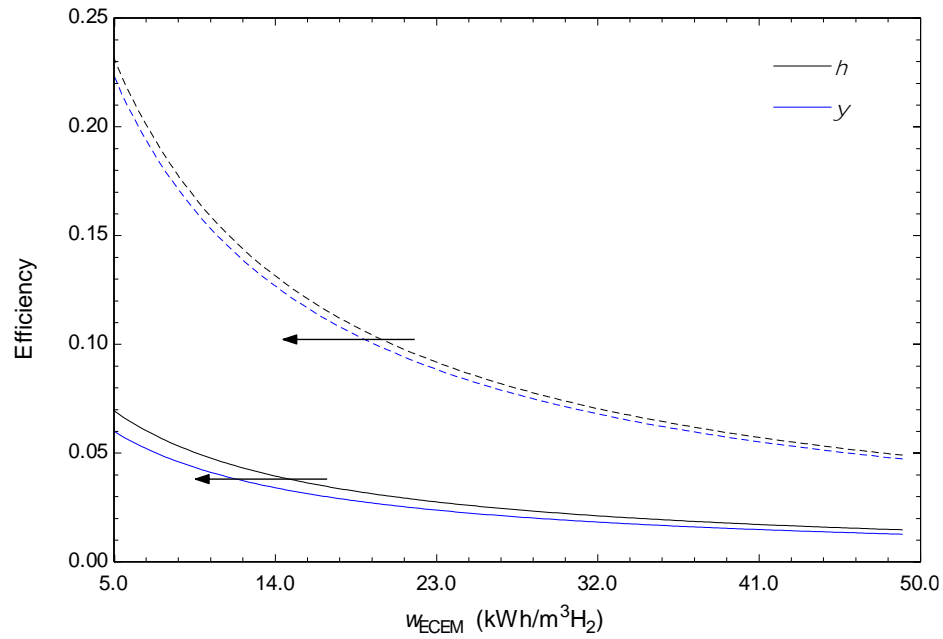


Figure 6.46: Effect of E-CEM specific-work reduction on electricity-to-methanol (dashed lines), and solar-to-methanol (solid lines) energy and exergy efficiencies.

CHAPTER 7: CONCLUSIONS AND RECOMMENDATIONS

7.1 Conclusions

Photoelectrochemical water splitting is an active area of research in green methods for solar hydrogen production. Much of the theoretical experimental research focuses on characterization and comparison of photoactive materials and individual PEC components under ideal laboratory conditions at very small scale. This thesis study develops and tests a fully integrated system that includes solar concentration with spectrum-splitting to supply energy to both PEC H₂ production and PV electricity generation from a single solar input. A theoretical case study of the CPV-PEC system is integrated in a methanol synthesis plant for solar fuel generation as an H₂ storage medium and as a practical liquid fuel for direct use in transportation and power generation applications.

- A novel PEC reactor design with a large area (930 cm²) proton exchange membrane and photocathode (820 cm²) has been built and tested under simulated and ambient solar light. The PEC-electrolysis reactor has energy and exergy efficiency values of 71.5% and 69.7%, respectively.
- The integrated CPV-PEC apparatus has overall energy and exergy efficiency values of 1.7% and 1.3%, respectively, with the most significant losses occurring during light concentration, transmission, and reflection.
- The theoretical integrated methanol process for System I has overall energy and exergy efficiency values of 7.0% and 7.0%, respectively.

7.2 Recommendations

Based on the results presented in this thesis, the following recommendations are made for future experimental and theoretical studies:

- An experimental study of the integrated CPV-PEC for full day operation and solar tracking to investigate the performance of the system components and hydrogen production rate.
- An experimental study integrating CPV cooling with PEC reactor feed water to investigate potential efficiency improvements for both components.
- Investigation of PEC methanol synthesis options for tandem water electrolysis and fuel synthesis reactors.
- Assessment of sustainable water and CO₂ sources (for example municipal or industrial wastewater, and biomass carbon resources) in urban and rural regions.

REFERENCES

- [1] IEA. (2016). CO2 Emissions from Fuel Combustion Highlights 2016. pdf. (Online) Retrieved: May 2017. Retrieved from: <http://www.iea.org/publications/freepublications/publication/co2-emissions-from-fuel-combustion-highlights-2016.html>.
- [2] "EIA. (2017). International Energy Outlook 2016. Chapter 1. World energy demand and economic outlook. Outlook for world energy consumption by source. Excel data. Available: <https://www.eia.gov/outlooks/ieo/world.php>. Accessed: May 20, 2017".
- [3] Kaltschmitt, M., Streicher, W., & Wiese, A. (2007). Renewable energy: technology, economics and environment. Springer.
- [4] Joshi, A. S., Dincer, I., & Reddy, B. V. (2011). Solar hydrogen production: a comparative performance assessment. *International Journal of Hydrogen Energy*, 36(17), 11246-11257.
- [5] Grimes, C. A., Varghese, O. K., & Ranjan, S. (Eds.). (2007). Light, water, hydrogen: the solar generation of hydrogen by water photoelectrolysis. Springer.
- [6] Das, D., and Veziroğlu, T. N. (2001). Hydrogen production by biological processes: a survey of literature. *International Journal of Hydrogen Energy*, 26(1), 13-28.
- [7] Dincer, I. (2012). Green methods for hydrogen production. *International journal of hydrogen energy*, 37(2), 1954-1971.
- [8] Motyka, T., W. Summers, and R. Zidan. (2004) "Hydrogen storage: the key challenge facing a hydrogen economy." United States Department of Energy.
- [9] US Department of Energy (US DOE). Office of Energy Efficiency and Renewable Energy. (2015). Hydrogen Storage. Retrieved from: <http://energy.gov/eere/fuelcells/hydrogen-storage>>..
- [10] Burke, A., & Gardiner, M. (2005). Hydrogen storage options: Technologies and comparisons for light-duty vehicle applications. Institute of Transportation Studies.
- [11] Olah, G. A. (2005). Beyond oil and gas: the methanol economy. *Angewandte Chemie International Edition*, 44(18), 2636-2639.
- [12] "US Department of Energy. (2017). Renewable Hydrocarbon Biofuels < https://www.afdc.energy.gov/fuels/emerging_hydrocarbon.html > Accessed: June 01, 2017."

- [13] "Hogerwaard, J., Dincer, I., & Zamfirescu, C. (2017). Thermodynamic and Environmental Impact Assessment of NH₃ Diesel-Fueled Locomotive Configurations for Clean Rail Transportation. *Journal of Energy Engineering*, 143(5), 04017018."
- [14] C. Zamfirescu and I. Dincer, "Ammonia as a green fuel and hydrogen source for vehicular applications.," *Fuel processing technology*, pp. 729-737, 2009.
- [15] A. J. Reiter and S.-C. Kong, "Combustion and emissions characteristics of compression-ignition engine using dual ammonia-diesel fuel.," *Fuel*, pp. 87-97, 2011.
- [16] Elucidare, "Ammonia - New possibilities for hydrogen storage and transportation," Elucidare Ltd., 2008.
- [17] Methanol Institute. (2015). [Supply and demand data figure]. MMSA Supply and Demand Balance (2008-2013E): World. Retrieved from <<http://www.methanol.org/-Methanol-Basics.aspx>>.
- [18] Ipinazar, E. (2013). Methanol: a future transport fuel based on hydrogen and carbon dioxide?. *Methanol Production and Use from a Lifecycle Perspective*. STOA – EU Parliament – Brussels, October 17, 2013. (Online). Retrieved: August 8, 2015 from: <<http://ww>>.
- [19] Grobe, H. (2006). Air - sea exchange of carbon dioxide. (Figure). Alfred Wegener Institute for Polar and Marine Research, Bremerhaven, Germany. [CC BY-SA 2.5 (<http://creativecommons.org/licenses/by-sa/2.5>)], via Wikimedia Commons. URL: <https://upload.wiki>.
- [20] "Bauer, J. E., Cai, W. J., Raymond, P. A., Bianchi, T. S., Hopkinson, C. S., & Regnier, P. A. (2013). The changing carbon cycle of the coastal ocean. *Nature*, 504(7478), 61-70".
- [21] Riebeek, H. (2011, June 16). The Carbon Cycle. NASA Earth Observatory (NEO). (Online). Retrieved: August 10, 2015, from <http://earthobservatory.nasa.gov/-Features/CarbonCycle/>.
- [22] NOAA. (nd). National Oceanic and Atmospheric Administration – Ocean. (Online). Retrieved: March 2015. URL: <<http://www.noaa.gov/ocean.html>>.
- [23] Greenlee, L. F., Lawler, D. F., Freeman, B. D., Marrot, B., & Moulin, P. (2009). Reverse osmosis desalination: water sources, technology, and today's challenges. *Water research*, 43(9), 2317-2348.
- [24] Wang, J., Wang, X., Jiang, A., Jiangzhou, S., & Li, P. (2014). Operational Optimization of Large-Scale Parallel-Unit SWRO Desalination Plant Using

- Differential Evolution Algorithm. The Scientific World Journal, 2014, 584068. doi:10.1155/2014/584068.
- [25] Rycroft, M. (2014). Water Desalination and Energy. Energize. EE Publishers. (Online) Retrieved: February 2015, from <<http://www.ee.co.za/article/water-desalination-energy.html>>.
- [26] "Coelho, B., Oliveira, A. C., & Mendes, A. (2010). Concentrated solar power for renewable electricity and hydrogen production from water—a review. Energy & Environmental Science, 3(10), 1398-1405".
- [27] Kalogirou, S. A. (2004). Solar thermal collectors and applications. Progress in energy and combustion science, 30(3), 231-295.
- [28] "Romero, M., & Steinfeld, A. (2012). Concentrating solar thermal power and thermochemical fuels. Energy & Environmental Science, 5(11), 9234-9245".
- [29] Dincer, Ibrahim, and Calin Zamfirescu. (2014). "Chapter 7 - Renewable-Energy-Based Power Generating Systems". Advanced Power Generation Systems. Elsevier Science and Technology Books, Inc.
- [30] Wang, Z., Roberts, R. R., Naterer, G. F., & Gabriel, K. S. (2012). Comparison of thermochemical, electrolytic, photoelectrolytic and photochemical solar-to-hydrogen production technologies. International Journal of Hydrogen Energy, 37(21), 16287-16301.
- [31] Hepbasli, A., & Alsuhaibani, Z. (2011). A key review on present status and future directions of solar energy studies and applications in Saudi Arabia. Renewable and Sustainable Energy Reviews, 15(9), 5021-5050.
- [32] Ursua, A., Gandia, L. M., & Sanchis, P. (2012). Hydrogen production from water electrolysis: current status and future trends. Proceedings of the IEEE, 100(2), 410-426.
- [33] Roy, A. (2006). Dynamic and transient modelling of electrolyzers powered by renewable energy sources and cost analysis of electrolytic hydrogen (Doctoral dissertation, Loughborough University).
- [34] Ivy, J. (2004). Summary of electrolytic hydrogen production: milestone completion report (No. NREL/MP-560-36734). National Renewable Energy Lab., Golden, CO (US).
- [35] Ni, M., Leung, M. K. H., & Leung, Y. C. (2006). Electrochemistry Modeling of Proton Exchange Membrane (PEM) Water Electrolysis for Hydrogen Production. In 16th World Hydrogen Energy Conference, 13-16 June 2006, Lyon, France.

- [36] Zoulias, E., Varkaraki, E., Lymberopoulos, N., Christodoulou, C. N., & Karagiorgis, G. N. (2004). A review on water electrolysis. *TCJST*, 4(2), 41-71.
- [37] "Jia, J., Seitz, L. C., Benck, J. D., Huo, Y., Chen, Y., Ng, J. W. D., ... & Jaramillo, T. F. (2016). Solar water splitting by photovoltaic-electrolysis with a solar-to-hydrogen efficiency over 30%. *Nature communications*, 7, 13237".
- [38] Jorquera, O., Kiperstok, A., Sales, E. A., Embirucu, M., & Ghirardi, M. L. (2010). Comparative energy life-cycle analyses of microalgal biomass production in open ponds and photobioreactors. *Bioresource technology*, 101(4), 1406-1413.
- [39] Bolton, J. R. (1996). Solar photoproduction of hydrogen: a review. *Solar energy*, 57(1), 37-50.
- [40] Cifre, P. G., & Badr, O. (2007). Renewable hydrogen utilisation for the production of methanol. *Energy conversion and management*, 48(2), 519-527.
- [41] Choi, M. J., & Cho, D. H. (2008). Research activities on the utilization of carbon dioxide in Korea. *CLEAN–Soil, Air, Water*, 36(5-6), 426-432.
- [42] Chen, Z., Dinh, H., & Miller, E. (2013). *Photoelectrochemical Water Splitting: Standards, Experimental Methods, and Protocols*. Springer Science & Business Media.
- [43] Fujishima, A., & Honda, K. (1972). Electrochemical photolysis of water at a semiconductor electrode. *nature*, 238(5358), 37-38..
- [44] Hamann, T. W., & Lewis, N. S. (2006). Control of the stability, electron-transfer kinetics, and pH-dependent energetics of Si/H₂O interfaces through methyl termination of Si (111) surfaces. *The Journal of Physical Chemistry B*, 110(45), 22291-22294.
- [45] Li, J., & Wu, N. (2015). Semiconductor-based photocatalysts and photoelectrochemical cells for solar fuel generation: a review. *Catalysis Science & Technology*, 5(3), 1360-1384.
- [46] Gratzel, M. (2001). Photoelectrochemical cells. *nature*, 414(6861), 338-344.
- [47] Walter, M. G., Warren, E. L., McKone, J. R., Boettcher, S. W., Mi, Q., Santori, E. A., & Lewis, N. S. (2010). Solar water splitting cells. *Chemical reviews*, 110(11), 6446-6473.
- [48] Acar, C., & Dincer, I. (2014). Analysis and assessment of a continuous-type hybrid photoelectrochemical system for hydrogen production. *International Journal of Hydrogen Energy*, 39(28), 15362-15372.

- [49] "Modestino, M. A., & Haussener, S. (2015). An integrated device view on photo-electrochemical solar-hydrogen generation. Annual review of chemical and biomolecular engineering, 6, 13-34".
- [50] Fuel Cells Etc, "Fuel Cells Etc: Commercial Fuel Cell Components," 2017. [Online]. Available: <http://fuelcellsetc.com/>. [Accessed April 2016].
- [51] DuPont Fuel Cells. (2008). Nafion ® Membranes. pdf. Retrieved from: <http://www.fuelcellsetc.com/store/data-sheets>. Accessed: March 8, 2017.
- [52] Edmund Optics (2016). Cold Mirror: Specifications and Documents. Online. Available: < <https://www.edmundoptics.com/optics/optical-mirrors/hot-cold-mirrors/cold-mirrors/1900/>>. Accessed: Oct. 21, 2016..
- [53] Sunwize. (2016). Sunwize Specialty Products. Specialty Module. [Online]. <<http://dealer.sunwize.com/index.cfm?page=products&productid=4220>>. Last Accessed: May 8, 2017.
- [54] Gamry Instruments. (2017). Gamry Reference 3000 Potentiostat/Galvanostat/ZRA: Specifications. [Online]. <<https://www.gamry.com/potentiostats/reference-3000/>>. Accessed: June 10, 2017.
- [55] OAI (2013). Trisol Class AAA Standard Solar Simulator (TSS) Data Sheet. pdf. Available: <<http://www.oainet.com/oai-solarsimulator-pp.html>>. Accessed: Apr. 13, 2015.
- [56] Ocean Optics. (2017). USB-650 Red Tide Spectrometers. (Online). Available: <https://oceanoptics.com/product/usb-650-red-tide-spectrometers/>. Accessed: May 31, 2017.
- [57] Vernier Software Technology. (2017). Surface Temperature Sensor. Available from: <<https://www.vernier.com/products/sensors/temperature-sensors/sts-bta/>>. Accessed: May 31, 2017.
- [58] Vernier Software Technology. (2017). Products – Pyranometer. Available from: <<https://www.vernier.com/products/sensors/solar-radiation-sensors/pyr-bta/>>. Accessed: May 31, 2017.
- [59] Brito, J. F. D., Silva, A. A. D., Cavaleiro, A. J., & Zanoni, M. V. B. (2014). Evaluation of the parameters affecting the photoelectrocatalytic reduction of CO₂ to CH₃OH at Cu/Cu₂O electrode. International Journal Of Electrochemical Science, 5961-5973.

- [60] Luo, J., Steier, L., Son, M. K., Schreier, M., Mayer, M. T., & Grätzel, M. (2016). Cu₂O nanowire photocathodes for efficient and durable solar water splitting. *Nano letters*, 16(3), 1848-1857.
- [61] Navidi, W. C. (2006). *Statistics for engineers and scientists* (Vol. 2). New York: McGraw-Hill.
- [62] Kim, J. H., Simon, T. W., & Viskanta, R. (1993). Journal of heat transfer policy on reporting uncertainties in experimental measurements and results. *Journal of Heat Transfer*, 115(1), 5-6.
- [63] Rihko-Struckmann, L. K., Peschel, A., Hanke-Rauschenbach, R., & Sundmacher, K. (2010). Assessment of methanol synthesis utilizing exhaust CO₂ for chemical storage of electrical energy. *Industrial & Engineering Chemistry Research*, 49(21), 11073-11078.
- [64] El-Emam, R. S., & Dincer, I. (2014). Thermodynamic and thermoeconomic analyses of seawater reverse osmosis desalination plant with energy recovery. *Energy*, 64, 154-163.
- [65] Eisaman, M. D., Parajuly, K., Tuganov, A., Eldershaw, C., Chang, N., & Littau, K. A. (2012). CO₂ extraction from seawater using bipolar membrane electrodialysis. *Energy & Environmental Science*, 5(6), 7346-7352.
- [66] Willauer, H. D., DiMascio, F., Hardy, D. R., & Williams, F. W. (2014). Feasibility of CO₂ Extraction from Seawater and Simultaneous Hydrogen Gas Generation Using a Novel and Robust Electrolytic Cation Exchange Module Based on Continuous Electrodeionization.
- [67] "National Institute of Standards and Technology (NIST). (2011). Chemistry WebBook. (Online).
<<http://webbook.nist.gov/cgi/cbook.cgi?ID=C1333740&Mask=1#Thermo-Gas>>.
Last accessed: May 20, 2016".
- [68] Zamfirescu, C., & Dincer, I. (2009). How much exergy one can obtain from incident solar radiation?. *Journal of Applied Physics*, 105(4), 044911.
- [69] Duffie, J. A., & Beckman, W. A. (2013). *Solar engineering of thermal processes*. John Wiley & Sons..
- [70] Bicer, Y., Dincer, I., & Zamfirescu, C. (2016). Effects of various solar spectra on photovoltaic cell efficiency and photonic hydrogen production. *International Journal of Hydrogen Energy*, 41(19), 7935-7949.

- [71] Teranishi, K., Tsushima, S., & Hirai, S. (2005). Study of the effect of membrane thickness on the performance of polymer electrolyte fuel cells by water distribution in a membrane. *Electrochemical and Solid-State Letters*, 8(6), A281-A284.
- [72] Gurau, V., Barbir, F., & Liu, H. (2000). An analytical solution of a half-cell Model for PEM fuel cells. *Journal of the Electrochemical Society*, 147(7), 2468-2477.
- [73] "Carmo, M., Fritz, D. L., Mergel, J., & Stolten, D. (2013). A comprehensive review on PEM water electrolysis. *International journal of hydrogen energy*, 38(12), 4901-4934".
- [74] Eikerling, M., Kharkats, Y. I., Kornyshev, A. A., & Volkovich, Y. M. (1998). Phenomenological Theory of Electro-osmotic Effect and Water Management in Polymer Electrolyte Proton-Conducting Membranes. *Journal of the Electrochemical Soc.*, 145(8), 2684-2699.
- [75] "Bak T, Nowotny J, Rekas M, Sorrell CC. Photo-electrochemical hydrogen generation from water using solar energy. Materials-related aspects. *International Journal of Hydrogen Energy*. 2002;27(10):991-1022".
- [76] "Chiang C-Y, Shin Y, Aroh K, Ehrman S. Copper oxide photocathodes prepared by a solution based process. *International Journal of Hydrogen Energy*. 2012;37(10):8232-9".
- [77] "Dotan, H., Mathews, N., Hisatomi, T., Grätzel, M., & Rothschild, A. (2014). On the Solar to Hydrogen Conversion Efficiency of Photoelectrodes for Water Splitting. *The journal of physical chemistry letters*, 5(19), 3330."
- [78] "Dorf, R. C., & Bishop, R. H. (2011). *Modern control systems*. Pearson."
- [79] Mittelman, G., Kribus, A., & Dayan, A. (2007). Solar cooling with concentrating photovoltaic/thermal (CPVT) systems. *Energy Conversion and Management*, 48(9), 2481-2490.
- [80] Lim, H. W., Park, M. J., Kang, S. H., Chae, H. J., Bae, J. W., & Jun, K. W. (2009). Modeling of the kinetics for methanol synthesis using Cu/ZnO/Al₂O₃/ZrO₂ catalyst: influence of carbon dioxide during hydrogenation..
- [81] Bucher, W. (2002). "Renewable Energy Systems and Desalination – Volume III: Reverse Osmosis by Solar Energy". *Encyclopedia of Desalination and Water Resources (DEWARE)*. (Online). Retrieved: March 2015 from <<http://www.desware.net/>>.
- [82] Iizuka, A., Hashimoto, K., Nagasawa, H., Kumagai, K., Yanagisawa, Y., & Yamasaki, A. (2012). Carbon dioxide recovery from carbonate solutions using

- bipolar membrane electrodialysis. *Separation and purification technology*, 101, 49-59.
- [83] Lazzaretto, A., & Tsatsaronis, G. (2006). SPECO: a systematic and general methodology for calculating efficiencies and costs in thermal systems. *Energy*, 31(8), 1257-1289.
- [84] Almahdi, M. (2016). Integrated heat pump options for heat upgrading in Cu-Cl cycle for hydrogen production (MAsc Thesis, University of Ontario Institute of Technology).
- [85] Turton, R., Baillie, R. C., Whiting, W. B., & Shaeiwitz, J. A. (2009). *Analysis, Synthesis, and Design of Chemical Processes*. US: Pearson Education.
- [86] Meyer, L., Castillo, R., Buchgeister, J., & Tsatsaronis, G. (2009). Application of exergoeconomic and exergoenvironmental analysis to an SOFC system with an allothermal biomass gasifier. *International Journal of Thermodynamics*, 12(4), 177.
- [87] Bicer, Y., Dincer, I., & Aydin, M. (2016). Maximizing performance of fuel cell using artificial neural network approach for smart grid applications. *Energy*, 116, 1205-1217..
- [88] Deb, K. (2001). *Multi-objective optimization using evolutionary algorithms* (Vol. 16). John Wiley & Sons.
- [89] Konak, A., Coit, D. W., & Smith, A. E. (2006). Multi-objective optimization using genetic algorithms: A tutorial. *Reliability Engineering & System Safety*, 91(9), 992-1007.
- [90] NREL. (2010). ASTM G173-03 Reference Spectra. Derived from: SMARTS v. 2.9.2. Excel Software. Download Available: http://www.nrel.gov/rredc/smarts/smarts_files.html. Accessed: April 17, 2016.
- [91] Patterson, BD., Holzner, R., Kurum, A., Rossel, C., Willauer, HD., and van Bokhoven, JA. (2015). "Proposed liquid fuel production on artificial islands", Conference on Energy, Science and Technology 2015, Karlsruhe, Germany, Book of Abstracts, p. 76.
- [92] Hogerwaard, J., Dincer, I., Naterer, G.F., Patterson, B.D. (2016). [In Review]. Solar methanol synthesis from seawater on offshore artificial islands. *Solar Energy Journal*.
- [93] Esmaili, P., Dincer, I., & Naterer, G. F. (2015). Development and analysis of an integrated photovoltaic system for hydrogen and methanol production. *International Journal of Hydrogen Energy*.

- [94] Yuan, L., & Xu, Y. J. (2015). Photocatalytic conversion of CO₂ into value-added and renewable fuels. *Applied Surface Science*, 342, 154-167.
- [95] "Szargut, J. (2005). Exergy method: technical and ecological applications (Vol. 18). WIT press."
- [96] "Ozbilen, A., Dincer, I., & Rosen, M. A. (2011). A comparative life cycle analysis of hydrogen production via thermochemical water splitting using a Cu–Cl cycle. *International Journal of Hydrogen Energy*, 36(17), 11321-11327".
- [97] "Molino, A., & Braccio, G. (2015). Synthetic natural gas SNG production from biomass gasification–Thermodynamics and processing aspects. *Fuel*, 139, 425-429."
- [98] Ham, A., Berg, H., Benneker, A., Simmelink, G., Timmer, J., & Weerden, S. (2012). Hydrogenation of carbon dioxide for methanol production. *Chemical engineering transactions*, 29, 181-186.
- [99] Zhao, W., Fu, W., Yang, H., Tian, C., Li, M., Li, Y., ... & Zou, G. (2011). Electrodeposition of Cu₂O films and their photoelectrochemical properties. *CrystEngComm*, 13(8), 2871-2877.